Fakultät für Luftfahrt, Raumfahrt

und Geodäsie

Material Screening of Fiber-Reinforced Polymers under Thermal Runaway Conditions

María Fernández de Palencia Navarro

Master Thesis, scientific work in fulfillment of the requirements for

the degree M.Sc. at TUM School of Engineering and Design.

Supervisor	Univ.-Prof. Dr.-Ing. Klaus Drechsler Lehrstuhl für Carbon Composites
Advisor	Margarita Etchegaray Bello, M.Sc. Lehrstuhl für Carbon Composites
Author	María Fernández de Palencia Navarro Calle Císcar 59 46005 Valencia Tel.: +34629603931 Matr.-Nr.: 03753744
Submission Date	München, 20.09.2024

Technische Universität München
Fakultät für Luftfahrt, Raumfahrt und Geodäsie
Lehrstuhl für Carbon Composites
Boltzmannstraße 15
D-85748 Garching bei München

Tel.: +49 (0) 89 / 289 − 15092
Fax: +49 (0) 89 / 289 − 15097
Email: info@lcc.mw.tum.de
Web: www.lcc.mw.tum.de

Technische Universität München │Lehrstuhl für Carbon Composites
Boltzmannstr. 15 │85748 Garching bei München

María Fernández de Palencia Navarro
Calle Císcar 59
9, p13 46005
Valencia, Spain

Garching bei München, April 1st, 2024

Task Assignment Master's Thesis
„Fiber-Reinforced Polymer Material Screening under Thermal Runaway Conditions for Li-ion Battery Enclosure"

Energy-efficient aircraft are of great interest for the future viability of aviation. One key challenge for the transition to electrification of this transport mode is the further optimization of the weight of energy storage components. Structural integration of batteries into the wing structure and optimal design of an aircraft with upswept wings can enable both a rapid contribution to sustainable aviation and the implementation of a fully electrified RAM. Furthermore, with the support of the Chair of Carbon Composites (LCC), the batteries required for electric flight are to be integrated into the wing structure, making the best possible use of the available installation space.

The LCC will support the battery integration into the wing structure, providing the necessary mechanical parameters for the design and considering the thermal properties of the battery cells, such as energy release during an explosion. An experimental characterization of various composite materials under realistic thermal and mechanical conditions of thermal runaway conditions will be conducted for the material selection of the battery module housings. The materials will be evaluated based on the degree of damage.

Contents:

- Literature review
  - o Fire properties of selected fiber-reinforced polymers
  - o Mechanical properties of selected fiber-reinforced polymers
  - o Fiber-reinforced polymers in battery casing applications
- Test matrix definition
- Preparation of the samples and sensors for experimental testing
- Improvement of the thermal runaway trigger mechanism, incl. the integration of the necessary electronic components
- Integration and calibration of the thermal camera for the testing
- Experimental testing
- Result analysis
- Documentation in English

Date of emission: 01.04.2024   Due date: 30.09.2024
Supervision: Prof. Dr.-Ing Klaus Drechsler   Lehrstuhl für Carbon Composites, TUM
                Margarita Etchegaray Bello, MSc.   Lehrstuhl für Carbon Composites, TUM

Declaration of Honor

I hereby declare on my honor that I have prepared this thesis independently and without the use of other than the indicated resources; the thoughts taken directly or indirectly from outside sources (including electronic sources) are identified as such without exception. The work has not been submitted in the same or similar form to any other examination authority.

München, 20.09.2024

City, Date

Signature

Übersicht

Energieeffiziente Flugzeuge sind von großem Interesse für die Zukunft der Luftfahrt. Das Masterarbeitsprojekt konzentriert sich auf eine der wichtigsten Herausforderungen für den Übergang zur Elektrifizierung dieses Verkehrsträgers: die Optimierung des Gewichts des Batteriegehäuses. Das Projekt wird in Zusammenarbeit mit dem Lehrstuhl für Carbon Composites an der Technischen Universität München (TUM) durchgeführt. Es wird eine experimentelle Charakterisierung verschiedener Verbundwerkstoffe unter realistischen thermischen und mechanischen Bedingungen des thermischen Durchgehens durchgeführt, um eine Materialauswahl für Batteriemodulgehäuse Anwendungen zu identifizieren. Schließlich werden die Materialien anhand des Schädigungsgrades bewertet.

Abstract

Energy-efficient aircraft are of great interest for the future of aviation. The master thesis project focuses on one of the key challenges for the transition to electrification of this transport mode: the optimization of the weight of the battery housing. The project will be carried out in collaboration with the Chair of Carbon Composites at the Technical University of Munich (TUM). An experimental characterization of various composite materials under realistic thermal and mechanical conditions of thermal runaway will be conducted for material selection of battery module housing applications. Finally, the materials will be evaluated based on the degree of damage.

Contents

Nomenclature

Formelzeichen	Einheit	Beschreibung
Al	$[-]$	Aluminium
Cd	$[-]$	Cadmium
H	$[-]$	Hidrogen
Ni	$[-]$	Nickel

Abbreviations

Abbreviation	Description
ABS	Acrylnitril-Butadien-Styrol
AH	Acumulated Heat
AlPi	Aluminum Diethyl Phosphinate
ARC	Accelerating Rate Calorimetry
AS	Ammonium Sulfamate
BMI	Bismaleimide
BMS	Battery Management System
CaAl-LDH	Calcium Aluminum Layered Double Hydroxide
CF	Carbon Fibers
CF/PPS	Carbon Fiber Reinforced Polyphenylene Sulfide
CFRP	Carbon fiber reinforced plastic
CLT	Corner Left Top
CMCs	Ceramic matrix composites
CMLT	Corner Middle Left Top
CRB	Corner Right Bottom
CRT	Corner Right Top
CTG	Concentration of Toxic Gases
CVC	Cell Volume Change
CVs	Cyclic voltammograms
DCS	Differential Scanning Calorimetry
DOPO	9,10-Dihydro-9-Oxa-10-Phosphaphenanthrene-10-Oxide
DSC	Differential Scanning calorimetry
EDS	Energy dispersive spectrometer
EG	Expandable Graphite
EHC	Effective Heat of Combustion
ESI	Extinction flammability index
ESS	Energy Storage System
EV	Electric Vehicle
EV-ARC	Extended Volume-Accelerating Rate Calorimetry
FIGRA	Fire Growth Rate
FR	Fire Retardant
FRCM	Fiber-reinforced composite materials
FRPs	Fiber Reinforced Polymers
FSI	Flame Spread Index
FSR	Flame Spread Rate
FT	Flame Temperature
GF	Glass Fibers

Abbreviation	Description
GF/PC	Glass Fiber Reinforced Polycarbonate
GF/PET	Glass Fiber Reinforced Polyethylene Terephthalate
GF/PETG	Glass Fiber Reinforced Polyethylene Terephthalate Glycol
GF/PP	Glass Fiber Reinforced Polypropylene
GF/PPS	Glass Fiber Reinforced Polyphenylene Sulfide
HR	Heating Rate
HRe	Heat Release
HRR	Average Heat Release Rate
HRR	Heat Release Rate
HRr	Heating Rate Ratio
ICP	Inductively coupled plasma
IR	Internal Resistance
ISC	Internal Short Circuit
IT	Internal Temperature
LCO	Lithium Cobalt Oxygen
LFP	Lithium Ferrum Phosphate
LIB	Lithium-ion battery
LMO	Lithium Manganese Oxide
LMP	Lithium-Metal-Polymer
LND	Lithium Nickel Dioxide
LOI	Limiting Oxygen Index
M	Middle
ML	Mass Loss
MLR	Mass Loss Rate
MMCs	Metal matrix composites
MPP	Melamine Polyphosphate
NCA	Nickel Cobalt Aluminium Oxides
NMC	Nickel Manganese Cobalt
p	Pressure
PC	Polycarbonate
PEEK	Polyether ether ketone
PHR	Peak Heat Release Rate
PHRT	Peak Heat Release Temperature
PMCs	Polymer matrix composites
PPS	Polyphenylene sulfide
PSPR	Peak Smoke Production Rate
RAM	Regional Air Mobility
RW	Residual Weight
SD	Smoke density
SEI	Solid Electrolyte Interface

Abbreviation	Description
SEM	Scanning electron microscope
SMT	Smoke Temperature
SOC	State of charge
SPR	Smoke Production Rate
S/T	Smoke/ Toxicity
ST	Surface Temperature
SYT	Safety Time
T	Temperature
TD	Temperature Difference
TE	Time to Explosion
THE	Total Heat Evolved
THR	Total Heat Release
TI	Time To Ignition
TPHR	Time to Peak Heat Release
TR	Thermal Runaway
TRP	Thermal Runaway Propagartion
TS	Time Smoke
TSP	Total Smoke Production
TSR	Total Smoke Release
TV	Time Venting
V	Voltage
VD	Voltage Drop
VT	Venting Temperature
XRD	X-ray diffraction
ZnPi	Zinc Diethyl Phosphinate

1 Introduction

Energy-efficient aircraft are of great interest for the future viability of aviation. The transition to electrification of the aeronautical sector presents key challenges for the energy storage system (ESS), it should operate with the widest array of storage and operating limits and have the highest performance characteristics of their type while keeping low mass and volume combinations, being secure and trustworthy; and cost-effective [87].

Lithium-ion batteries (LIBs) are the most rapidly growing high-energy storage device in the industry [21]. They are used as an auxiliary or the main power supply for electric propulsion vehicles (EVs) in the case of endoatmospheric aircraft over other electrochemical cells [87]. LIBs require protection to ensure a safe operation and avoid failures: performance degradation, thermal runaway (TR), temperature maldistribution, and low-temperature performance [61]. TR occurs when elevated temperatures induce an exothermic reaction that goes out of control, increasing its rate and temperature. This increase in temperature leads to a further increase in the reaction rate, which can turn into an explosion [61, 88, 80].

To address these challenges, fiber-reinforced composite materials (FRCMs) have been identified as a promising solution for battery housing in energy storage systems. FRCMs present advantages compared to other traditional materials, such as strength, low weight, resistance to corrosion, design flexibility, and long-term durability [31]. These characteristics make composite materials suitable for a wide variety of applications in aerospace. However, a few challenges still exist regarding their use in the aeronautical sector, such as the limited information on the behavior of composite structures due to less experience with composite airframes and parts compared to metallic designs [77].

Several studies focus on LIBs' TR and composite materials' fire resistance and fire reaction properties. Nevertheless, the literature focusing on the behavior of FRCMs under the TR process of LIBs is limited.

The use of FRCMs for the ESS will suppose an improvement in its weight optimization, being a key factor in the transition to electrification in the aeronautic sector. A material screening for the battery module housing is performed in this project, characterizing the behavior of various composite materials under realistic thermal and mechanical conditions of thermal runaway. TR is induced by thermal abuse in the two cell configurations studied, seven 21700 cells and one 4695 cell. The UL 2596 test method is used as a guideline to validate the thermal and mechanical performance of five different materials: CF/PC, CF/PEEK, CF/PPS, GF/PEEK, and GF/PPS.

A final evaluation of the materials tested is performed, considering the temperature ratio between the maximum temperature inside the cell enclosure and the maximum sample temperature, the mass loss of the composite material after the TR process, and the temperature difference along the sample during the TR process.

2 State of the art

This section discusses the current state of the art regarding lithium-ion batteries, thermal runaway, composite materials, and experimental methods employed to characterize the properties of composite materials under realistic thermal and mechanical conditions of thermal runaway.

2.1 Lithium Ion Battery (LIB)

2.1.1 Working principle

Lithium-ion batteries (LIBs) function on a principle centered around three main components: the anode, cathode, and electrolyte [88]. The electrodes inside LIB determine the capacity and energy density of the battery [61].

Conventional LIBs are made from carbon, the cathode is a metal oxide, and the electrolyte is a lithium salt in an organic solvent. Graphite is commonly employed as the anode material, while a layered oxide, a poly-anion, or a spinel serve as cathodes, and a mixture of organic carbonates containing complexes of lithium ions serves as the electrolyte. [88]

A separator splits the anode and the cathode; it separates the positive and negative electrodes while allowing ions to pass through, and it is composed of a thin sheet of micro-perforated plastic [88]. It is used to separate the positive and the negative electrodes in case of an internal short circuit. Li-ions can pass through without restriction, but electrons are blocked and not allowed to cross under normal circumstances, as in an electrical insulator, when the temperature inside the cell is outsized, the separator shuts the cell down, working as a fuse to prevent thermal runaway from happening [61].

Other parts of the LIB are the current collector and the case. The collector collects the currents generated by the batteries, and its negative side is usually made of copper, and the positive side is generally of aluminum. The cell case is a sealed container that braces the cell; it is usually made of steel or aluminum to achieve satisfactory mechanical and thermo-physical properties [61]. In the Figure 2.1, a schematic representation of the LIB components can be observed.

A schematic representation of the working principle LIB cell is found in Figure 2.2. During the charge cycle of a LIB, lithium ions move from the cathode (positive electrode) to the anode (negative electrode) through the electrolyte and the separator. Simultaneously, the electrons are released at the surface of the electrode particles to maintain the electric equilibrium. To form the charge current, the electrons are collected by the cathode and

travel via the external electrical circuit to the anode. Finally, the lithium ions react with the electrons and are intercalated into the cathode materials. During the discharge cycle, the inverse process occurs; an equal amount of lithium ions and electrons move from the cathode to the anode through the internal and external passage [61] [88]. LIBs are also known as swing batteries or rocking chair batteries due to the two-way movement of the Li-ions between the anode and the cathode during the charge and discharge process. The total energy of a battery, i.e., the storing and lasting capacity, is highly dependent on the lithium electrodes that can take in; the more they are, the greater energy it can store [88].
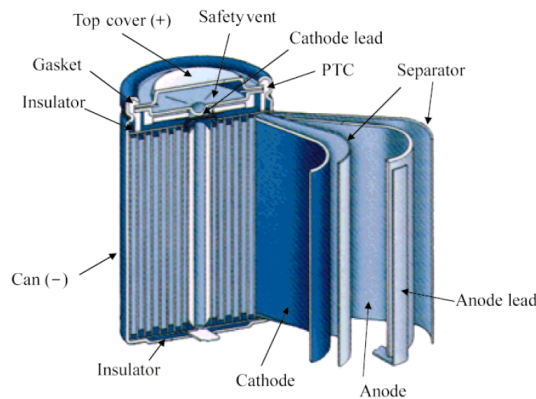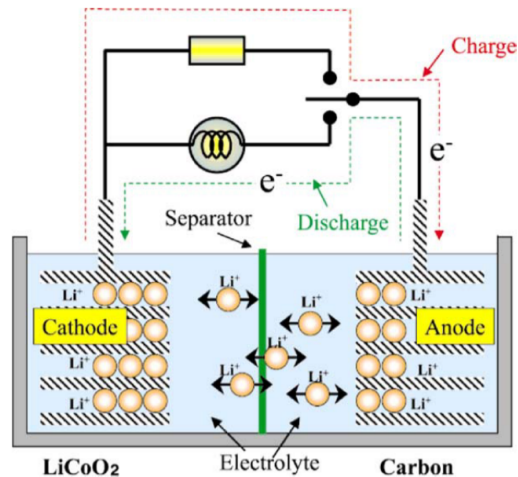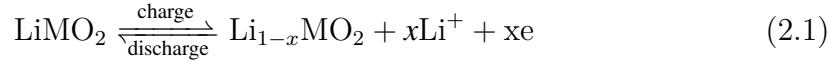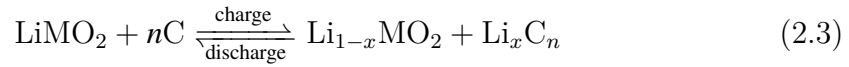

Figure 2.1   : LIB structure [69]

Figure 2.2   : Schematic representation of the working principle LIB cell [69]

Most types of LIBs are based on the $C/LiPF_6$ in $EC-DMC/LiMO_2$ sequence and operate following the cathode half-reaction (Equation 2.1) and the anode half-reaction (Equation 2.2) [88].

$$\text{LiMO}_2 \xrightleftharpoons[\text{discharge}]{\text{charge}} \text{Li}_{1-x}\text{MO}_2 + x\text{Li}^+ + \text{xe} \qquad (2.1)$$

$$n\text{C} + x\text{Li}^+ + \text{xe} \xrightleftharpoons[\text{discharge}]{\text{charge}} \text{Li}_x\text{C}_n \qquad (2.2)$$

The full cell reaction would correspond to Equation 2.3 where M is among others Co, Ni, Fe, W. Cathode materials may be $LiCoO_2, LiNiO_2, LiMn_2O_4, LiFeO_2, LiWO_2$ and anode materials $Li_xC_6, TiS_2, WO_3, NbS_2, V_2O_5$ among others [88].

$$\text{LiMO}_2 + n\text{C} \xrightleftharpoons[\text{discharge}]{\text{charge}} \text{Li}_{1-x}\text{MO}_2 + \text{Li}_x\text{C}_n \qquad (2.3)$$

2.1.2 Types and properties of lithium-ion batteries

Classification according to configuration

Most common LIBs designed for electric vehicles (EVs) usually have a cylindrical or prismatic configuration. Cells are winding and stacking up the anode-separator-cathode sandwich layer; a single cell would not be adequate to provide enough energy and power for vehicle usage. Prismatic design configuration optimizes the space and increases flexibility, while manufacturing cylindrical cells is easier, which makes them cheaper. [61]

To form the battery modules, multiple cells are connected either in series and/or in parallel. These modules are linked in series or parallel using electric wiring to constitute a battery pack and provide the required voltage and capacity for a specific application [61] [88]. Battery thermal models should be designed for the configuration [88]. In Figure 2.3, the schematics of a module configuration of cylindrical, prismatic, and elliptic cells can be observed.
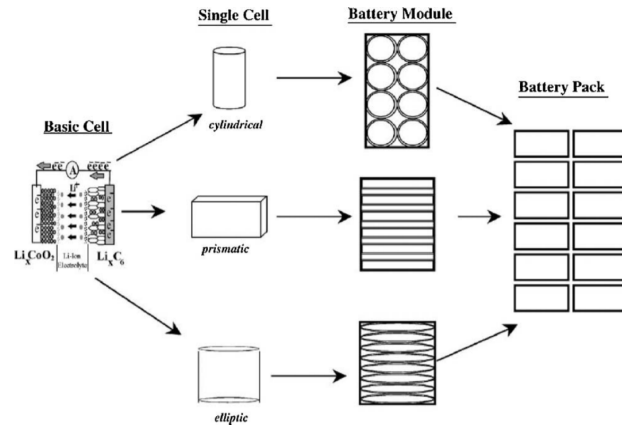

Figure 2.3 : Schematics of the battery pack design with different cell configurations [22]

Classification according to electrode materials

Electrode materials from LIB can be divided into three types according to their structure [61] [40]:

- Layered structure: lithium transition metal oxides with layered structure, such as Nickel Manganese Cobalt (NMC), Lithium Cobalt Oxygen (LCO), Lithium Nickel Cobalt Aluminium Oxides (NCA), and Lithium Nickel Dioxide (LND). Some examples are $LiCoO_2$ (LCO), $Li(NI_{0.8}Co_{0.15}Al_{0.05})$ (NCA) and $LiNiO_2$ (LNO).

- Spinel structure: Refers to Lithium Manganese Oxide (LMO), an example is $LiMn_2O_4$.

- Olivine structure: transition metal phosphates containing lithium, such as Lithium, Ferrum, Phosphate (LFP), and Lithium-Metal-Polymer (LMP). Some examples are $LiFePO_4$ (LFP) and $LiMnPO_4$ (LMP).

$LiCoO_2$ was the first LIB marketed and is one of the most common choices in the industry. Its advantages are its high capacity and mature preparation procedure, while its inconveniences include its toxicity, high material cost, and poor thermal stability. In contrast, $LiFePO_4$ is more resistant to thermal abuse [61]. In Table 2.1, some of the properties of the different kinds of chemistry are observed.

Positive electrode	$LiCoO_2$	$Li(Ni_{0.8}Co_{0.15}Al_{0.05})O_2$	$Li(Ni_{1-x-y}Mn_xCo_y)O_2$	$LiMn_2O_4$	$LiFePO_4$
Abbreviation	LCO	NCA	NMC	LMO	LFP
Cell voltage (V)	3.7-3.9	3.65	3.8-4.0	4.0	3.3
Specific energy	Good	Excellent	Excellent	Moderate	Moderate
Power	Moderate	Good	Moderate	Good	Good
Safety	Bad	Moderate	Moderate	Good	Excellent
Lifespan	Moderate	Good	Moderate	Moderate	Good
Cost	Bad	Moderate	Moderate	Good	Good
Specific capacity [mAh/g]	155	200	140-180	100-120	160
Midpoint V vs. Li at C/20	3.9	3.73	3.8	4.05	3.45

Table 2.1 : Characteristics of different positive electrode materials [61] [37]

Classification of cylindrical cells according to battery sizing

In the experimental part of the project, cylindrical cells are employed. Therefore, this section explains the types of cylindrical batteries that exist. Cylindrical cells present various sizing formats depending on the manufacturer and purpose. They are usually numbered with four digits. The first two digits correspond to the diameter of the cylinder in millimeters, and the two last digits correspond to the height in millimeters [28]. For example, the cells used in the current study are the 4695, which has 46 mm of diameter and 95 mm of height, and the 21700, which has 21 mm of diameter and 70 mm of

height. In figure Figure 2.4, the evolution in the sizing of the batteries over the years can be observed. With the size information of the cylindrical cells, the volumetric energy density can be calculated following Equation 2.4.

$$\text{Volumetric energy density } [Wh/cm^3] = \frac{\text{Energy } [Wh]}{\text{Volume } [cm^3]}$$
$$= \frac{\text{Capacity } [Ah] \cdot \text{Nominal Voltage } [V]}{\text{Volume } [cm^3]} \quad (2.4)$$
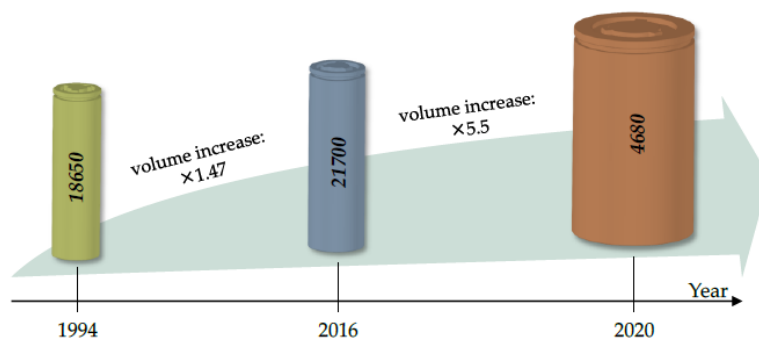
Figure 2.4 : Cell format evolution [28]

2.1.3 Types of failure

The optimum performance of LIBs is obtained when they are kept in a range of 15 to 35 ºC; when the working temperatures exceed these limits, batteries' performance, safety, and life duration deteriorate. This range of operating or storage temperatures can be exceeded in real-life applications. Li-ion batteries have two main temperature failure sources that affect their performance: operating temperature exceeding acceptable limits and localized degradation due to a low-temperature uniformity leading to a shortened battery lifespan [61]. The main thermal risks include:

- Performance degradation: Performance degradation in lithium-ion batteries refers to the deterioration in capacity and power output, particularly under high temperatures. Lithium loss and active material reduction inside the battery lead to capacity fade, while the increasing cell internal resistance due to the elevated temperature leads to power abatement. [61]

- Thermal runaway: A series of interconnected and undesired processes and reactions that feed into one another. The elevated temperatures induce an exothermic reaction that goes out of control, increasing its rate and temperature. This increase in temperature leads to a further increase in the reaction rate, which can turn into an explosion [61] [88] [80]. The cell is exposed to local temperatures higher than

7

100ºC -130 ºC when a failure occurs [26]. More information about this unexpected thermal behavior can be found in section 2.2.

- Temperature maldistribution: An uneven temperature distribution among cells and within individual cells during the charge and discharge process can adversely affect the whole cell's performance and may result in battery failure [61].

- Low-temperature performance: LIBs cell performance deteriorates when they work in low temperatures, especially below -20ºC when a reduction in the energy and power of the battery is observed [61].

2.1.4 Aerospace applications

LIB present advantages in comparison with other electrochemical cells: higher energy density per unit mass, they do not exhibit a memory effect, their self-discharge rate is less than half compared with other available solutions, their current lifetime is over 1000 cycles, and their self-life is more than 10 years [87]. These advantages had positioned LIB as the most rapidly growing high-energy storage device in the industry [21]. Nevertheless, LIB requires more protection to ensure a safe operation and avoid the type of failures analyzed in subsection 2.1.3.

Lithium-ion batteries are used in many applications in our daily lives; some examples are [21]:

- Portable electronic devices: smartphones, tablets, laptops, E-bikes, among others.

- Hybrid and Electric Vehicles: an example of LIB usage is found in Tesla EVs; before 2006, Early NCR 18650 was used in their vehicles, and during 2016, they used the 21700 LIB.

- Aerospace applications: ESS of satellites, auxiliary power supply of airplanes, main power supply of electric propulsion aircraft, among others.

- Medical applications: heart pacemakers and neurological pacemakers.

- Grid energy storage: to answer the stability issues of the clean energy resources.

Focusing on the aerospace sector, the requirements for the energy storage system (ESS) performance and reliability presented are strict; it should operate with the widest array of storage and operating limits and have the highest performance characteristics of their type while keeping low mass and volume combinations, being secure and trustworthy; and cost-effective [87]. The ESS is responsible for providing the startup power for the engines, the working power for the main computer systems, and emergency power when the engine is inoperative. There are two main applications based on their working environment: endoatmospheric aircraft applications or exoatmospheric aircraft (commonly referred to as spacecraft) applications [21].

In the case of exoatmospheric aircraft, the most critical ESS is used in satellites. Some satellites are fully powered by solar energy obtained from photovoltaic modules; when they enter a dark region, the power supply is no longer available; therefore, they employ very reliable energy sources. Most satellites still utilize nickel-cadmium and lead–acid batteries since they have been on the market for 40 years and are fully developed. LIB appears as an alternative over Ni-H$_2$ and Ni-Cd batteries in the future due to their high specific energy and power density, wide operating temperature range, long shelf life, and lightweight, which is a required point in the design of commercial aircraft, but especially in spacecraft due to the launching cost [21] [23]. According to [23], NMC and LFP are the most suitable cell chemistries for deep space missions as they degrade less than 1% at low temperatures, and there is the potential to maintain over 90% capacity for a 50-year mission [23]. Some of the most important manufacturers of LIB batteries for satellites are Saft and Quallion; examples are the Saft cells used in the Inmarsat 5F-1 Satellite. LIBs are also being contemplated for space stations and other spacecraft once certain issues are addressed [21].

LIBs can be used as an auxiliary or the main power supply for electric propulsion vehicles in the case of endoatmospheric aircraft. For the first case, some examples are the A350, which employs Saft's LIBs for the starting and emergency power supply, and the 787 Dreamliner, which employs the GYLP's LIB [21, 87]. The primary manufacturers of LIB batteries in the commercial and military sectors are GYLP, Cell-Con, ITAR, EPT, and EnerSys [87].

Electric propulsion systems and fully electric aircraft are focused on small passenger capacity for flying short distances, such as transportation to small islands. This kind of aircraft design requires multiple propellers to ensure redundancy; this type of configuration can be observed in Figure 2.5 different types of electric propulsion configurations.
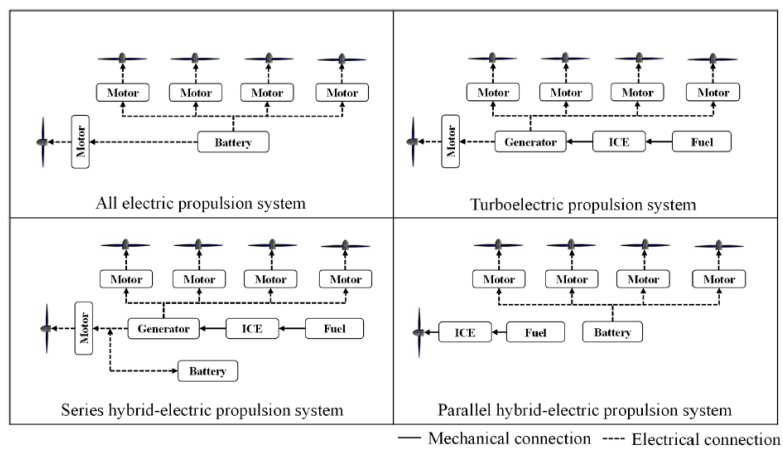

Figure 2.5 : Schematic diagram of four electric propulsion configurations [98]

9

Some of the airplanes, prototypes, and programs related to the production and use of fully electric aircraft are:

- Alice: By eAviation that uses NMC cells. In 2020, a LIB exploded while the aircraft was at the airport [21].

- Electric version of DHC-2 Beaver: MagniX teamed with the small commuter airline in British Columbia Harbour in 2019 to develop this model. Currently, the certification of battery components is estimated to occur in 2025 [30].

- eCaravan: A collaboration between MagniX and AeroTEC, it became the largest fully electric plane to fly in 2020 [21].

- Joby Aero: An air taxi company that was able to fly its first prototype of electric plane with NMC cells. It will have a 4-passenger capacity plus the pilot [21].

- Large Antares 20E: A glider built by Lange Aviation whose first prototype flew in 2003. Its electric motor is fully driven by the propulsion system (approximately 76 kg) of 72 39Ah Li-ion nickel oxide cathode cells in series. It is the first aircraft with an electric propulsion system to get a certificate of airworthiness [21].

- Lilium: Company that seeks to decarbonize transport with electrified solutions. Lilium Jet is the world's first electric Vertical Rake-Off and Landing Jet with zero operating emissions, and without a large-scale ground infrastructure [59].

- Pipistrel: Electric aircraft company focused on the future of sustainable flight. In 2011, they developed the Taurus G4, the most powerful electric aviation motor ever developed (145Kw) at the time, which features a twin-fuselage concept with a large central wing housing [75].

- Vaeridion: Company that seeks zero-emission regional flights with clean and affordable mobility for underserved regions with their electric microliner with a capacity of up to 9 passengers plus crew with a 500 km range. The wings present a high aspect ratio design with integrated batteries, instead of the fuselage, to optimize the structural weight and increase the maximum range. Vaeridium expects their microliners to be operative before 2030 [43].

- Volocopter: Pioneer company in urban air mobility with an emerging branch of fully electric aviation, including taxis, cargo drones, and longer-range passenger aircraft [44].

To minimize the hazardous effect of LIB failure conditions such as TR, their enclosures are typically composed of heavy-weight materials such as aluminum or steel, which negatively affects the lightweight goal [99]. Lightweight and high-performance solutions for enclosures are being pursued by the aerospace industry, such as composite materials alternatives.

2.2 Thermal runaway (TR)

In this section, one of the types of failure listed in 2.1.3 that LIBs present, thermal runaway, will be explained. The causes and stages during thermal runaway and the current studies concerning TR are analyzed in more detail.

2.2.1 Causes

Thermal runaway can occur for several reasons that can be classified according to different criteria. The most common response of a cell to abusive conditions is the generation of heat and gas. According to Liu, Doughthy and Sterling, [63] [37] [83], failures can be classified depending on the type of abusive conditions LIB batteries had suffered; this includes:

- Mechanical abuse or physical damage: Includes puncture, crush, vibration, nail-pierced, or shock. Under mechanical abuse conditions, there is a possibility of creating an internal short circuit within the cell or causing a short circuit within a battery pack, leading to unintended and unanticipated current flow. [37]. Defective materials, i.e., the perforated separators, can also lead to an ISC [26, 27].

- Electrical abuse or charge and discharge failures: Overcharge and overdischarge of rechargeable batteries can occur if there is a malfunction on the control electronics of the charging station or the Battery Management System (BMS) or severe cell imbalance in a battery pack. The thermal response of Li-ion cells during overcharge is largely determined by the cathode chemistry. [37]

    - Overcharge: It occurs due to either the use of an inappropriate battery charger, malfunctions during the recharge phase, or the failure to assess the voltage of the LIB cell [26, 27]. Causes excessive lithium intercalation at the anode or excessive de-intercalation at the cathode [64].

    - Overdischarge: Results from malfunctions in the BMS or in case of severe cell balancing. It can cause a temperature rise, leading to Joule heating and electrochemical reactions [26, 27]. Causes capacity degradation due to the over-delithiation in the anode and amorphization in the cathode.

- Thermal abuse: Heat generation within batteries during abusive tests can increase the danger of failures. A short circuit causes the cell to heat up due to Joule heating, leading to additional heat from internal chemical reactions. Overcharging also produces heat within the cell through oxidative chemical reactions, which can trigger thermal runaway [37]. This type of failure includes overheating due to a malfunction in the thermal management system or a defective cell design

[26, 27]. Overheat refers to an intensive heat generation caused by the passing of high current through a given area [64].

- Short circuit: External short circuit is the most common type of battery abusive condition. Since thermal output is small, cells typically can withstand an external short circuit. Thermal management will dictate if the response of cells will be benign or exhibit thermal runaway. Large cells (over 10 Ah), cells that can sustain very large short circuit currents, cells with higher internal resistance, and cells with low inherent thermal stability are more prone to exhibit thermal runaway. [37]

These types of missuses can lead to an internal short circuit (ISC), and one of the main issues that causes this ISC is overcharging. When a battery overcharges, it reaches its maximum voltage or state of charge (SOC) limit while the charging current continues to pass through the battery. This leads to a safety issue as lithium dendrites are formed inside the battery when it is overcharged for a long time, and they can penetrate the separator, causing an ISC. When a large area of an ISC is formed inside the battery, the energy stored will be released at a high rate, increasing the internal temperature and leading to a potential TR [63].

2.2.2 Stages

When a LIB cell is heated above certain temperatures (130 - 150 ℃), the electrodes and electrolyte set will start a series of exothermic chemical reactions that will lead to a rise in the internal temperature of the cell. From that point on, the cell can dissipate the heat, avoiding an abnormal rise in the temperature, or if the heat generated is more than the heat that can be dissipated, the exothermic processes and the cell temperature will increase rapidly. This increase in temperature can lead to an acceleration of the chemical reactions that will increase the temperature as well, resulting in a TR. [88]

The TR process can be represented by a sequence of stages characterized by numerous studies by experimentation. The sequence of the stages is the following:

- **1st stage**: In the initial stage, the plastic enclosing the LIB starts a melting process, which causes gases and swelling; this effect, plus the incident heat flux that gradually raises the cell surface temperature, leads to a fracture in the gas release and an escape of a small amount of gas [83]. Fu et al. [39], observed a smoldering stage with no flame. This stage is named onset while cells are tested in the lab; in this stage, a source of heat is used to raise the cell's temperature to the onset temperature [37].

- **2nd stage**: At the same time, the SEI layer, where lithium ions move from the cathode to the anode, experiences exothermic decomposition, releasing more heat.

A second SEI layer is formed when the electrolyte passes the broken SEI film and reaches the lithiated electrode. As temperatures rise, the new layer also decomposes, releasing additional heat [83, 39]. Fu et al. [39] observed in their experiments a sustainable flame above the sample; this stage lasts several tens of seconds before the burning process enters the third stage. This stage is called acceleration; as the heat is not dissipated, the temperature rises due to exothermic reactions. These reactions depend on the active material chemistries and the state of charge [37].

- **3rd stage**: A violent reaction takes place between the lithium released from the decomposition of the electrodes and the by-products of the electrolyte decomposition. Consequently, an explosion occurs that leads to the ejection of the cap assembly and a large amount of gas that will ignite afterward. In this stage, the temperature rises approximately from 250 to 750 ℃ in 10 seconds, and a sharp rise in surface temperature occurs [83, 39]. In the Thermal Runaway stage, it is highly unlikely that any intervention or external cooling mechanism could stop the ongoing TR; the self-heating rate of this stage is defined as 10 ℃/min or greater. The timing of thermal runaway can be delayed by minutes, hours, or days since it depends on the particulars of the construction of the battery pack and the operating environment [37].

- **4th stage**: After the explosion, the temperature gradually decreases as the fire consumes the chemical fuels [83] [39].
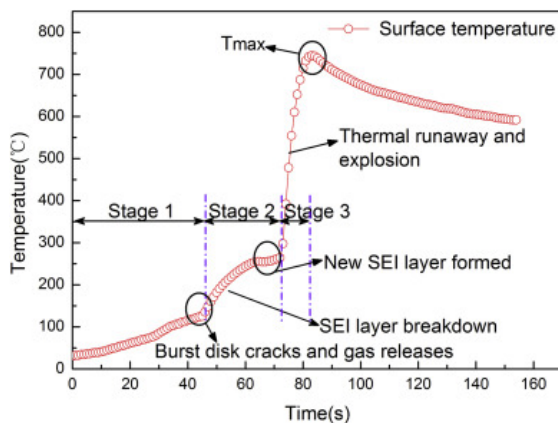
Figure 2.6 : Temperature profile with time of the fully charged LIB under an incident heat flux of 50 kW m^{-2} [39]
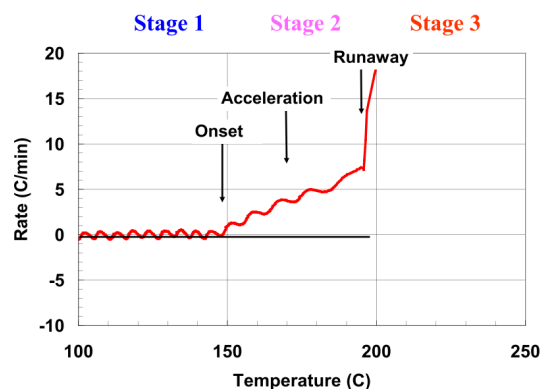
Figure 2.7 : Cell self-heating rate during forced thermal ramp test of Li-ion Gen 2 chemistry [37]

In the Figure 2.6, the sequence of stages explained can be observed for the generalized temperature profile for an 1860 cell undergoing thermal runaway under an incident heat flux of 50 kW m^{-2}. A minor decrease in temperature can be observed at approximately 255 ℃ due to the new SEI layer preventing the electrolyte from continuously reacting

with intercalated lithium. As a result of the TR the surface temperature increases sharply from 264 to 747 ºC within 10 s [39]. In the Figure 2.7, the laboratory stages of onset, acceleration, and runaway can be observed for a Li-ion Gen2 chemistry. Mechanical abuse or physical damage is studied by [57] with the nail penetration method.

Literature review

There are multiple studies that characterize thermal runaway. In Table 2.2, some of the most relevant studies can be found, and it can be observed how different causes explained at subsection 2.2.1 that lead to TR are studied by different experimental methodologies.

In the table, the different methods employed to cause TR on the batteries can be observed; some authors have focused on standardized methods like ISO 5660-1, as [63] and [39], while others select custom design test stands such as [45]. For studying mechanical abuse or physical damage, [89], [41] and [25] use sharp nail penetration. For studying electrical abuse failures, some authors overcharge the cells by ARC or es-ARC, like [38], [90], [48], and [79]. Finally, for thermal abuse studies, some authors employ heating ramps like [89], [45], and [81]; while others employ more innovative methods such as laser-induced triggering abuse methods like [41].

The majority of the studies perform multiple experiments to compare different manipulated variables. The most popular manipulated variables are the SOC ([63], [39],[90], [79], [89],[92], [41]) and the comparison between cell chemistries ([40], [45] and [25]). Other parameters, like different geometries and configurations studied in [57], are also really interesting for this project's scope.

The most common controlled variables used to parametrize the effects of TR are ST (Surface Temperature), VD (Voltage Drop), IT (Internal Temperature), MLR (Mass Loss Rate), and the time needed to reach them. There are other parameters, but most of them depend on the purpose of the investigation; for example, CTG is more related to studies that analyze the composition of the gases due to TR of LIB. It can also be observed that some studies follow a standardized method like the ISO 5660-1, but most of the revised studies follow their own method, which is not standard.

Year	Reference	Type of battery	Method	Equipment	Manipulated variables (input)	Controlled variables (output)
2013	[45]	18650 LFP, NMC, LCO/NMC	Thermal abuse	Heatable reactor, electric feed-throughs, gas feed-throughs, vacuum pump, pressure transmitter, fume hood, removable sample holder, heating sleeve, thermal insulation layer, 10 thermocouples	Chemistries	CTG, ST, HR, p, gas analysis (amount and production rate)
2014	[38]	25 Ah NMC	Overcharge	es-ARC (standard ARC and EV-ARC) N-type and K-type thermocouples	Same battery same experiment multiple test	IR, IT, ST, VD, TD
2015	[39]	UR18650FM	Thermal abuse	Cone calorimeter	SOC	MLR, TI, TE, HRR, ST, CTG
2015	[57]	2200 mAh 18650 and 3000 mAh pouch	Mechanical abuse	Hydraulic press, thermocouples, nail	Geometries and configurations	TI, ST, HRR
2015	[92]	32 Ah prismatic (Ningde Amperex Electronics Technology Co. Ltd. (ATL))	Overcharge	Al Can, K-type thermocouples, cyclic voltammograms, Soltarton 1480 electrochemical workstation	SOC	IT, ST, VD, IR, CVC
2016	[90]	52345 1 Ah	Overcharge	Nickel strips banded with Teflon adhesive tapes, N-type thermocouples, calorimeter, battery cycler	SOC	ST, V, max ST, VD, max V, HRe, AH
2017	[48]	NMC 44 mAh, 88mAh and 264 mAh	Overcharge	ARC, es-ARC, 2 heaters, 2 N-type thermocouples, temperature-resistant tape	Capacities and prevention methods	ST, VD, heat
2019	[79]	40Ah LMO	Overcharge	A and K type thermocouples, ARC, high-temperature insulation Kapton tape, restraining plates	SOC, configurations and heat dissipation condition	IT, ST, IR, V, gas analysis, max ST, max T at TR
2022	[63]	2.6 Ah 18650 NCM523	Thermal abuse	Cone calorimeter, 7 thermocouples	SOC	HRR, ST, FT, MLR

Year	Reference	Type of battery	Method	Equipment	Manipulated variables (input)	Controlled variables (output)
2022	[40]	ICR (Samsung 26J), INR (Samsung 20R), IFR (NX 7063)	Thermal abuse	Continuous Flow Vessel, high-speed camera, thermocouples	Chemistries and environmental conditions	VT, SMT, max ST, TV, TS, SYT, MLR
2023	[96]	NCM battery from Shenzhen Wei Energy Electronic Technology Co., Lt	Thermal abuse	Combustion chamber, smoke exhaust fan, heating plate, battery module (4 cells) fixed iron box, K-type thermocouples	SOC, temperature spacing and mass spacing	ST, ML, MLR, HRe
2023	[89]	157 Ah NMC811/C	Thermal abuse, mechanical + thermal abuse + overcharge	Aluminium plates, ceramic insulation, local heater, pneumatically operated steel nail, pressure vessel, pressure sensors, K-type thermocouples, gas bags, steel net cage, gas collector, Fourier Transform Infrared (FTIR) spectroscopy	SOC and TR methods	TI, ST, max ST, ML, specific total gas production, CTG
2024	[81]	86 Ah lithium-iron phosphate	Thermal abuse	Energy storage chamber, battery module (15 cells), K-type thermocouples, heating plate	Prevention methods	ST, heat utilization efficiency, heat removed from the battery
2024	[41]	LG18650 NMC811	Thermal abuse	Litron's Lasers LD30-527 series, Xenon arc lamp, high-speed camera, hermetic vessel, pressure sensor, 2 K-type thermocouple, voltage sensor, Yokogaya Datalogger	SOC and laser exposure durations	max p at the chamber,0.05V VD, V, max air, max ST (top cell) and their respective time to reach them, MLR

Year	Reference	Type of battery	Method	Equipment	Manipulated variables (input)	Controlled variables (output)
2024	[25]	3Ah LCO, LMO, NMC and LFP	Mechanical abuse	Explosion-proof thermal chamber (Gaoxin GX-3000-80LHB20), cell testing system (Neware CT-4008-5V50A), K-type thermocouple (OMEGA GG-K-30-SLE)	SOC	VD, ST, MLR
2024	[35]	KULR 18650-K330, KULR 21700-K500, Soteria 18650, LG 21700-M50, LG 18650, Saft D-Cell-VES16, Samsung 18650, Sony 18650, MO-LiCEL 18650	Mechanical abuse and thermal abuse	FTR and high-speed X-ray radiography	Chemistries, geometries, capacity, casing thickness, bottom vent and maximum discharge rate	Total Heat, capacity-normalized total heat output, MLR, total heat output, positive heat, ST, negative heat

Table 2.2 : Current literature on characterization of TR of LIB

In Table 2.2, abbreviations are used to make it possible to present the manipulated variables and the controlled variables. In alphabetical order: AH (Acumulated Heat), ARC (Accelerating Rate Calorimetry), CTG (Concentration of Toxic Gases), CVs (Cyclic Voltammograms), CVC (Cell Volume Change), DCS (Differential Scanning Calorimetry), EDS (Energy dispersive spectrometer), EV-ARC (Extended Volume-Accelerating Rate Calorimetry), FT (Flame Temperature), HR (Heating Rate), HRR (Heat Release Rate), HRe (Heat Release), ICP (Inductively coupled plasma), IR (Internal Resistance), ISC (Internal Short Circuit), IT (Internal Temperature), LIB (Lithium-ion batteries), LCO (Lithium Cobalt Oxygen), LFP (Lithium, Ferrum, Phosphate), LMO (Lithium Manganese Oxide), MLR (Mass Loss Rate), NMC (Nickel Manganese Cobalt), p (Pressure), SEM (Scanning electron microscope), SMT (Smoke Temperature), SOC (State of charge), ST (Surface Temperature), SYT (Safety Time), T (Temperature), TD (Temperature Difference), TE (Time to Explosion), TI (Time to Ignition), TR (Thermal Runaway), TRP (Thermal Runaway Propagation), TS (Time Smoke), TV (Time Venting), VD (Voltage Drop), V (Voltage), VT (Venting Temperature), XRD (X-ray diffraction), CTG (Concentration of Toxic Gases), and CVs (Cyclic Voltammograms).

Other studies that characterize the behavior of the TR are those that develop numerical methods for its simulation. These theoretical-simulated investigations go beyond the framework of this project; nonetheless, there are advances regarding the study of TR that deserve to be noted. Some of these studies like [95] in which a numerical model to predict the mechanism of TR triggered by local overheating is developed based on energy

conservation equation and Arrhenius equations; or [80], that derives and validates and non-dimensional parameter (Thermal Runaway Number) whose value governs whether or not TR will occur in LIB.

2.3 Composite materials

2.3.1 Definition

Composite materials consist of a bulk binding material, the resin matrix, that binds the reinforcement component, usually in fiber form, which increases the stiffness and hardness of the resultant material. In Figure 2.8, a schematic diagram of the combination of these two parts can be observed. The result of the union of two or more different but compatible materials is an improvement in the overall properties and functionalities of the resultant material to each constituent component. In addition to the matrix and fiber reinforcements, it can also consist of core materials, fillers, additives, and surface finishes to obtain the best performance characteristics for an application. [31, 51]

Reinforcement + **Matrix (Polymer)** = **Combined Composite**
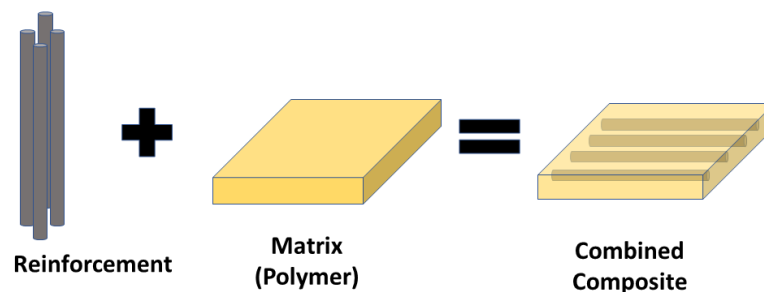
Figure 2.8   : Schematic diagram of a composite material [12]

Composite materials present advantages compared to other traditional materials, such as strength, low weight, resistance to corrosion, design flexibility, and long-term durability [31]:

- Strength: Composites are among the most durable materials; they present a superior strength in relationship with their densities superior to most construction materials.

- Lightweight: Composites are much lighter in weight than most metals and woods, which makes them suitable for reducing the cost of transportation and installation in the case of infrastructure and in the aeronautical sector, reducing fuel consumption and, therefore, the flight cost.

- Resistance to corrosion: Composites have been assessed in environments in which traditional materials would deteriorate quickly due to exposure to harsh weather and chemicals.

- Flexibility: Composites may be modified to meet the precise requirements of any given use; versatility stems from the wide variety of possible material combinations, from being simple to forming intricate designs.

The two basic parts of a composite material and the different types within each part will be explained in detail in the following sections, introducing the compounds used in the project.

2.3.2 Matrix

Matrix or resin systems constitute a high-volume fraction of the composite material. Resin systems should present good adhesive and mechanical properties to resist environmental and service degradation [51]. The main functions of the matrix are [31]:

- Serve as a stress transfer mechanism between the reinforcing fibers.

- Behave as a bonding mechanism to maintain the fibers intact0

- Operate like a shield that protects the fibers from mechanical and environmental fibers.

The three main functions can be summarised as allowing an efficient load transfer mechanism while preventing debonding during stress cycles and avoiding cracking and delamination, the main problems that affect composite materials when used as load-bearing structures. The selection of the resin for a specific application must be tough enough to resist crack propagation. [51]

Classification

In this subsection, the different classes based on the matrix and reinforcement material are defined:

- **Metal matrix composites (MMCs)** combine metal with another material; some examples are Aluminium MMCs, Magnesium MMCs, and Titanium MMCs [31]. The advantages are high-temperature capability, fire resistance, and high electric conductivity. Nevertheless, they have disadvantages such as a higher cost of some

material systems, more complicated production methods, and relatively undeveloped technology [13, 52].

- **Polymer matrix composites (PMCs)** are made of a polymer (resin) matrix and a fibrous reinforcing phase spread throughout the matrix; some examples are GRP, CFRP, and aramid (Kevlar) [31]. They present some advantages, such as good stiffness and strength and high performance and durability, and disadvantages, like sensitivity to radiation and moisture and a lower maximum working temperature compared to other composite materials [52].

- **Ceramic matrix composites (CMCs)** are made out of a ceramic matrix and a ceramic reinforcement (refractory fibers). Supplementary fibers can be added for reinforcement; in this case, they can be classified as a subset of both composites and ceramics [31]. Some of their advantages are higher chemical stability and fatigue endurance, while some of their disadvantages are lack of ductility, repairing difficulties, and they are exposure to thermal cracking [52].

At Table 2.3, the main differences already introduced previously between the three main types of matrices can be found. The selection of the proper matrix will depend on the requirements for the specific application.

Property	PMC	MMC	CMC
Modulus	Medium	Very high	Very high
Cost of processing	Low	Medium	Very high
Processing techniques	Easy	Difficult	Reasonable ease
Density	Low	Medium	Low
Creep resistance	High	High	Low
Fracture toughness	High	Medium	Low
Fatigue resistance	High	Medium	Low
Tension	Very high	High	Medium
Compression	High	High	High
Diversity of use at room temperature	Extensively used	Moderately used	Rarely used
Diversity of use at high temperatures	Rarely used	Moderately used	Highly used
Thermal conductivity (Anisotropic in nature)	Low	High	Oxide CMCs are good insulators
Wear resistance	Good	High	Very high
Corrosion resistance	Very high	Low	Good

Table 2.3 : Comparative analysis between PMC, MMC and CMC from [52]

Polymer matrix composites (PMCs) classification

The final scope of this project is to analyze the behavior of certain PMCs under the effects of TR of LIB batteries. The aim of this subsection is to delve into this type of matrices and their types.

Polymeric resin systems typically employ either thermoplastic or thermoset resins in their construction. Resins can be classified into:

- **Thermosets**: Most frequently used, especially for structural applications. After the cross-linking polymerization, they became solid materials whose resins are irreversible. The resins are cured by heat, catalyst, or both to obtain the final material. Some examples of typical structural thermosets are [31]:

  - Epoxy: This group concerns various cross-linked polymer chains based on polymer monomeric units containing an epoxide group. they are usually formed by the reaction between diepoxide and a primary. Reactants with higher reactive functionalities are used for aerospace applications since they result in a highly cross-linked, stiff, and tough epoxy network. This type of resin is lightweight and has increased adhesion, reduced degradation from water ingress, and increased resistance to osmosis. Epoxy resins normally have outstanding functionalities and material properties compared to unsaturated polyester resins or vinyl esters, though their use is limited due to their high cost. [51]

  - Polyurethane: This is obtained by the reaction between diisocyanate and polyester diol. They are a very versatile class of polymers with different applications: rigid foam insulation of walls, flexible foams in furniture, the automotive industry, and insulation material in fridges. A disadvantage of this type of resin is its poor properties in thermal, mechanical, and corrosion resistance characteristics in severe environments. [36, 52]

  - Phenolic: Obtained by the reaction of phenols with simple aldehydes. They are mostly used where high fire resistance is critical despite being brittle and not possessing high mechanical properties. They are used to make molded products, coatings, and adhesives, and they can be found in aeronautical and aerospace vehicle construction in which, during atmospheric re-entry, the vehicle is subjected to severe aerodynamic heating, and the phenolic converts to an ablative char. [29] [51]

  - Unsaturated polyester: Consists of prepolymer mixtures containing unsaturated groups and styrene (serving as a diluent and cross-linking agent during the radical polymerization process) [9]. Most of this resin type is cured at room temperature, yet catalysts, accelerators, and heat can be used to speed up the reaction. Some of their advantages are easy processibility, good mechanical, water, and corrosion resistance properties, and relatively low cost. Their main uses are linked to marine, automotive, and construction applications. A disadvantage of this type of resin is the environmental impact of the material during its production process [51].

  - Vinyl ester: The structure of this type of resin is similar to unsaturated polyester resins with a difference in the location of the primary vinyl re-

active groups, which are positioned at the ends of the monomeric chains. Unlike unsaturated polyesters, they offer better mechanical properties and are less prone to hydrolysis damage since they contain fewer ester linkages. [51]

- **Thermoplastics**: These resins are not cross-linked; the final material is reversible and can be reshaped as many times before it is permanently damaged. Some examples of common thermoplastics are [31]:

  - Acrylonitrile Butadiene Styrene Acrylonitrile butadiene styrene (ABS): This type of polymer is composed of the three main monomeric chemical compounds that compose its acronym, acrylonitrile, butadiene, and styrene. Some advantages of ABS are its high impact strength, processing simplicity, low cost, and a good mix of mechanical, electrical, and thermal properties. [52]

  - Polycarbonate (PC): It is produced by reacting bisphenol A and carbonyl chloride in an interfacial process. PC is an amorphous engineering thermoplastic material with exceptionally high impact strength, transparency, low density, chemical stability, high dimensional stability, moderate temperature resistance and ease of processing. These properties make PC one of the most widely used thermoplastic materials. Other characteristics are its glass transition temperature of 148°C, high gloss finishing, low mold shrinkage, and low moisture absorption properties. It also has high corona resistance and insulation resistance properties. This material can be compounded to produce resins for sterilizability, flame retardant, stain resistance, and fiberglass and mineral reinforcements with various additives. These can enhance the final material's thermal stability, UV stability, tensile strength, stiffness, and flame retardants. [20, 33]

  - Polyether ether ketone (PEEK): This material is a member of the PAEK (poly aryl ether ketone) family of thermoplastics used for high-performance applications in aerospace. The main characteristics of this semi-crystalline family are low flammability, high thermal stability, glass transition temperature, corrosion resistance, and mechanical performance over a wide temperature range. PEEK is a semi-crystalline thermoplastic with a linear, highly aromatic molecular backbone that includes ether and ketone rings. Due to the crystalline nature of the material, the resins obtained have a great mix of physical qualities like strength, chemical resistance, and hydrolytic thermal stability. Its glass transition temperature is around 160ºC while its melting temperature is around 345ºC. [16, 84]

– Polyphenylene sulfide (PPS): It is a high-performance polymer whose structure consists of benzene and sulfide atoms alternately arranged repeatedly. Due to the rigidity of the benzene ring and robust semi-crystalline aromatic, the polymer presents great thermal and chemistry stability. Another advantage of this type of matrix is the limiting oxygen index (LOI), which is over 35%; this parameter indicates an excellent self-extinguishment in air. PPS material has been tested to be a great alternative for the LIB separators as it satisfies the safety requirements. [91]

– Polyethylene terephthalate (PET): It belongs to the polyester family of polymers. It shows a higher range of mechanical properties, such as higher stiffness and Young's modulus, than other polymers. Other characteristics of this material are that it is aromatic, has low permeability and is semicrystalline, has a low cost, and is easily available. It is used in a wide range of applications, like food packaging and fire retarding materials. [52]

– Polystyrene (PS): It is a synthetic aromatic polymer made from the monomer styrene.[97]. PS is mainly employed in insulating materials and noise-absorbing screens for the construction industry, medicine, utilities, and food industry. Polystyrene foam is commonly used for small UAV-fixed wing filling due to its good damping properties and low weight. [53, 19]

Thermoplastics can be organized according to their polymer families and their temperature resistance. The three polymer families are amorphous, semi-crystalline, and elastomers; they are also subdivided into three thermal categories: standard or commodity materials, engineering or performance materials, and high-performance materials. This classification of thermoplastics can be observed in Figure 2.9. Thermoplastics with an amorphous structure are commonly transparent and have higher toughness and high-dimensional stability; they are suitable for high-precision parts. Semi-crystalline thermoplastics are typically opaque, rigid, and have good chemical resistance. Thermoplastic elastomers (TPE) present a heterogeneous structure of flexible and rigid domains; this type is located midway between thermoplastics and crosslinked elastomers. [49, 82]
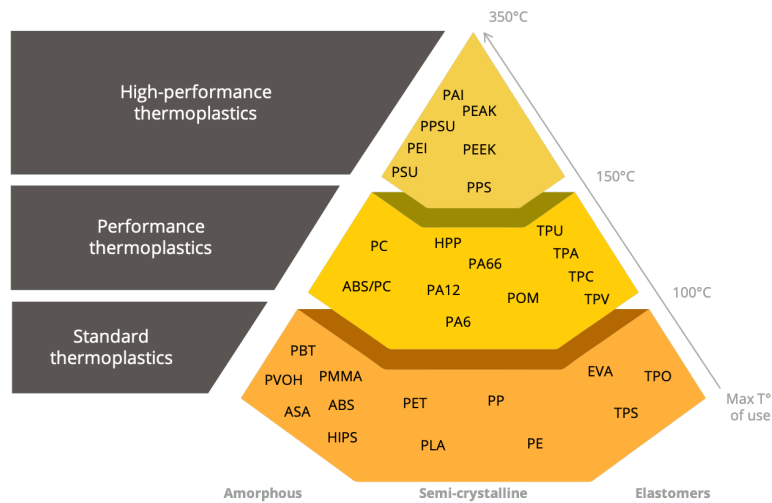
Figure 2.9 : Pyramid of thermoplastics according to their temperature performance [49]

2.3.3 Reinforcement

Reinforcements shall be orientated to match end-product loads and user design criteria; they increase the mechanical properties of the consolidating polymer resin matrix.

Reinforcements for composite materials can be classified by shape: particles, whiskers, or fibers. Particles have no preferred orientation, and their improvements in the material's mechanical properties are minimal; they are mainly used as fillers to reduce the final material cost. Whiskers are single crystals shorter in length and diameter than fibers; they are extremely strong but difficult to disperse uniformly in the matrix. Fibers are usually circular or nearly circular and have a very long axis compared to particles and whiskers; they are significantly stronger in this direction. Fibers are the most common reinforcement for advanced composites due to their strength and stiffness. Likewise, fibers can be classified as continuous or discontinuous, depending on the application and manufacturing process [32]. Due to the use of fibers for advanced composite materials, the rest of the section will focus on this last type of reinforcement.

In addition to the mechanical and interfacial (fiber-resin properties) properties, other factors should be considered when designing a composite, such as the fiber orientation through the composite and the fiber volume fraction. Varying these factors, the material can be optimized, obtaining a greater performance, a weight reduction, and or lower fabrication-related expenses. [51, 31]

The orientation of most reinforcement is based on uni-directional, chopped, braided, stitched, and woven fiber rovings. Uni-directional orientations are preferred for high-performance composites like in aerospace applications. [51]

The most common fibers for structural applications are [51]:

- **Glass fibers (GF)**: Due to the low cost and high strength-to-weight ratio, glass fibers make up over 90% of reinforced plastics [31].

  – C-glass (chemical) has good resistance to chemical attacks, and it can be found as the outer layer in laminates for applications in water pipes and chemical storage tanks.

  – E-glass (electrical) has good electrical properties and good mechanical properties (tensile, compressive strength, and stiffness), and it is cheaper compared to other glass fibers.

  – S-glass (high strength) has a higher modulus and tensile strength than E-glass but is more expensive. Due to these properties, these fibers can be found in applications where safety and protection are more important than cost, like aerospace and hard ballistic armor applications.

- **Carbon fibers (CF)**: This type of fiber is produced via thermal treatment of carbon-containing precursor fibers commonly made of cellulose, pitch, and poly-acrylonitrile precursors due to its superior fiber properties. Carbon fibers have the best properties regarding tensile strength and stiffness compared to the rest of the fibers, and they are also highly resistant to corrosion, creep, and fatigue. However, they have lower impact resistance in comparison with GF, and they are more expensive.

- **Aramid fibers**: Highly crystalline aromatic polyamides are obtained by rotating the liquid crystalline polymer solutions into thin threads and stretching them to augment stiffness. They are highly anisotropic and have very high specific strength(high strength and low density). Yet, they are not recommended for compressive load application and are more expensive than GF.

2.3.4 Aerospace applications

Composite materials present advantages in comparison with other traditional materials such as strength, low weight, resistance to corrosion, design flexibility, and long-term durability, as stated at the beginning of the chapter [31]. These characteristics make composite materials suitable for a wide variety of applications, such as aerospace, automotive, and biomedical industries, among others.

In the space sector, composite materials have been employed for the past few decades in various spacecraft systems, including those that transport humans, satellites, payload supports, and launch vehicles. Due to their low weight and resistance to extreme temperatures in space, composites are needed for spacecraft. One of the first examples is the use of composites during the Apollo program, which were used for ablative and other high-temperature components, including rocket motor nozzles and re-entry heat

shields. Other examples are the optical benches and other precision constructions; these are always made of carbon fiber laminates with low moisture absorption resins, usually cyanate ester, to maintain dimensions in space's vacuum and extreme temperatures. [31]

Top manufacturers in the aviation industry, like Airbus and Boeing, have shown that composite materials could be used on a large scale. As shown in Figure 2.10, the use of composites has increased exponentially in the last two decades for both military and civil applications. The considerable growth in their use is attributed to the key benefits and versatility of employing different types of composites for different types of applications that can address most of the critical requirements for aerospace materials [31, 77]:

- Lightweight: Composites are much lighter in weight as compared to metals; composite use entails a weight reduction of somewhere between 20 and 50%, which, therefore, achieves considerable fuel savings and makes aviation more sustainable.

- Structures made of a single shell may have increased strength while maintaining a reduced overall weight. Structures should have high static strength to be resistant to extreme forces due to wind shear and other high transient forces.

- A remarkably high resistance to impact against sudden impacts of various types (eg, bird strikes, foreign objects, etc.).

- High resistance to thermal instability.

- Resistance to fatigue and corrosion.

- Structural components constructed of composite materials are directly arranged together; therefore, to metals, composite materials require fewer joints and rivets, leading to higher aircraft reliability and lower susceptibility to structural fatigue cracks.

- Multifunctionality: Composites can provide outstanding dimensional stability under a wide range of temperatures, resistance to lightning strikes, hail, and corrosive environments, and improved fire, smoke, and toxicity performance.

- High fracture toughness and damage tolerance: The cracks and flaws present in the structures should not grow quickly leading to sudden failure of the structures.

- Shielding of electromagnetic waves.
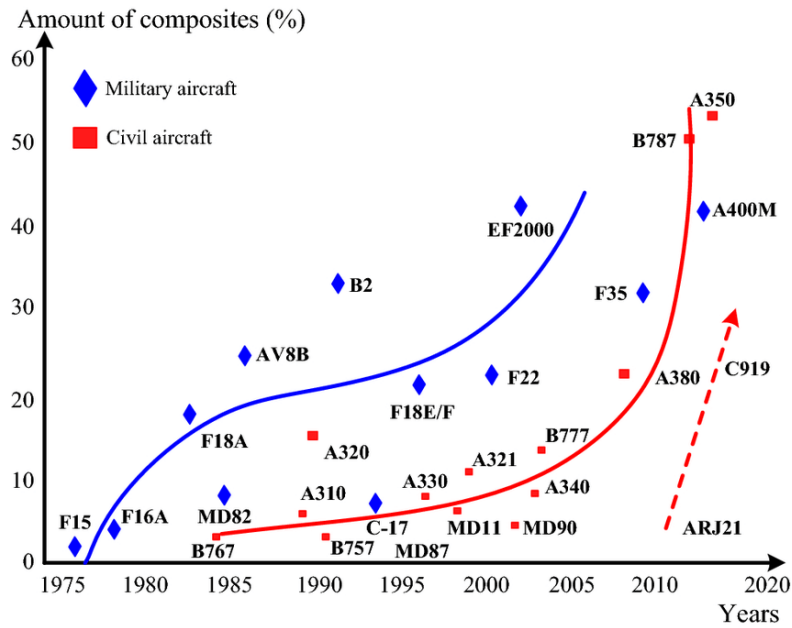
Figure 2.10 : Amount of composites used in military and civil aircrafts [94]

In aerospace applications, carbon/epoxy composites are predominantly used in primary structures such as the fuselage, wings, tail fin components, control surfaces, and doors. Cabin interiors in passenger aircraft are largely made from polymer matrix composites, mainly glass/phenolic [51]. Composite materials have also been used in other primary and secondary structural parts like antenna structures, compressor blades, fan blades, flywheels, transmission structures in helicopters, jet engines, radar, solar reflectors, turbine blades, turbine shafts, rotor shafts in helicopters, wing box structures, radomes, antenna dishes, engine nacelles, stabilizers, center wing boxes, aircraft wings, pressure bulkheads, engine cowls, flap track panels, and so on[31, 77].

Some examples of military and civilian aircraft that are built with a high amount of composite materials in their airframes can be observed in Figure 2.10 [94]. The most relevant example is the Boeing 787 Dreamliner, a twin-engine, long-range aircraft with a wide-body cabin and a lightweight composite frame that accounts for 80% of its capacity. Additionally, the aircraft is composed of ten percent steel, fifteen percent titanium, twenty percent aluminum, and five percent other elements. A schematic representation of the material selection can be observed in Figure 2.11. This material selection accomplished significant weight reductions, realizing significant cost savings, as a result [31, 77, 42].

27
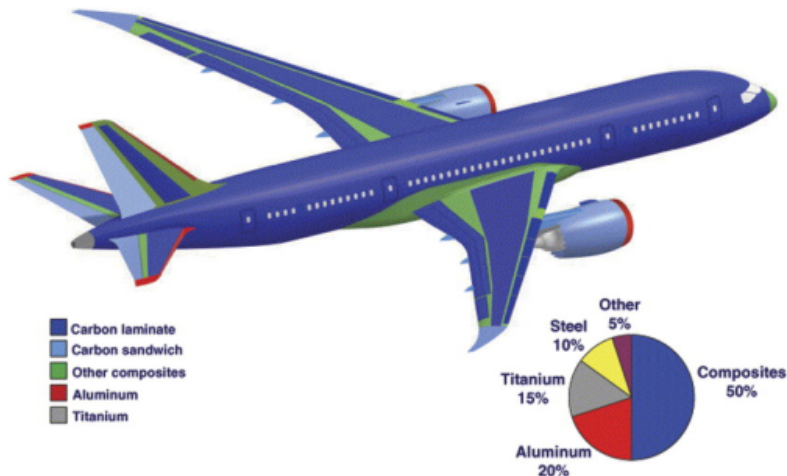
Figure 2.11   : Material distribution on the Boeing 787 [42]

A few challenges still exist regarding the use of composite materials in modern aircraft and spacecraft. One of them is the complex structure of composite materials, which leads to difficulty in detecting various damages. The repair of composite structures takes more time as compared to repairing the metallic frames. Another problem with composite materials is the limited information on the behavior of composite structures due to less experience with composite airframes and parts as compared to metallic designs [77]. That said, this project aims to face the latest challenge that composite materials currently present and investigate their response to an extreme thermal situation, in this case, the TR of LIBs.

2.3.5 Fire resistance and fire reaction properties

The aim of this subsection is to summarize some of the most relevant and recent studies regarding the fire resistance and fire reaction properties of different composites. Fire resistance is defined as the ability of a material to impede the spread of fire and retain mechanical integrity, and fire reaction defines the flammability and combustion properties of a material that affect the early stages of fire, generally from ignition to flashover [2]. In order to completely understand the selected bibliography is required to explain beforehand the meaning of the main properties.

- **Time to ignition (TI)**: Period of time when a material starts burning, the period that a combustible material can withstand exposure to a continuous heat flux before igniting and experiencing sustained flaming combustion. This parameter can be used as a rough measure of the flammability resistance. The measuring unit for TI is the seconds [s]. [67]

- **Limiting oxygen index (LOI)**: It is the minimum concentration of oxygen in a mixture of oxygen and nitrogen needed to sustain flaming combustion; quantifies

28

the flammability of composite materials. The greater the LOI value, the greater the concentration of oxygen required to maintain the combustion of a material after it has ignited. A high LOI is desirable to minimize a potential fire hazard [67, 1, 2].

- **Peak heat release rate (PHRR)**: The maximum amount of heat liberated by a material during the combustion process. It is a transient property but a great indicator of the flammability of a material. Large PHRR values are usually highly flammable, contributing more to the growth and spread of fire. The measure units of PRR are thermal energy per surface area of the material [J/m^2]. [67, 2]

- **Average heat release rate (HRR)**: It is the total heat released averaged over a combustion period of three or five minutes and measures the heat contribution to a sustained fire. It is the most important fire reaction property of polymer composites, as the amount of heat released by decomposing materials can contribute to the growth and spread of fire. The lower the HRR, the lower the fire hazard of aircraft composites. The measure unit of HRR is thermal energy per surface area of the material [J/m^2]. [67, 2]

- **Total heat release (THR)**: Total amount of thermal energy released from decomposing composite material. The lower the total heat release, the less of the composite will contribute to the temperature of a fire. The measuring unit of THR is the Joules [J]. [67]

- **Flame spread rate (FSR)**: It describes the speed at which flames spread over the surface of a combustible material. This factor is crucial in determining the growth and spread of fire. [67, 2]

- **Flame spread index (FSI)**: It is a comparative dimensionless measure expressed, derived from visual measurements of the spread of flame versus time. FSI indicates the speed at which flames spread over the surface of a composite material, meaning a high value of a fast flame spread. [67, 1]

- **Smoke/ Toxicity (S/T)**: Smoke is defined as airborne suspension of solid and liquid particles evolved when a material undergoes pyrolysis and combustion. Toxicity is the propensity of smoke to produce adverse biochemical or physiological effects. The gas that often has the greatest individual hazard is carbon monoxide (CO) and is measured in parts per million [ppm]. [67, 1]

- **Mass loss (ML)**: Wight change of the material after this is exposed to fire, expressed in percentage [%]. [1]

- **Extinction flammability index (ESI)**: This index measures the flammability of composite material, it is determined by plotting the average HRR against the incident heat flux. [1]

- **Smoke density (SD)**: It is the concentration of smoke particles within the plume of a fire. [1]

- **Thermal decomposition (TD)**: Temperature of the polymeric matrix at which mechanical and physical properties of the material can degrade, impacting their long-bearing capacity. [86]

- **Fire performance index (FPI)**: Corresponds to the ration of TI to PHRR. This parameter is dimensionless. [1]

The bibliographic research summarized in the Table 2.4 highlights several significant trends and advancements in the study of composite materials and their fire resistance and fire reaction properties. Recent research has shown a growing emphasis on understanding the thermal and fire characteristics of various composites, particularly in aerospace and structural applications. For instance, [34] focuses on materials like CF/PPS and CF/PEEK. These studies investigate how fiber orientation and polymer matrix degradation impact fire performance, emphasizing the need for improved flame resistance in high-performance materials used in aerospace and other demanding environments.

The experimental test parameters more recurrent are: Heat Release Rate in [65], [93], [58], [76], [72], [18], [24], [54], [17]; Mass Loss Rate in [76], [24], [65], [54], [72], and [93]; Limiting Oxygen Index in [58],[18], [17], [54], [65], and [93]; and Smoke/Toxiciy in [93], [58], [47], [76], and [65].

Additionally, the research from 2023 and 2024 demonstrates a concerted effort to enhance the fire-retardant properties of polymers through the incorporation of various additives and fillers. Furthermore, the mechanical properties of composites are also studied in various research studies that address the critical need for materials that perform reliably under extreme conditions.

In addition to the characteristics previously explained, the rest of the acronyms in the Table 2.4 correspond to: EHC (Effective Heat of Combustion), EG (Expandable Graphite), FIGRA (Fire Growth Rate), FR (Fire Retardant), MLR (Mass Loss Rate), PHRT (Peak Heat Release Temperature), PSPR (Peak Smoke Production Rate), RW (Residual Weight), SPR (Smoke Production Rate), TSP (Total Smoke Production), TSR (Total Smoke Release), THE (Total Heat Evolved), TPHR (Time to Peak Heat Release), AlPi (Aluminum Diethyl Phosphinate), AS (Ammonium Sulfamate), BMI (Bismaleimide), CaAl-LDH (Calcium Aluminum Layered Double Hydroxide), CF/PPS (Carbon Fiber Reinforced Polyphenylene Sulfide), DOPO (9,10-Dihydro-9-Oxa-10-Phosphaphenanthrene-10-Oxide), GF/PET (Glass Fiber Reinforced Polyethylene Terephthalate), GF/PETG (Glass Fiber Reinforced Polyethylene Terephthalate Glycol), GF/PC (Glass Fiber Reinforced Polycarbonate), GF/PPS (Glass Fiber Reinforced Polyphenylene Sulfide), GF/PP (Glass Fiber Reinforced Polypropylene), MPP (Melamine Polyphosphate), and ZnPi (Zinc Diethyl Phosphinate).

Year	Reference	Composite material (Fiber + resin)	Experimental test parameter	Purpose of the study
2020	[76]	PEEK matrix	MLR, ML, S/T, HRR	Investigation of thermal and fire behaviors of PEEK
2021	[72]	PA/GF25, PA/GF-RP1.5, PA/GF-RP6.0	PHRR, HRR, ML, MLR	Study of the combustion behavior of multi-component flame retardant (FR)
2021	[47]	PPS/GF, PPS/CF, PET/GF, PETG/GF, PP/GF (FR), PC/GF	SD, S/T, FSI	Material screening for floating crew floor
2023	[18]	MPP, DOPO, AlPi, ZnPi, PA6, PA6/CF, PA6/CF with several concentrations of MPP, DOPO AlPi and ZnPi	Effects of phosphorous fire retardants on CF composites	
2023	[24]	PS, PS-FR, PS-FR-PPE(S), PS-FR-PPE(F), PS-FR-PPS(S), PS-FR-PPS(F)	LOI, TI, PHRR, THR, FIGRA, SPR, PSPR, TSP, MLR, ML	Investigation on non-flammable and fire-proof thermoplastics with lower flame retardant (FR)
2023	[17]	PA6/CF, PA6/CF/10EG, PA6/CF/20EG, PA6/CF/30EG	PHRR, HRR, TI, THE, EHC, FPI, LOI, ML, stress, strain	EG effect as fire retardant
2023	[54]	PPS, PPS/GF, PPS/GF/10CaAl-LDH, PPS/GF/20CaAl-LDH, PPS/GF/10 m-CaAl-LDH, PPS/GF/20 m-CaAl-LDH, PPS/GF/30 m-CaAl-LDH, PPS/GF/40 m-CaAl-LDH	LOI, MLR, tensile strength	Study of the addition of CaAl-LDH as a FR filler

Year	Reference	Composite material (Fiber + resin)	Experimental test parameter	Purpose of the study
2023	[58]	GF/BMI	TI, PHRR, time to PHRR, THR, TSR, RW, LOI, SD, S/T	Characterization of thermal and fire properties of GF/BMI composites used for aircraft
2023	[93]	PC/ABS, PC/ABS/BDP, PC/ABS/BDP/SMA-SiO2-0.5, PC/ABS/BDP/SMA-SiO2-1, PC/ABS/BDP/SMA-SiO2-2, PC/ABS/BDP/SMA-SiO2-3, PC/ABS/BDP/SiO2-1	ML, MLR, LOI, HRR, THR, S/T, SPR, TSP, tensile strength, elongation at break, notched impact strength	Study of the mechanical properties and flame retardant improvements
2024	[34]	CF/PPS, CG/PEEK	ML, TD	Study over thermal degradation of the polymer matrix for the aerospace field
2024	[55]	CFRP epoxy resin	LOI, FSR, FSD, HRR	Fiber orientation vs opposed-flow flame spread
2024	[65]	PA6, PA6-AS, PA6-PPS(S), PA6-PPS(S)-AS, PA6-PPS(F), and PA6-PPS(F)-AS	LOI, PHRR, HRR, PHRT, TPHR, FIGRA, ML tensile stress, tensile modulus, elongation break	Flame retardant properties in PA6 though PPS and AS
2024	[86]	CF/PEEK	TD, creep	Quasi-isotropic laminates exposed to one-sided thermal aggression from a cone calorimeter

Table 2.4 : Current literature on fire resistance and fire reaction properties of composites

2.4 Standard and literature review on the thermal performance of battery enclosure materials

This section aims to analyze the current studies and standards that specifically analyze the reaction of different materials to TR of LIB. Here, the studies and standards that are close to the scope of this project are listed, as it can be observed the current academic investigation joining the comparison of the thermal behavior of different materials and the TR of battery is limited in comparison with the studies that only investigate the thermal behavior of the materials or the TR of LIBs.

2.4.1 Standard test method

The UL 2596 test method, [8], aims to standardize the requirements for the thermal and mechanical performance of battery enclosure materials in response to the TR of LIB. The objective of the standardization is the comparison of different materials' performance during TR but not a correlation of its behavior with its performance in the end-use application [8].

The test method specifies the conditions of the material test samples, the test apparatus, the instrumentation, and the fuel package. Moreover, it specifies the test method procedure and the information that should be recorded for the report. For more detailed information due to copyright reasons, it is recommended to consult the official norm. The tests developed in this project will follow the standardization of the UL 2596 as far as possible.

2.4.2 Literature review on the thermal performance of battery enclosure materials

Introduction of a battery enclosure thermal runaway material screening program for electric vehicles

This paper, [70], describes the basis of the technical requirements at a system level, the background on the landscape of test protocols identified, and an outline of the new protocol developed, including results from a cross-section of materials using the new test protocol.

An enclosed specimen-level test method is designed to repeatedly test the materials under the combined effects of the TR (temperature, ablation, and pressure). This test procedure aims to quantify material endurance to representative real-world conditions. Another purpose of the method is to develop an early material screening program that

allows quick iterations and enables new materials in the design and assembly considerations for balancing system cost and weight while maintaining performance.

In the test, a method developed, an array of 5 x 5 of 18650 lithium-ion (Li-ion) cells, is selected to perform the experiments based on the relative energy density, commercial availability, consistency, and expected long-term availability. The test apparatus consisted of a 5-sided welded plate steel box with a bolted perimeter flange with a test panel of 200 mm x 200 mm x 2 mm secured to the top of the box and retained by a plate steel bolted flange. The test apparatus is sealed with the exception of the specified flat plate orifice and instrumented with thermocouples to measure temperature during the test. The chamber area the samples are exposed to is 100 mm x 100 mm, with the sample thickness set at 2 mm.

For the experiments, preparation calculations and a series of trials are conducted to confirm appropriate orifice sizes for the relevant enclosure pressures. In order to achieve an induced TR, they placed two resistive heaters wired in series and wrapped them around the two centermost cells in the array. The cells are heated at a rate of 6 °C per minute until the TR event is initiated when the rate of temperature rise exceeds the heating rate [70].

The materials studied for testing the TR test protocol were [70]:

- Steel.
- Thermoplastic reinforced with discontinuous glass fiber.
- Thermoplastic reinforced with continuous glass fiber.
- Thermoset reinforced with discontinuous glass fiber.
- Thermoset reinforced with continuous glass fiber.
- Metal/polymer sandwich reinforced with discontinuous glass fiber.
- Metal/polymer sandwich reinforced with continuous glass fiber.

The failure modes observed after the test were [71]:

- Perforation.
- Rupture.
- Matrix failure.
- Delamination.

The preliminary results from this study show that the test protocol was capable, repeatable, and effective in screening various battery enclosure material specimens [70].

Fiber-Reinforced Polymer Material Screening under Thermal Runaway Conditions for Li-ion Battery Enclosure

This project, [99], tests different composite materials under TR conditions. For this purpose, a decision matrix method is developed to select the most suitable materials. The main materials used for the experiments were a steel box of 120 x 120 mm and an orifice of 15.25 mm in diameter, a battery holder, arrays of seven 21700-type cells, a microcontroller, two heating foils, a temperature sensor amplifier, a transistor, and a power supply.

For the analysis of the experiments, several properties are analyzed in this project: time to reach TR, temperature at TR, maximum temperature, and initiator cell max. temperature, heating rate, and mass loss, among others [99].

The fibers and the resins tested were [99] :

- CF fiber with EP (Epoxy), PA6 (Polyamide), PC (Polycarbonate), PI (Polyimide), PH (Phenolic), PPS (Polyphenylene sulfide) and PEEK (Polyetheretherketone).

- GF fiber with EP, PA6, and CE (Cyanate ester).

- C/GF fiber with PA6.

The study shows that the resin that exhibits the best fire properties under TR is PA6 resin-reinforced PMCs with glass fiber. The study also shows that thermoplastic resins exhibit high fire resistance, and carbon-reinforced PEEK, PPS, and PI and glass fiber-reinforced CE are suitable for high-temperature applications [99] . Based on the results obtained in this study, the materials to be studied in the present study were selected.

Composite structure failure analysis post-Lithium-Ion battery fire

The work [83] develops Finite Element models to asses thermal and mechanical damage and failure mechanisms during a TR considering a section of a battery enclosure. The study employs data for a cylindrical 18650 LIB fire to represent the thermal loading.

The project aims to develop a thermo-mechanical model and a residual strength model. For the thermo-mechanical model, the temperature-dependent CFRP material properties selected are resin decomposition, fire ablation, Temperature, density, specific heat, energy released, fiber thermal conductivity, transverse thermal conductivity, and thermal conductivity through thickness.

Single-cell runaway on composite specimens and multi-cell runaway on composite specimens were simulated, concluding that the presence of damage from a single-cell runaway can potentially reduce the strength of the specimen by 20% while multi-cell runaway can potentially reduce the strength by 56%.

Heat transfer analysis through hybrid FRP composite for self-sensing lithium-ion battery enclosure

This work focuses on studying a hybrid carbon and glass Fiber Reinforced Polymer (FRP) composite designed to replace the traditional metal LIB enclosure and lightweight the EV design. This study aims to lay the groundwork for a self-sensing condition monitoring LIB enclosure and characterize the composite enclosure's temperature response at different layers. A theoretical design of the said system is detailed, and experiments performed to measure the temperature response of the self-sensing composite prototype when exposed to TR are performed using a prototype enclosure sample instrumented with temperature sensors. A computational model is developed to predict the composite's thermal response during different LIB failure temperatures and provide design optimization information. [68]

3 Materials and Experimental Method

In this section, a summary of the main materials and the experimental method followed is detailed.

3.1 Materials

In this section, the main necessary materials for carrying out the TR test are listed, as well as the relevant technical data related to the project's purpose. In addition to these materials, it should be noted that the necessary materials and protective measures are also employed, such as latex gloves, thermal protection gloves, protective overalls for the body and clothing, ear plugs, and masks with filters for gas protection.

Kapton tape holds the batteries and thermocouples due to its resistance to very high temperatures. Masking tape is used to avoid reflections. An emissivity tape for measurements on reflective surfaces with an emissivity coefficient of 0.95 for more precise measurements of the samples with the thermal camera. This tape has a consistent emissivity, meaning it efficiently emits infrared radiation. By applying this tape to the sample surface, the emissivity at this point is known, allowing the thermal camera to take more reliable measurements and reduce errors caused by reflections.

3.1.1 Fiber Reinforced Composite Materials

For the material screening process, 5 different composites were tested; those composites resulted from combining the matrix materials PEEK and PPS with 2 different fibers, CF and GF, and the matrix material PC with CF. In this section, information regarding the technical data provided by the manufacturer and the number of different samples tested for each material is summarized at Table 3.1 .

One sample of CF/PC (Tepex® dynalite 210fr-C200(x)/45% 3K Carbon - PC flame retardant consolidated composite laminate, Bond-Laminates, Germany) is tested by the single 4695 TR test, this sample is labeled as CF/PC 1.

Three samples of CF/PEEK (TECATEC PEEK MT CF50 S280 CP/IP/OS V01 natural, Ensinger, Germany) are tested by the multi-cell 21700 TR test; these samples are labeled as CF/PEEK 1, CF/PEEK 2, and CF/PEEK 3; and one sample of CF/PEEK is tested by the single 4695 TR test; this sample is labeled as CF/PEEK 4.

Three samples of CF/PPS (TECATEC PPS CF50 T200 CP/IP/OS V01 natural, Ensinger, Germany) are tested by the multi-cell 21700 TR test; these samples are labeled as CF/PPS 1, CF/PPS 2, and CF/PPS 3; and one sample of CF/PPS is tested by the single 4695 TR test; this sample is labeled as CF/PPS 4.

Three samples of GF/PEEK (TECATEC PEEK GF50 S296 CP/IP/OS V01 natural, Ensinger, Germany) are tested by the multi-cell 21700 TR test; these samples are labeled as GF/PEEK 1, GF/PEEK 2, and GF/PEEK 3; and one sample of GF/PEEK is tested by the single 4695 TR test; this sample is labeled as GF/PEEK 4.

Three samples of GF/PPS (TECATEC PPS GF50 P203 CP/IP/OS V01 natural, Ensinger, Germany) are tested by the multi-cell 21700 TR test; these samples are labeled as GF/PPS 1, GF/PPS 2, and GF/PPS 3; and one sample of GF/PPS is tested by the single 4695 TR test; this sample is labeled as GF/PPS 4.

At Table 3.1, the technical data regarding physical parameters, thermal properties, and mechanical properties for the different composite materials tested is indicated.

Property	CF/PC	CF/PEEK	CF/PPS	GF/PEEK	GF/PPS
Fiber Type	3K Carbon	Carbon HT 3K	Carbon HT 3K	E glass	E glass
Weaving Style	Twill 2/2	Atlas 5HS	Twill 2/2	US 7781	Style 7628
Area Weight (dry fabric)	200 g/m^2	280 g/m^2	200 g/m^2	296 g/m^2	203 g/m^2
Weight Rate (0°/90°)	50/50 %	-	-	-	-
Fiber Volume Content	45 %	50 %	50 %	50 %	50 %
Matrix Weight Content	-	41.9 %	42.7 %	33.9 %	34.9 %
Product Area Weight	-	482 g/m^2	349 g/m^2	455 g/m^2	312 g/m^2
Material Width	-	1000, 1270 mm	1000, 1270 mm	1000, 1270 mm	1000, 1270 mm
Thickness per Layer	0.25 mm	0.31 mm	0.22 mm	0.24 mm	0.16 mm
Density	1470 kg/m^3	1520 kg/m^3	1520 kg/m^3	1900 kg/m^3	1900 kg/m^3
Glass Transition Temperature	100 °C	143 °C	90 °C	143 °C	90 °C
Melting Temperature	-	343 °C	285 °C	343 °C	285 °C
Short-term Use Temperature	-	300 °C	260 °C	300 °C	260 °C
Long-term Use Temperature	-	260 °C	230 °C	260 °C	230 °C
Thermal Expansion Coefficient (0°/90°)	-	$5 \cdot 10^{-6}$ K^{-1}	$5 \cdot 10^{-6}$ K^{-1}	$10 \cdot 10^{-6}$ K^{-1}	$10 \cdot 10^{-5}$ K^{-1}
Burning Behavior at 1.5 mm	V-0	-	-	-	-
Burning Behavior at 3.0 mm	V-0	-	-	-	-
Burning Behavior at 0.4 mm	V-0	-	-	-	-
Burning Behavior at 0.75 mm	V-0	-	-	-	-
Tensile Strength	550 MPa	713 MPa	680 MPa	450 MPa	375 MPa
Tensile Modulus	48 GPa	59 GPa	55 GPa	24 GPa	23 GPa
Elongation at Break	1.1 %	-	-	-	-
Flexural Strength	775 MPa	866 MPa	780 MPa	445 MPa	500 MPa
Flexural Modulus	43 GPa	645 MPa	57 GPa	22 GPa	21 GPa
Compressive Strength	-	645 MPa	650 MPa	-	400 MPa
Compressive Modulus	-	-	51 GPa	-	26 GPa
Interplanar Shear Strength	-	137 MPa	131 MPa	105 MPa	88 MPa
Interlaminar Shear Strength	-	65 MPa	-	41 MPa	-

Table 3.1 : Technical data of CF/PC [66], CF/PEEK [5], CF/PPS [6], GF/PEEK [4] and GF/PPS [7]

3.1.2 LIB cells

For the material screening process, 2 different types of LIB were tested. For the multi-cell TR test, 7 cells of the type INR21700-50S (21700, Samsung, Korea) were used, while for the single-cell TR test, the cells employed were INR4695 (INR4695-300A, Svolt, China).

To charge the different batteries, the following chargers are used:

- **INR21700-50S charger** (XTAR VC8 Charger, ShenZhen XTAR Electronics Co, China)

- **INR4695 charger** (Ultramat 16S, Graupner, Germany)

Technical data

In Table 3.2, technical data of the INR21700-50S and INR4695 is presented. It can be observed that the maximum operating temperature of both of the cells for safety use is 60 ºC and 70ºC, respectively. This indicates that INR4695 will have to be heated to a higher temperature than INR21700 to induce TR.

Property	INR21700-50S	INR4695
Cell Weight	72 g max.	430 g, 435 g max.
Cell Height	70.62 mm max.	95 $\pm$ 0.3 mm
Cell Diameter	21.25 mm max.	46 $\pm$ 0.2 mm
Volume	0.02 cm^3	0.16 cm^3
Capacity	5 Ah	30 Ah
Nominal Voltage	3.6 V	3.6 V
Energy	18 Wh	108 Wh
Volumetric energy density	742.41 Wh/cm^3	684.06 Wh/cm^3
Standard Charging Time	150 min / 250 mA cut-off	-
Energy Density	-	270 Wh/kg
Operating Charging Temperature (ambient)	0 to 60 ºC	0 to 45 ºC
Operating Discharging Temperature (ambient)	-20 to 60 ºC	-30 to 60 ºC
Operating Charging Temperature (surface)	0 to 60 ºC	-
Operating Discharging Temperature (surface)	-20 to 80 ºC	-
Operating Temperature (for Safety Certificate)	*10 to 60 ºC	-
Operating Temperature (Overheat Protection)	-	70 ºC

Table 3.2   : Technical data of INR21700-50S [11] and INR4695 [3]

The volume and the energy are calculated with the given data. The volumetric energy density is calculated following the equation previously explained at subsubsection 2.1.2. Regarding volume, 6.51 21700 cells correspond to one 4695 cell, while in terms of energy, six 21700 cells correspond to one 4695 cell. In terms of volumetric energy density 21700 cells present a higher one, having a 7.86 % greater volumetric energy density.

Transportation and storage of the LIBs

For safety requirements, the cells were stored and transported to the experimental area by a box for LIB protection (GENIUS Transportbehälter aus Kunststoff, GENIUS Technologie GmbH, Germany) with UN3480 approval. In the following Figure 3.1 a, the box employed for transportation is observed. The batteries were also secured inside the box so they would not tip over or collide with other batteries around them.

Once the TR experiments were run, the battery safety box RETRON 460 (Battery safety box RETRON 460, RETRON GmbH, Germany) was employed to store them; it can be observed at Figure 3.1 b. It is a hot-dip galvanized steel container that is UN-approved and has a special insulation function. The usable volume of the box is 344 liters [78].

Figure 3.1 : a) UN3480 storage box, b) RETRON 460 battery safety box

3.1.3 Battery enclosure

Two battery enclosures made out of steel were employed. For the multi-cell test, the dimensions were 120 x 120 mm (Figure 3.2 a), while for the single-cell test, the box dimensions were 200 x 200 mm (Figure 3.2 d). Both of them present a cable port to get the cables of the heating foils and the thermocouples out from the enclosure, an orifice for the pressure sensor, and an orifice designed to relieve the heat during TR and prevent high pressures during it. In both of the enclosures, a battery holder (Figure 3.2 b) was employed to prevent the cells from entering contact or falling over.

Another difference between both of the enclosures is the lid system; while in the multi-cell test, a single lid is employed (Figure 3.2 c), in the single-cell test, two lids are employed. For the first case, the sample is over the box. In the second case, a lid is over

the box. This lid presents a space to support the sample, with the same size as the ones used in the multi-cell test, and over this sample, the final lid is placed (Figure 3.2 e). It's important to notice that both lids present fillet edges in the face that faces the sample so as not to damage the sample and to distribute the pressure equally throughout the sample.
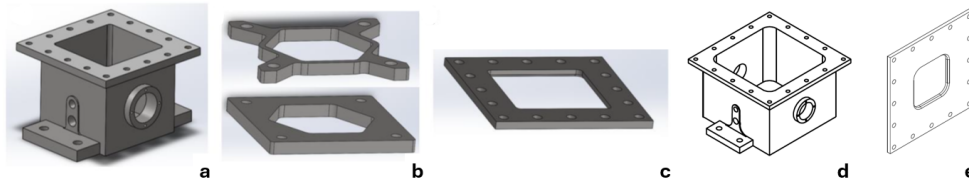
Figure 3.2 : a) Multi-cell test battery enclosure, b) Battery holder, c) Multi-cell test battery lid [99], d) Single-cell test battery enclosure e) Single-cell test battery lid

3.1.4 Electronic components

To accomplish the UL 2596 norm, see subsection 2.4.1, the following electronic components were employed.

- **Arduino Mega 2560** (Arduino Mega 2560 Rev 3, Arduino, USA): Microcontroller board based on the ATmega2560. It is used to control the heating rate supply by measuring the cell temperature. All the electronic components related to the control process are connected to it; a more detailed explanation is found in subsection 3.2.2.

- **QuantumX MX840B** (QuantumX MX840B Universal amplifier, Hottinger Brüel & Kjaer Germany): Data acquisition system that read the measurements of the thermocouples and the pressure sensor.

- **Dual-MOSFET-Treiber** (2,0 A Dual-MOSFET-Treiber, Microchip, USA): For switching and amplifying the signals from the Arduino to the heating foils.

- **K type thermocouple** (G/G-30-KK-IEC, Thermofühler GmbH, Germany): This temperature sensor sensor generates a small voltage proportional to temperature.

- **MAX6675 K-type thermocouple temperature sensor module for arduino** (MAX 6675, Maxim Integrated, USA): Reads the voltage from the K-type thermocouple, compensates for cold junctions, and converts it into a digital signal that the Arduino can interpret.

- **Heating foil of 48 W** (Polyimide heating foil, TRUE COMPONENTS, UK): Used to heat the initiator cell.

- **Power supply** (BYGD Adapter 12 V 10, BYGD, China): Transfers the amount of current necessary to heat the heating foil.

- **RS PRO Pressure Sensors 797-5046** (RS PRO Pressure Sensors 797-5046, RS, UK): With a measurement capacity of 0 to 6 bar and an output of 0-5 V, this sensor is connected to the battery enclosure, measuring the pressure inside it during the experiment and sealing it.

3.1.5 Thermal camera

The thermal camera employed to record the experiments is the infrared camera Optris PI 640i, Optris, Germany. This camera has an optical resolution of 640x480 pixels; the PI 640i delivers pin-sharp radiometric pictures and videos in real time. The camera measures 45x56x90 mm, and its working temperature range goes from -20 °C to 900 °C [73]. It can be observed at Figure 3.3 a.

To protect the thermal camera if, during the experiments, a sample breaks during the process or a flame reaches the camera, housing was designed for the camera, taking into account its measurements and its connection and protection needs with non-reflective germanium glass for the transmission of the wavelength in the camera range. The concept of this design can be seen in Figure 3.3 c and d. However, for greater protection, it was finally decided to opt for the outdoor protective housing from the same manufacturer due to the high cost of the thermal camera, represented at Figure 3.3 b.
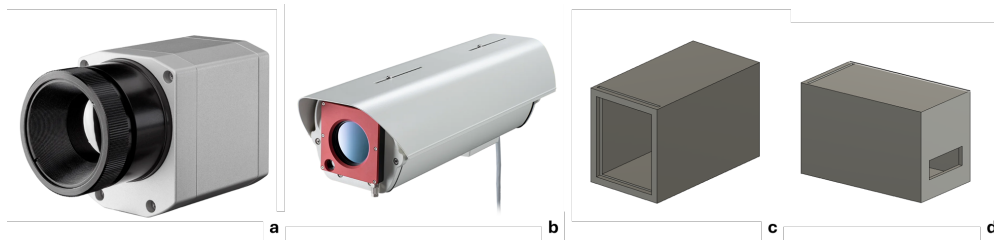
Figure 3.3   : a) Optris PI 640i [73], b) Outdoor protective housing [74], c) Frontal view of the housing concept d) Back view of the housing concept

3.1.6 Recording camera

The Nikon Z30, Nikon Corporation, Japan, is used to record the course of the experiments from the start of the cell heating process until minutes after the TR has occurred. To adjust this to the height of the experiment bench, a tripod is used, as can be seen in Figure 3.4.

Figure 3.4 : Nikon Z30 camera with tripod focusing on test bench

3.1.7 Software

In this section, all the software employed for the test execution is listed:

- **Optris PIX Connect**: Documentation and analysis of thermal images.

- **Arduino**: Programming of the Arduino Mega 2560 microcontroller, more information at subsubsection 3.2.3.

- **Visual Studio Code**: For developing a code in Python for storing the Arduino values, more information at subsubsection 3.2.3.

- **CatmanEasy-AP**: To acquire, view and save the measurement data from the thermocouples and pressure sensors.

3.2 Method

3.2.1 Preparation of the materials

Previously to the test campaign, the materials employed for it should be prepared beforehand. This section explains the preparation method of them.

To compare the mass loss of the samples tested, they are previously weighted as seen in Figure 3.5. The thickness of the four corners and the middle is also measured. The

measurements of these two characteristics are found in Table 3.3; it also includes the average thickness and the standard deviation of it.

Figure 3.5   : Sample weight measurement before TR

Sample	Weight [g]	Thk. 1 [mm]	Thk. 2 [mm]	Thk. 3 [mm]	Thickness 4 [mm]	Thk. 5 [mm]	Average Thickness [mm]	Standard deviation [mm]
CF/PC 1	51.60064	2.042	2.044	2.039	2.035	2.044	2.0408	0.003429286
CF/PEEK 1	63.03729	2.431	2.45	2.443	2.427	2.438	2.4378	0.008231646
CF/PEEK 2	63.92094	2.471	2.47	2.457	2.469	2.481	2.4696	0.007631514
CF/PEEK 3	63.30532	2.459	2.445	2.426	2.447	2.449	2.4452	0.010740577
CF/PEEK 4	63.30404	2.428	2.439	2.447	2.451	2.43	2.439	0.009055385
GF/PEEK 1	75.10527	2.166	2.251	2.327	2.301	2.345	2.278	0.064330397
GF/PEEK 2	74.92198	2.212	2.273	2.293	2.179	2.275	2.2464	0.043412441
GF/PEEK 3	75.29804	2.317	2.273	2.319	2.301	2.292	2.3004	0.016989408
GF/PPS 1	68.65721	2.006	2.091	2.086	2.055	2.059	2.0594	0.030256239
GF/PPS 2	68.79807	2.064	2.092	2.066	2.07	2.063	2.071	0.01077033
GF/PPS 3	68.61525	2.059	2.057	2.06	2.059	2.077	2.0624	0.007364781
CF/PPS 1	50.94981	1.968	1.98	1.956	1.959	1.984	1.9694	0.01109234
CF/PPS 2	50.98498	1.928	1.931	1.958	1.901	1.94	1.9316	0.018532134
CF/PPS 3	50.78617	1.932	1.89	1.942	1.945	1.922	1.9262	0.019823219
CF/PPS 4	50.68373	1.932	1.931	1.935	1.896	1.937	1.9262	0.015249918

Table 3.3   : Sample thickness and weight before TR

After this procedure is finished, the UL 2596 norm is followed, and the samples are preconditioned more than 48 hours prior to testing in a room at 23 ±2 °C with 50 ±10 % relative humidity [8].

Heating foils and thermocouples are also prepared in the lab. Thermocouples' longitude is selected depending on where they will be connected they are assembled as shown in Figure 3.6,
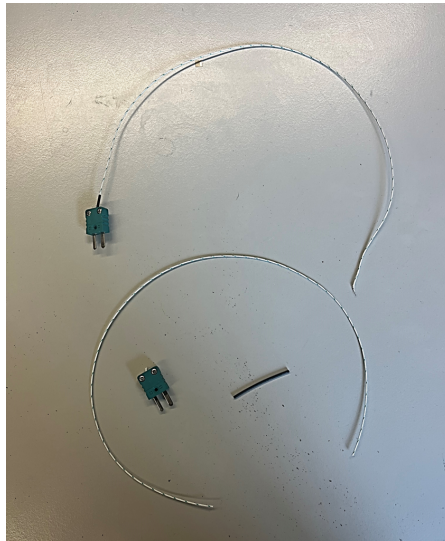
Figure 3.6 : Sample weight measurement before TR

Thermal insulation is cut to create an insulator between the steel box and the batteries when placing them on it. 12 squares are cut in 100 x 100 mm sizes for the multi-cell tests, and 4 are cut in 180 x 180 mm for the single-cell tests.

LIB cells are charged beforehand in the lab before transporting them to the test area.

3.2.2 Materials assembly and experiment flow

In the first place, cells should be prepared for the TR. In the case of the 21700, the first step is to peel the protector plastic. To do this, cells are placed in a holder to be fixed and do not collide with each other, see Figure 3.7 b; they are peeled one by one, leaving some plastic so the positive terminal is not in touch with the negative one, see Figure 3.7 a. The purpose of peeling the cells is to allow TR to propagate more easily as the worst-case scenario is being measured.

The cell in the middle, the initiator cell of the TR, is wrapped around two heating foils which apply a total of 96W, see Figure 3.7 c. The Arduino and Quantum X thermocouples are also glued and fixed again with Kapton tape to measure the temperature during the experiment. The temperature of the two surrounding cells and the ambient temperature were also registered with thermocouples.

Finally, the cells are placed in the steel holder (wrapped with Kapton tape to avoid a short circuit by not making contact with the cells), and they are also wrapped with Kapton tape to increase the contact between them for greater TR propagation. The final assembly of the 21700 cells for the test can be seen in see Figure 3.7 d.

In the case of the single-cell experiment, the process is similar to that of the multi-cell experiment. In this case, the 4695 cell is wrapped by 3 heating foils that will transmit 120 W to it, see Figure 3.7 e. Again, the thermocouples for the Arduino and the quantum X are placed on the cell, and also the environment thermocouples are placed in the enclosure. In Figure 3.7 f, the holder can also be seen; the insulator material at the bottom of the box is visible in this picture, though it is placed in all the experiments. A steel plate is placed under the insulator, in the 4695 case, to raise the cell to maintain the same distance from the top of the cell to the sample as in the single-cell experiment.

Finally, it is important to notice a main difference between Figure 3.7 d and f, not only in the number of cells but the placement of, in the case of the 21700 cells, the venting cup placed at the top of the cell (positive terminal) while in the case of the 4695, the venting cup is located on the button (negative terminal), this is the reason why 4695 cell is upside down.
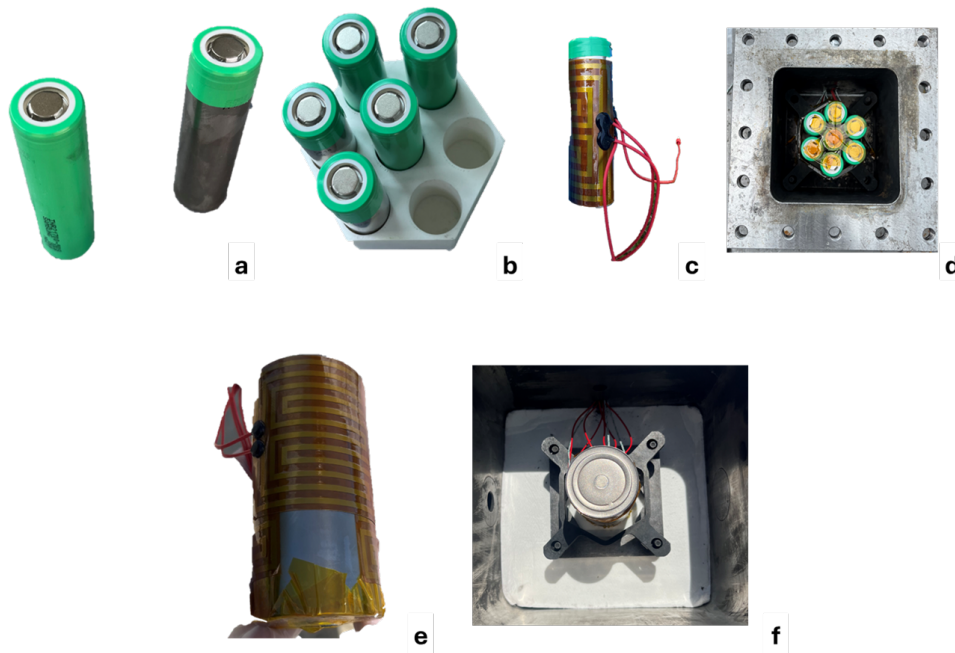
Figure 3.7   : a) 21700 peeling process, b) 21700 external holder, c)21700 initiator cell heating foils wrapping, d) Final assembly 21700 cells, e) 4695 cell heating foils wrapping, f) Final assembly 4695 cell

The next step is the placement of the sample. In Figure 3.8, the process can easily be followed:

a) The first step is to place the bottom lid for the case of the single-cell test.

b) The sample is placed over this bottom lid; in the case of the multi-cell, it is placed directly over the enclosure.

c) The top lid is placed, and masking tape is placed around the corners if the reflection is high.

d) The thermocouples, the emissivity tape for the thermal camera, and the screws are placed.

e) The screws are The screws are screwed following the star pattern torquing to distribute the stresses evenly.

f) Placement of the pressure sensor.
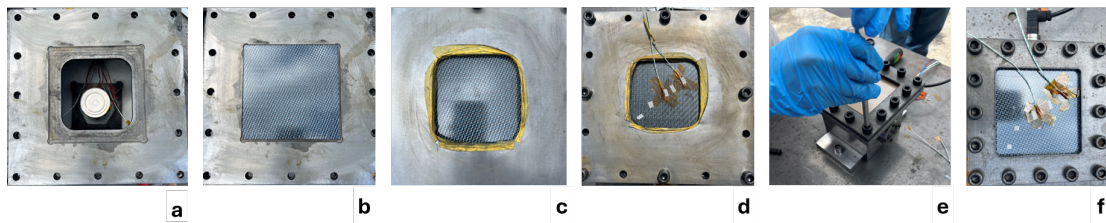
Figure 3.8 : a) 4695 enclosure bottom lid placement, b) 4695 enclosure sample placement, c)4695 enclosure top lid placement, d) 4695 enclosure screws, thermocouples, and emissivity tape placement, e) 21700 enclosure screwing process, f) 21700 final assembly with pressure sensor

The thermal camera is placed in the outdoor protective housing, and the focus is checked via the Optris PIX Connect software. The recording camera is placed in front of the test bench. All the thermocouples, except the one for the Arduino and the pressure sensor, are connected to the Quantum X; the CatmanEasy-AP software is employed to check that all the sensors are working properly. The initiator thermocouple, as well as the heating foils, are connected to the Arduino Mega 2560. The final assembly can be observed in Figure 3.9.

Figure 3.9   : Test bench final assembly

Once everything is connected, the test can begin. Firstly, with the initiation of the recording of the data of the QuantumX through the CatmanEasy-AP, the thermal camera data through Optris PIX Connect, and the images from the recording camera. The Arduino code is sent, and the data from the monitor is stored through the VS Code Python script. The implementation of the Arduino code heats the heating foils and, hence, the initiator cell until this one reaches any of the boundary conditions that are further explained in subsubsection 3.2.3 that represents the start of the TR condition. The thermal camera recording stops once the onset of thermal runaway happens, and the data recorded with the CatmanEasy-AP is collected for at least 5 min after it, as the UL 2596 indicates.

After conducting the experiments, the samples are weighted and then cleaned to remove any residue. They are weighted again to calculate the mass loss.

3.2.3 Code and boundary conditions

This section summarizes the process of developing the code for heating the LIB and the boundary conditions of heat that can be transferred to it.

Boundary conditions

The experimental data employed to calculate the boundary conditions of heat that can be transferred to the LIB are based on Özsoy experiments [99] with seven 21700-type cells. Data is extrapolated to the 4695 cells also studied in this project.

The three boundary conditions studied are:

- Temperature of the initiator cell at which TR started: Max. T.

- Heating rate of the initiator cell at which TR started: Max. HR.

- Heating rate ratio of the initiator cell at which TR started: Max. HRr.

For this purpose, three experiments were analyzed. On the first one Figure 3.10, The temperature at which Thermal Runaway started is 136.52ºC, which corresponds to the temperature located just before the abrupt slope change, the TR. The heating rate at which TR started corresponds to the 70.65 slope. The heating rate ratio corresponds to the ratio between the 70.65 ºC/s slope and the 0.365 ºC/s previous slope, in this case, 195.20.
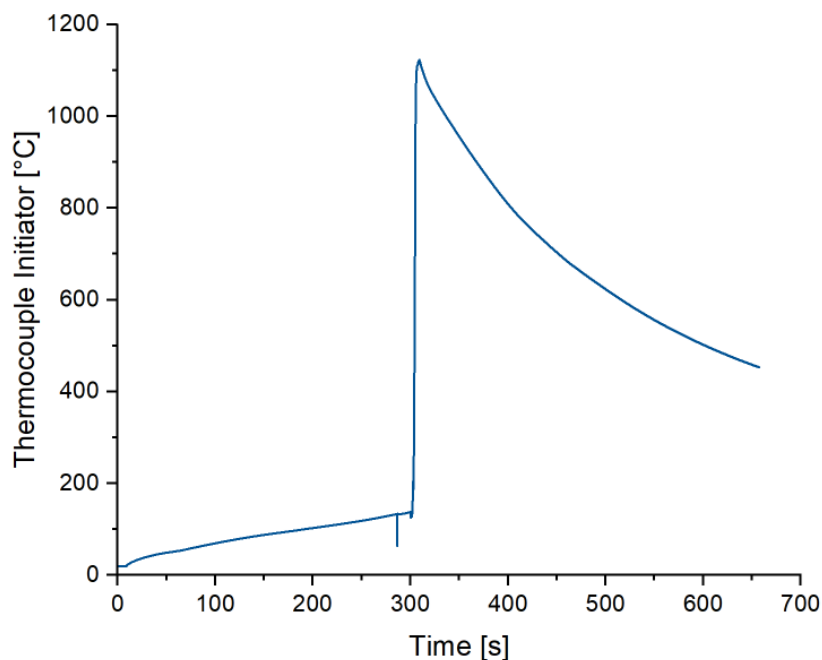
Figure 3.10   : Experimental data thermal runaway experiment with CF RC380 Toray. Data from [99]

The same calculations are performed with the experimental data shown in Figure 3.11 and Figure 3.12. The Table 3.4 collects all the calculated maximums.
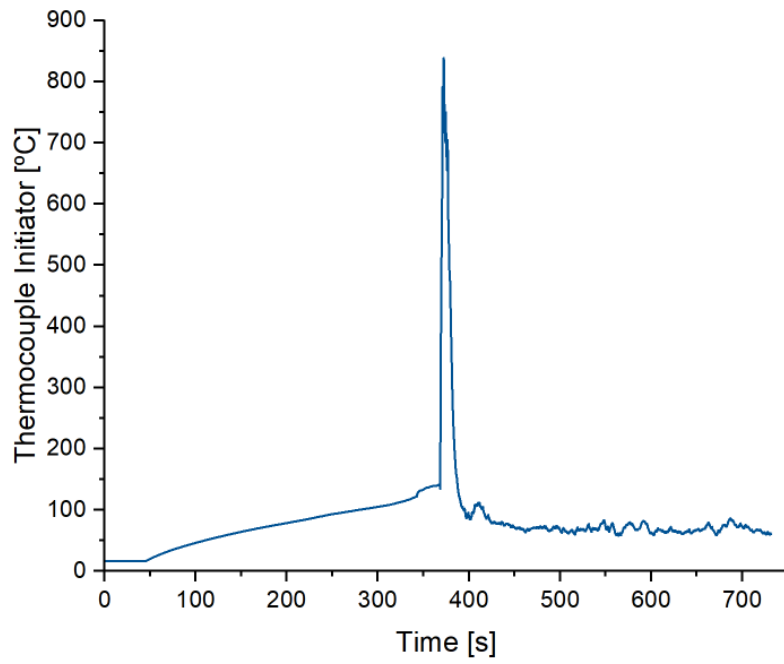
Figure 3.11   : Experimental data thermal runaway experiment with CF GF PA6.
Data from [99]
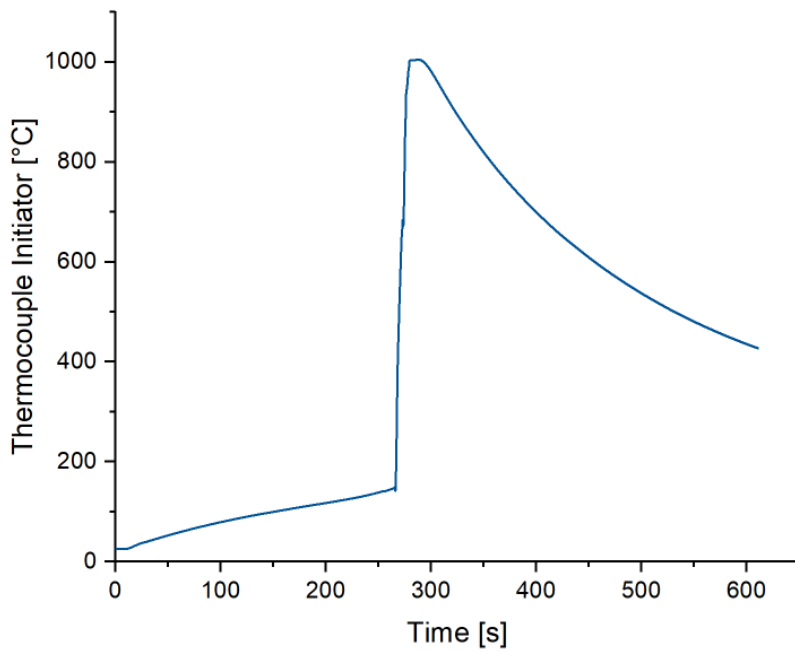
Figure 3.12   : Experimental data thermal runaway experiment with CF BioResin.
Data from [99]

Experiment	Max. T [ºC]	On set. T [ºC]	On set. HR [ºC/sec]	On set. HRr
CF RC380 Toray	1123.10	134.24	70.65	195.20
CF GF PA6	838.31	147.25	39.30	119.91
BioResin Isovolta	1004.7	146.26	37.69	84.91
Selected	-	160	100	100

Table 3.4   : On set T, HR and HRr selection

Based on the data of Table 3.4, the average maximum temperature, and the average maximum Heating Rate are selected as the boundary conditions for the 21700 cell experiments. All these boundary conditions are inserted in the Arduino code as boundary conditions for heating the heating foils that heat the cell. For the case of the 4695 experiments, the same boundary conditions were applied for the calibration test, and based on the results, they were adjusted, raising the on set T to 200 ºC, the on set. HT to 200 ºC/s and the On set. HRr to 200ºC.

Code

In this subsection, the Arduino code developed for the purpose of the experiments is explained. This version of the code was based on a preliminary version of it from [99].

```
1  //Pin configurations defined
2  const int thermoSO = 4;
3  const int thermoCS = 5;
4  const int thermoSCK = 6;
5  const int MosfetPIN = 13;          // the Arduino pin, which
      connects to the IN pin of relay
6
7  MAX6675 thermocouple(thermoSCK, thermoCS, thermoSO);
```

The first lines of code consist of configuring the different pins connected to the Arduino, including the thermocouple, the heating foils, and the MOSFET to control when heat should be or should not transferred through the heating foils.

```
1  //First values defined
2  float maxTemp = 160;
3  float maxHeatingRate = 100;
4  float maxRatioHeatingRate = 100;
5  float POWER = 100;                 // INPUT: desired power
6  float Power = 255*POWER/100;
7  unsigned long previousMillis = 0;
8  float currentTemp = 0;
```

```
9  float previousTemp = thermocouple.readCelsius();
10 float heatingRate = 1;
11 float previousHeatingRate = 1;
12 float ratioHeatingRate = 5;
13 float second = 0;
14 int timeStep =0;
```

The variables needed for the implementation of the code are defined. The maximum T, HR, and HRr calculated in subsubsection 3.2.3 is declared, and the power will be provided to the heating foils. Preliminary values of the current temperature, heating rate, and heating rate ratio of the cell and the seconds and time step of each measured are declared suitable values for programming purposes.

```
1 //Conversion of inf and nan to 1.00
2 float safeCalculation(float x) {
3   if (isnan(x) || isinf(x)) {
4     return 1.0;
5   }
6   return abs(x);
7 }
```

The function *safeCalculation* is declared to be employed later in the code to avoid bugs due to possible punctual malfunctions of the thermocouples and division by zeros when the temperature does not increase from one measurement point to the other, where the HRr would become a NaN due to a division by zero.

```
1 void setup() {
2   Serial.begin(9600);
3   pinMode(MosfetPIN, OUTPUT);
4   analogWrite(MosfetPIN, Power);
5 }
```

In the *void setup()*, the initial configuration of the Arduino and the MOSFET enables the current to be transmitted to the heating foils.

```
1 void loop() {
2   unsigned long currentMillis = millis();
3   timeStep =currentMillis - previousMillis;
4   if(timeStep >=1000){
5       currentTemp = thermocouple.readCelsius();
6       second = second + 1;
7       heatingRate = (currentTemp - previousTemp) / (
           timeStep / 1000.0);
```

```
8        ratioHeatingRate = abs(safeCalculation(heatingRate /
             previousHeatingRate));
9        Serial.print("t; ");
10       Serial.print(second);
11       Serial.print(" ; T;");
12       Serial.print(currentTemp);
13       Serial.print(" ; pHR;");
14       Serial.print(previousHeatingRate);
15       Serial.print(" ; HR;");
16       Serial.print(heatingRate);
```

In the *void loop*, the milliseconds that have elapsed since the first *void set up* was started are counted so that when a time step of 1 second is reached, the following operations found within the if are performed. In the first place, the current temperature of the cell is read with the function *thermocouple.readCelsius()*, from this information, the heating rate and the heating rate ratio are calculated, and the function *safeCalculation* is employed in this calculation. These measured and calculated data are displayed on the monitor plot within the seconds they were measured.

```
1        if(currentTemp > maxTemp){
2          analogWrite(MosfetPIN, 0);
3          Serial.print("   ; THE MAXIMUM TEMPERATURE WAS
             REACHED");
4        }
5        if(heatingRate > maxHeatingRate){
6          analogWrite(MosfetPIN, 0);
7          Serial.print("   ; THE MAXIMUM HEATING RATE WAS
             REACHED");
8        }
9        if(ratioHeatingRate > maxRatioHeatingRate &&
             previousHeatingRate!=1){
10         analogWrite(MosfetPIN, 0);
11         Serial.print("   ; THE MAXIMUM HEATING RATE RATIO
             WAS REACHED");
12       }
13       previousHeatingRate = heatingRate;
14       previousMillis = currentMillis;
15       Serial.println();
16     }
17 }
```

Finally, these data are compared with the boundary conditions defined previously. In case the current temperature of the cell is higher than the maximum temperature established, the MOSFET is disconnected, so the heating foils stop receiving current, and, therefore, they stop transferring heat to the cell. A message informing about this situation appears on the Arduino monitor, and from this moment on, the message is disconnected, but the information regarding T, HR, and HRr is displayed every second on the monitor. Analogously, the same process occurs when the maximum Heating Rate or the maximum Heating Rate ratio is exceeded.

Additionally to the Arduino code, a Pyhon Code was developed to store the data in an *Excel* file.

```python
import os
import csv
import serial
import time
from datetime import datetime

current_datetime = datetime.now()
filename = current_datetime.strftime("%Y-%m-%d_%H-%M-%S")
    + ".csv"

folder_path = r"D:\"

file_path = os.path.join(folder_path, filename)

with open(file_path, "w", newline='') as f:
    writer = csv.writer(f, delimiter=",")
    serialCom = serial.Serial('COM5', 9600)
    serialCom.setDTR(False)
    time.sleep(1)
    serialCom.flushInput()
    serialCom.setDTR(True)
    kmax = 180 * 90
    for k in range(kmax):
        try:
            s_bytes = serialCom.readline()
            decoded_bytes = s_bytes.decode("utf-8").strip
    ()
            print(decoded_bytes)
            writer.writerow([decoded_bytes])
```

```
28        except ValueError as ve:
29            print(f"Value error: {ve}, line was not
    recorded.")
30        except Exception as e:
31            print(f"Unexpected error: {e}, line was not
    recorded.")
32 serialCom.close()
```

3.2.4 Preliminary test

To validate the correct functionality of the Arduino code for the purpose it was created, the following preliminary experiments and some modifications and repetitions of them for warranty were performed. The absence of damage and the proper functionality of the electronic equipment were validated as well, and if any electronic component was damaged, it was replaced with a new one.

Preliminary test with light bulb

The first test was done by replacing the heating foils with a light bulb. This test aimed to check that a simpler code version worked correctly and that the MOSFET was not damaged.

The simpler version of the code consisted of a void loop with an if statement that sent a signal to the MOSFET to allow the current to light the bulb on during a certain time, and afterward, that turns off the current so the light bulb remained off for a certain time, it continued with this cycle behavior until the Arduino was disconnected.

This preliminary experiment concluded that the code worked, but the MOSFET was damaged, and as a consequence, it was replaced with a new one.

Preliminary test of the thermocouple

A preliminary test with an advanced version of the code and the heating foils was performed to check if the thermocouple was damaged. The measurements made by the thermocouple were far from reality, so they were replaced with new ones. The more advanced version of the code was validated.

The Python code for storing the data from the Arduino was validated.

Preliminary test with aluminum cylinder

The purpose of the last preliminary test was to check the validity of the final code (subsubsection 3.2.3) and ensure the safety of the final test. This preliminary test was based on the [99] heating rate test.

To implement the heating test, the heating foil was placed wrapping around an aluminum cylinder of a similar heat capacity ($C_{p,Al}$ = 0.90 J/g K) to a similar LIB cell, the 21700-type battery, whose heat capacity is 0.888 J/(g K) [60]. The thermocouple is also placed in the aluminum cylinder to predict the possible range of values that the cell will reach during the experiment, as well as the heating rate and the heating rate ratio before the thermal runaway. In Figure 3.13, the materials employed can be observed, for the preliminary test, the cell is placed in a holder for safety reasons.

Figure 3.13 : Preliminary test with aluminum cylinder materials

The use of two heating foils is preferred to the use of 1 heating foil as it will ensure that the cell arrives at the on-set temperature; it also ensures a linear behavior in the heating process.

On the Arduino code, the maximum power is set by 255 W for the MOSFET. The effect of the power efficiency is studied by setting it to 50, 60, 75 and 100 %. At 50 and 60 %, the temperature curve presented an exponential behavior, while at 75 and 100%, the temperature curve presented a linear behavior. In [62], it is demonstrated that a higher heating power and higher SOC can lead to a quick trigger for thermal runaway. In contrast, a low heating power can prolong the time interval between safety venting and thermal runaway, resulting in a milder thermal runaway and lower maximum temperature of failed cells. To test the safety of the sample in the worst-case scenario of TR, it decided to prioritize the linearity of the HR over maintaining the standard heating rate (4-7 ºC/min) of the UL 25696 [8].

It is decided to select the 100% power efficiency over the 75% power efficiency as, in both cases, the heating stopped at the maximum heating rate, and in the case of the 100%, the temperature of the cell at that point was greater than in the 75% case.

Thermal camera angle test

Two of the main issues of the thermal camera recording was the temperature distortion caused by the camera's inclination angle.

Due to the lack of consensus in the literature on the maximum inclination angle for avoiding temperature distortions, a thermal camera angle test was performed at the lab. Thermocouples and emissivity tapes over them were placed on a sample at the corners and in the middle, as seen in Figure 3.14. The results of this preliminary experiment show that the best solution was to place some emissivity tapes over the sample to obtain the accurate temperature, as the temperature on those points did not vary regarding the angle.
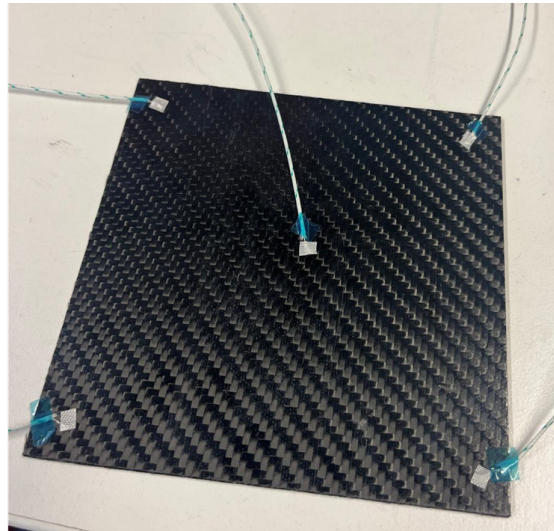
Figure 3.14   : Thermal camera angle test

4 Results and Discussion

This section presents and discusses the results obtained in the experiments carried out in this project.

The results are organized according to the matrix type employed in the sample for a clear presentation.

This section will present, among others, the results obtained with the thermal camera. A generic introduction to the nomenclature and colors used for each temperature is presented below. Each picture of the thermal camera follows the same color bar for a better comparison between them. The Figure 4.1 shows this color bar being the minimum temperature 25.9 ºC and the maximum 349.6ºC. It also represents the different point distribution of the measuring point data being:

- M: Middle, it coincides with the measurement of the thermocouples "Laminate Middle"

- CRT: Corner Right Top.

- CRB: Corner Right Bottom, it coincides with the measurement of the thermocouples "Laminate Corner".

- CLT: Corner Left Top.

- CMLT; Corner Middle Left Top, the intermediate point between CLT and M.

- Area 1: Measures the maximum temperature of the whole sample.
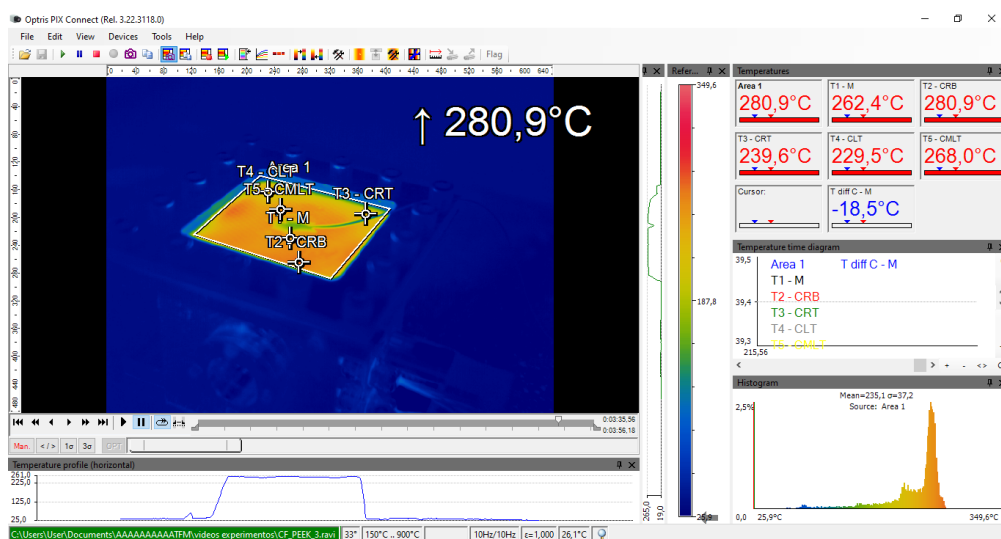
Figure 4.1   : Thermal bar and point data distribution at CF PEEK 3

In the case of the thermocouple measurement graphs, some of the thermocouples failed during certain tests; for this type of case, the measurements were directly suppressed from the graphs. All the Quantum X graphs, thermocouples, and pressure sensors are found in chapter 6; only CF/PEEK and CF/PC samples Quantum X samples are deeply explained in this section as the rest of the tests with the same cell arrangement followed a similar qualitative behavior.

For both thermal camera graphs and Quantum X graphs (thermocouple temperature and pressure), some offsets were applied, these offsets can be consulted at Table 6.1. For the Quantum X graphs, the instant 0 corresponds to the TR, while for the thermal camera graphs, the instant 0 corresponds to the beginning of the steeper slope of heating of the sample.

For a better understanding and comparison of the TR evolution between experiments, the initial temperature distribution, the temperature distribution 5 seconds before TR, the temperature distribution at TR, the temperature distribution 5 seconds after TR, and the maximum temperature distribution at the sample after TR are displayed.

In the case of the Nikon camera pictures, the same instants as the ones of the thermal camera are represented, except for the maximum temperature distribution, which will be changed to the final instant.

4.1 Multi-cell 21700 TR results

This section presents the results from the 21700 TR. Firstly, the PEEK resins results are presented, followed by the PPS matrix. Finally, a summary of the results of this investigation is presented.

4.1.1 PEEK

The first matrix, PEEK, was tested under TR with carbon and glass fibers. Three experiment repetitions were performed for each type of fiber with three different samples.

CF/PEEK

CF/PEEK 1 results

For the CF/PEEK 1 temperature recording, only the information on the thermocouples was stored due to a malfunction of the thermal camera.

The Figure 4.2 shows the measurements of the thermocouples during the TR experiment. The thermocouple of the initiator cell connected to the Quantum X did not work;

its data was replaced by the thermocouple attached to the Arduino. The heating rate of the initiator cell is 36.42 ℃/min. The moment the TR starts, all the measures inside the enclosure present a peak with a similar shape. The TR of the surrounding cells caused by the TR of the initiator presents a similar shape to the first one but with a slight delay in time and a lower temperature. Due to the TR process, the enclosure environment also heats up, but not as much as the cell measurements.

In the case of the temperature measurement of the laminate, the middle temperature presents a steeper slope than the one at the corner. In contrast, the middle temperature decreased more rapidly than the one at the corner. The laminate presents its higher temperature during the process, 338.89 ℃, in the middle region. The thermocouple measurements are shown as an example on the first set of samples, the CF/PEEK, the rest of them are found at the chapter 6.

The Figure 4.3 presents the differential pressure distribution in the enclosure. A peak is observed at the instant of the initiator cell's TR, followed by other pressure peaks. It is believed that the pressure peaks that follow the initial one correspond to the TR of the surrounding cells. The last pressure peak is the higher pressure it achieves in the enclosure, reaching 1.25 bar; after this, a minimum pressure appears.
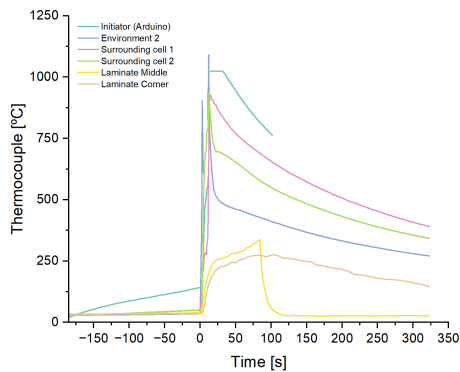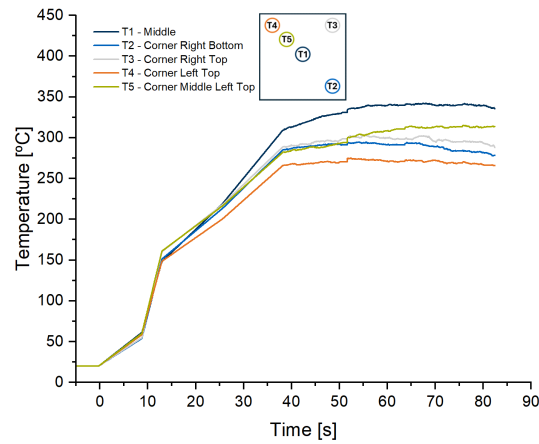

Figure 4.2 : CF/PEEK 1 thermocouple measurements during TR test
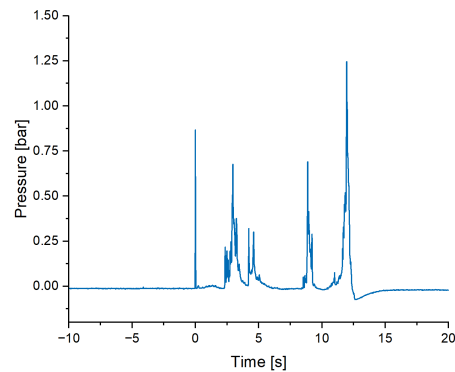
Figure 4.3 : CF/PEEK 1 pressure measurement during TR test

Figure 4.4 shows the sample evolution through the whole process. Traces of matrix degradation can be observed from the initial picture before the TR to the pictures after. On the front part, the color of the sample has changed after the TR, see Figure 4.4 b, while after the cleaning process, open plies are present at the sample, especially on the middle and on one of the corners can be observed at Figure 4.4 d.
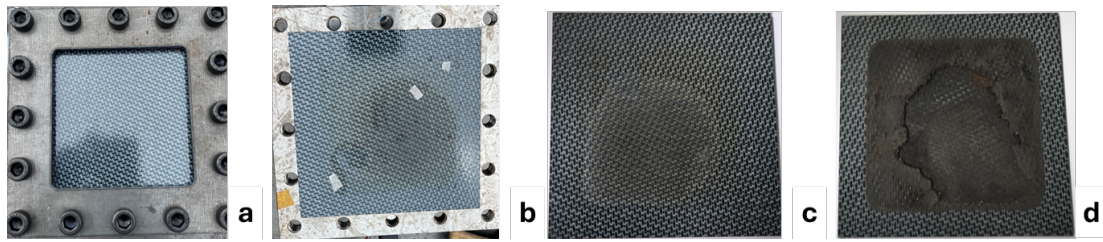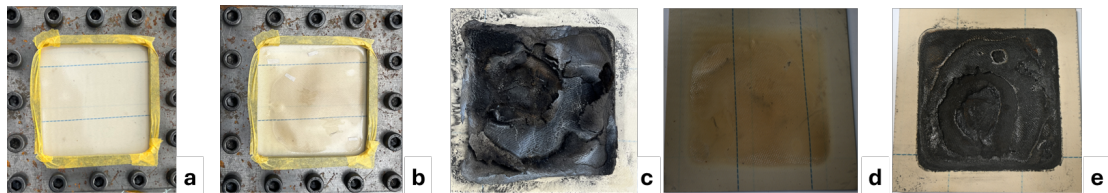
Figure 4.4　: CF/PEEK 1 a) before TR (front), b) after TR (front), c) after TR and cleaning (front), d) after TR and cleaning (back)

CF/PEEK 2 results

In Figure 4.5, it can be observed that the initiator cell and the environment temperatures both show a similar shape and a slope at the same time as the TR occurs. The heating rate of the initiator cell before TR was 40.23 ºC/min. Initially, the environment temperature values were similar to those of the initiator cell, but shortly after the TR, the environment temperature dropped. The surrounding cell heats up later; this difference is more noticeable than in CF/PEEK 1, and the shape of the temperature curve is slightly different from the initiator and environment measurements.

Figure 4.6 presents the differential pressure distribution in the enclosure. It can be observed as a peak at the TR instant followed by other pressure peaks, which are suggested to correspond to the TR of the surrounding cell. In this case, the one at the TR of the initiator cell presents a higher one of 1.13 bar.

The Figure 4.7 presents the temperature evolution at different sample parts. It can be observed that the maximum temperatures are concentrated in the middle of the sample as the T1 and T5 present the highest values.
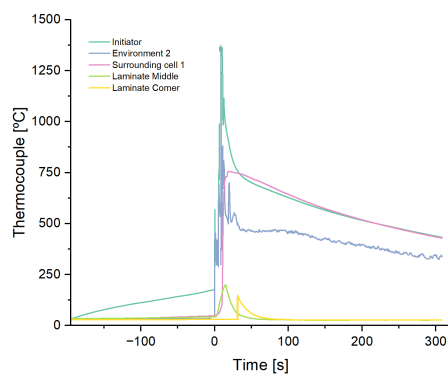
Figure 4.5　: CF/PEEK 2 thermocouple measurements during TR test
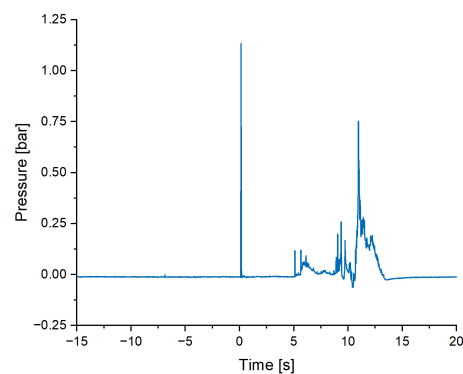
Figure 4.6　: CF/PEEK 2 pressure measurement during TR test
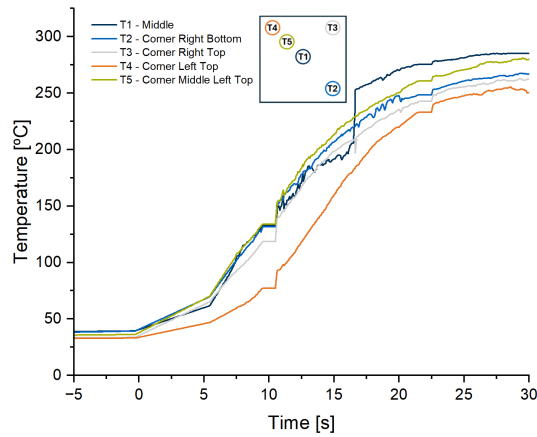
Figure 4.7 : CF/PEEK 2 thermal camera measurements during TR test

Figure 4.8 shows the sample evolution through the whole process. It presents a similar evolution as CF/PEEK 1 with a change of color on the front part after the TR, see Figure 4.8 b, and open plies, especially in the middle and on one of the corners, see Figure 4.8 e. From Figure 4.8 c to e, the importance of cleaning the residues after the TR process can be appreciated.
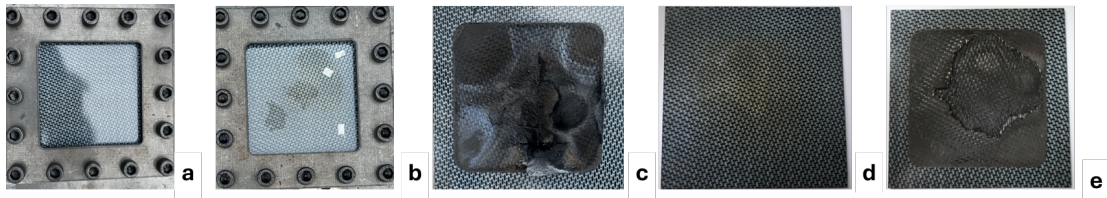
Figure 4.8 : CF/PEEK 2 a) before TR (front), b) after TR (front), c) after TR (back), d) after TR and cleaning (front), e) after TR and cleaning (back)

CF/PEEK 3 results

In Figure 4.9, the behavior of the environment and the surrounding cells is similar to the ones observed in the previous cases; the environment slope is more pronounced and slightly before the surrounding cells; after the TR, the temperature of the environment is lower than the ones of the surrounding cells. The maximum temperature of the environment was 1000 ℃. In this case there was no valid data for the initiator thermocouple.

Figure 4.10 presents the differential pressure distribution in the enclosure. As in the previous cases, there is a peak at the initiator cell TR instant followed by other pressure peaks, which are believed to correspond to the TR of the surrounding cells. In this case, the second peak presents the highest value, 0.94 bar.

The Figure 4.11 presents the temperature evolution at different sample parts. It can be observed that the maximum temperatures are concentrated in the middle of the sam-

ple, such as the T1 at the beginning of the experiment, while 20 seconds after TR, the temperature at the corner right bottom is much higher than the rest.
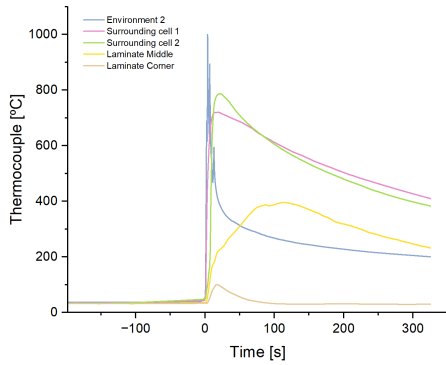
Figure 4.9 : CF/PEEK 3 thermocouple measurements during TR test
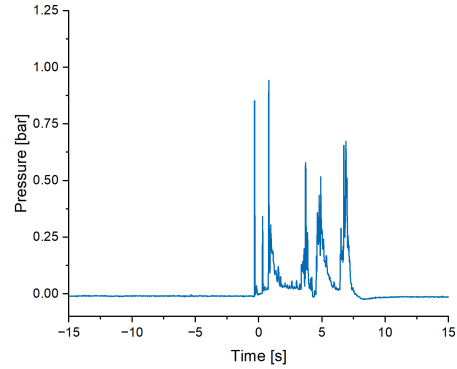
Figure 4.10 : CF/PEEK 3 pressure measurement during TR test
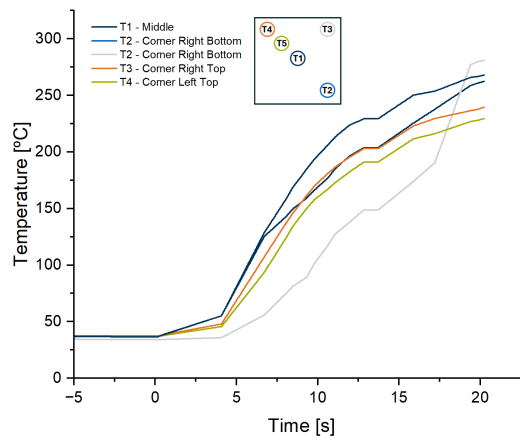
Figure 4.11 : CF/PEEK 3 thermal camera measurements during TR test

Figure 4.12 shows the sample evolution through the whole process. It presents a similar evolution as CF/PEEK 1 and 3 with a change of color on the front part after the TR, see Figure 4.8 b. Open plies are also noticeable in the middle of the sample. However, this time, it is also noticeable on one of the sides and not that much in the corners, see Figure 4.12 e. Again, from Figure 4.12 c to e, the importance of cleaning the residues after the TR process can be appreciated.
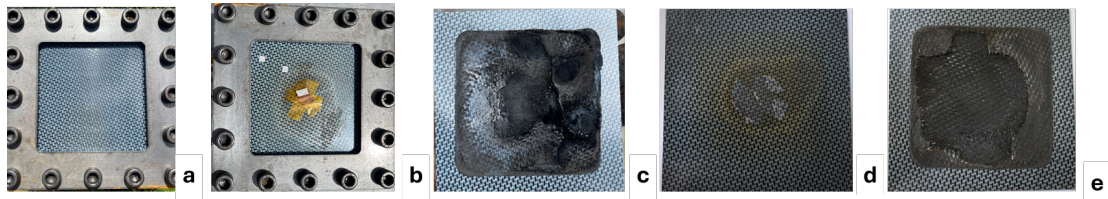
Figure 4.12 : CF/PEEK 3 a) before TR (front), b) after TR (front), c) after TR (back), d) after TR and cleaning (front), e) after TR and cleaning (back)

Summary and discussion

In Figure 4.13, the evolution of the CF/PEEK sample and the enclosures from the outside through the TR process is observed. It can be seen that only the two thermocouples from the sample stayed on it for the whole process for the CF/PEEK 1 case.

CF/PEEK 1   **CF/PEEK 2**   **CF/PEEK 3**

Beginning of the experiment

5 seconds before flame

First flame

5 seconds after flame

End of the experiment

Figure 4.13   : CF/PEEK 1, 2 and 3 sample and flame evolution from outside the enclosure during TR

At Figure 4.15, the thermal images of the CF/PEEK 2 and 3 samples are presented during the TR processes. It can be observed that 5 seconds after the first flame, the

flame of the second sample was greater than the third one, and the temperatures of the sample were higher as well.
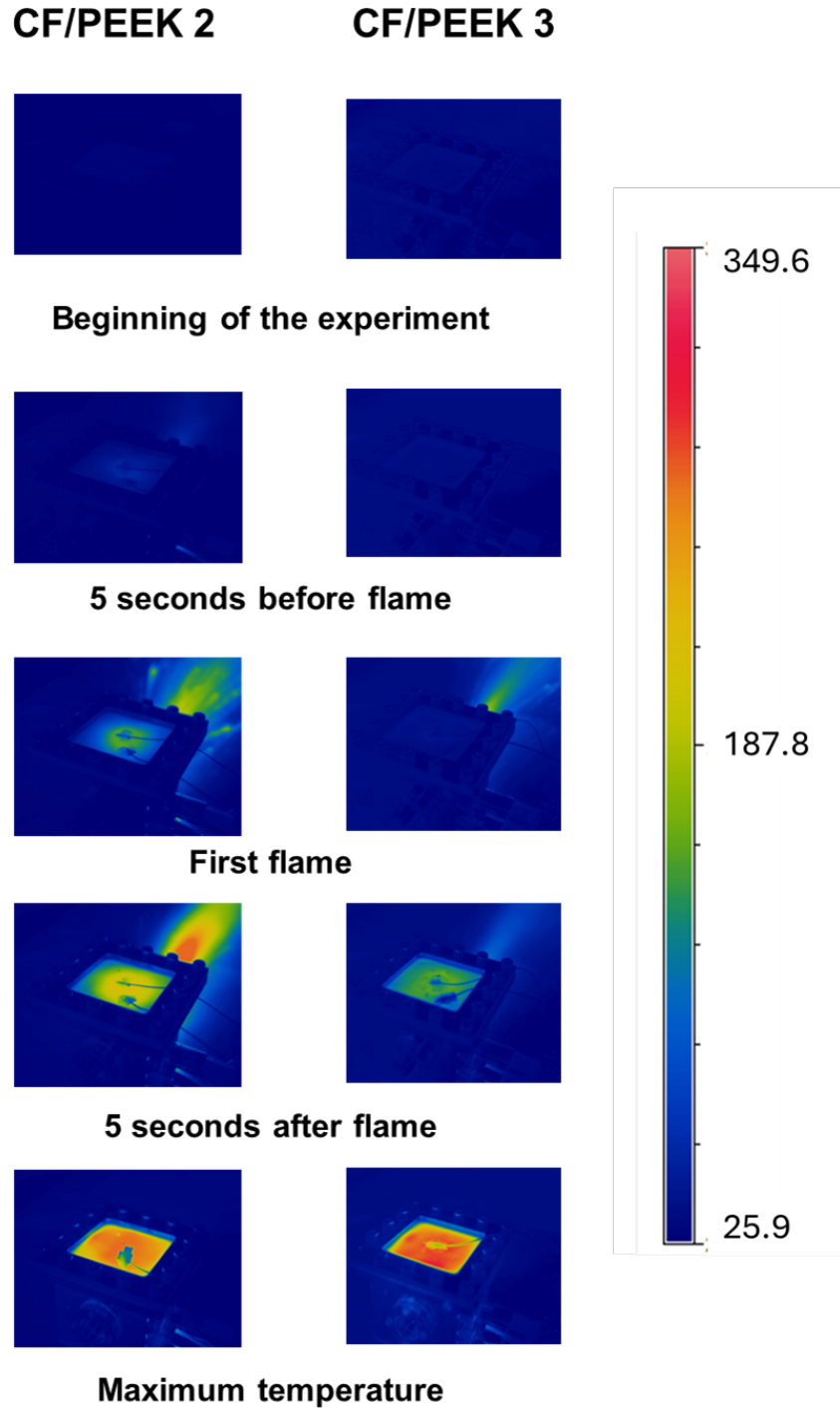
Figure 4.14   : CF/PEEK 2 and 3 sample thermal evolution evolution during TR

Figure 4.15 shows a comparison of the maximum temperature at each point of the sample for the three repetitions, as well as the maximum differential pressure at which they

were exposed. While CF/PEEK 2 and 3 present similar values of maximum temperatures in all the points studied, sample 3 presents a lower maximum differential pressure compared to sample 2. Both the values of maximum temperatures and maximum differential pressures of sample 1 are higher than in samples 2 and 3.
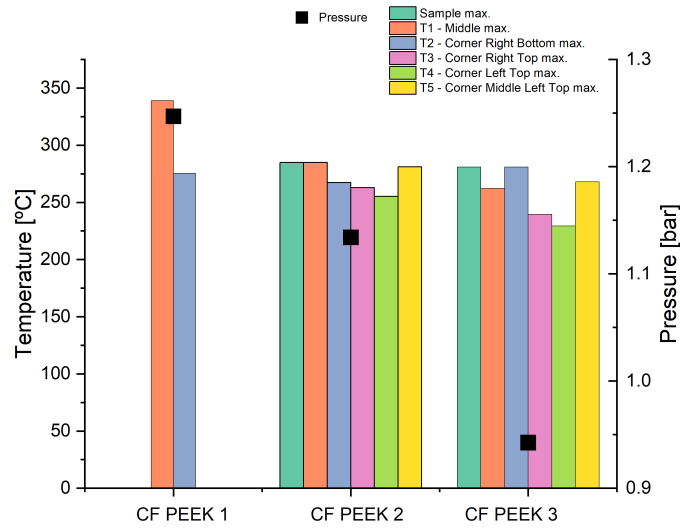
Figure 4.15   : CF/PEEK 1, 2 and 3 sample temperatures and pressure summary

In Figure 4.16 and Figure 4.17, the mass loss of the CF/PEEK samples is presented in grams and percentages, respectively. It is observed that samples 1 and 2 exhibit similar values, 3.23% and 3.32%, respectively. In contrast, sample 3 displays a higher mass loss, 3.80%, even though the testing conditions were similar to those of the second repetition, and the maximum difference in pressure was not as significant compared to the earlier samples.
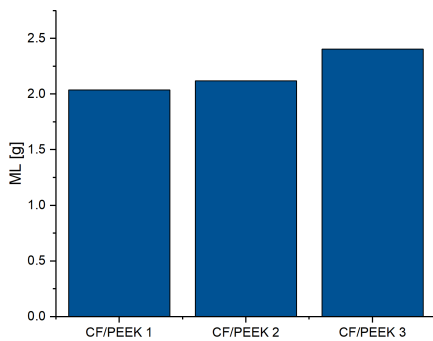
Figure 4.16   : CF/PEEK 1, 2 and 3 ML [g] after TR
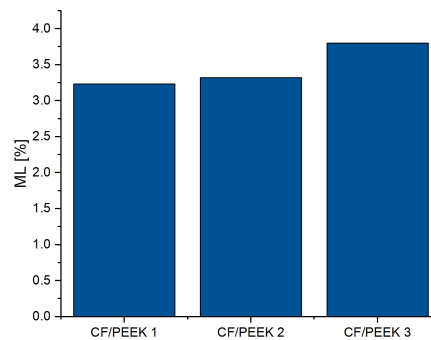
Figure 4.17   : CF/PEEK 1, 2 and 3 ML [%] after TR

GF/PEEK

GF/PEEK 1 results

The Figure 4.18 presents the temperature evolution at different sample parts. It can be observed that the maximum temperatures are concentrated in the middle of the sample as the T1 presents the greatest temperatures, and T5 presents a similar shape as the middle one but with lower values. The points of study located at the corners present a similar slope as the middle one, but they start cooling down earlier.
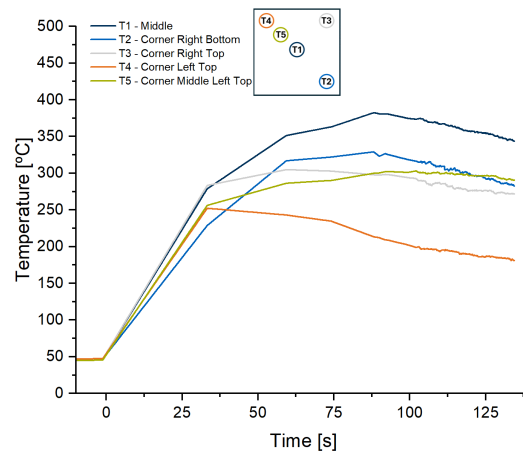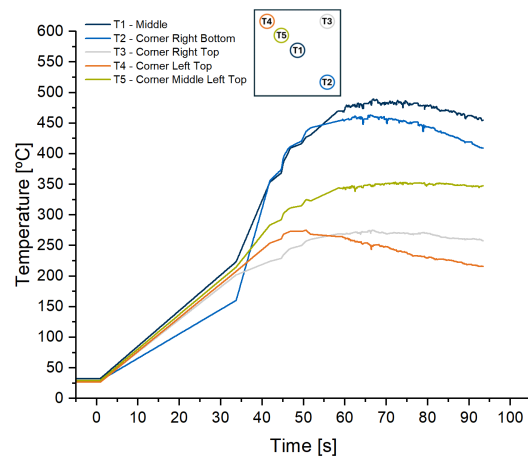

Figure 4.18 : GF/PEEK 1 thermal camera measurements during TR test

Figure 4.19 shows the sample evolution through the whole process. A change of color between before TR Figure 4.19 a, and after TR Figure 4.19 b and c is visible. In Figure 4.19 c, it can be seen that the sample presents swelling. Figure 4.19 d presents traces of open plies, especially in the middle of the sample, but it also expands to the sides, affecting the whole area exposed to the TR.
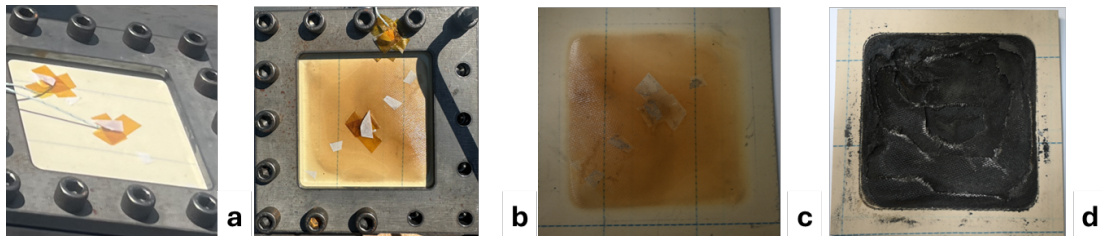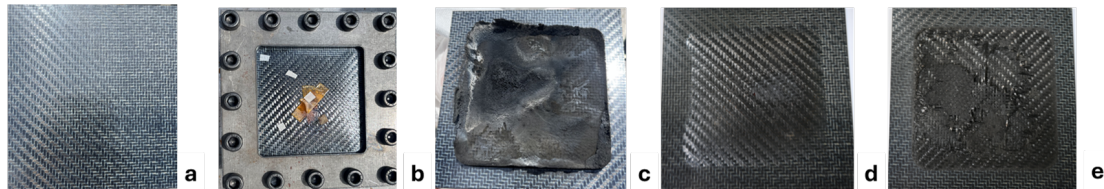

Figure 4.19 : GF/PEEK 1 a) before TR (front), b) after TR (front), C) after TR and cleaning (front) d) after TR and cleaning (back)

GF/PEEK 2 results

The Figure 4.20 presents the temperature evolution at different sample parts. It can be observed that the corner right top presents the maximum temperatures during the TR process, followed by the middle one and the corner left top.
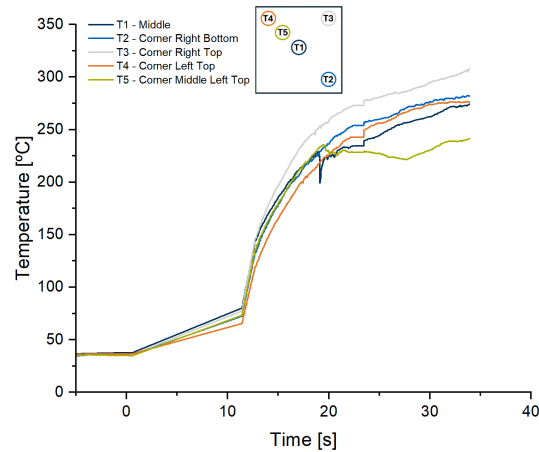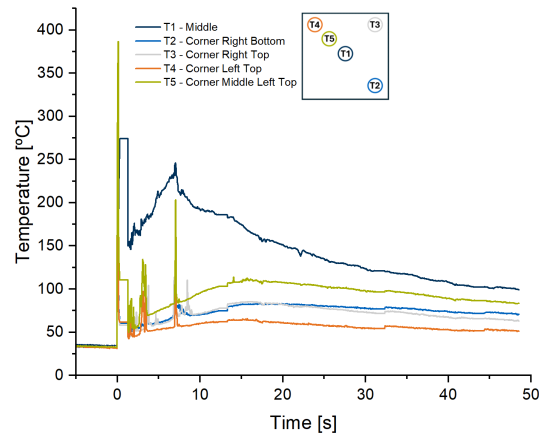

Figure 4.20 : GF/PEEK 2 thermal camera measurements during TR test

Figure 4.21 shows the sample evolution through the whole process. A change of color between before TR Figure 4.21 a, and after TR Figure 4.21 b and c is visible. In b and c, it can be observed that the sample is swollen on one half of it (a triangle swelling); the points that delimit this swelling are the same ones as the ones shown at Figure 4.20 that showed the highest temperatures. Picture Figure 4.19 d presents traces of open plies, especially following the swelling line.
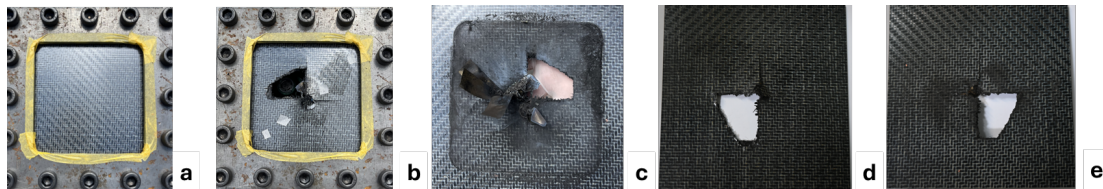

Figure 4.21 : GF/PEEK 2 a) before TR (front), b) after TR (front), c) after TR (back), d) after TR and cleaning (front), e) after TR and cleaning (back)

GF/PEEK 3 results

The Figure 4.22 presents the temperature evolution at different sample parts. It can be observed that the middle point presents the highest temperatures while the rest of the points present similar temperatures except the corner left top, which presents the lowest values.

Figure 4.22 : GF/PEEK 3 thermal camera measure-
ments during TR test

Figure 4.23 shows the sample evolution through the whole process. A change of color between before TR Figure 4.23 a, and after TR Figure 4.23 b and c is visible. In b and c, it can be observed that the sample is swollen, as it was in the two previous samples. Picture Figure 4.19 d presents traces of material degradation as open plies, especially in the middle and one of the corners following a concentric pattern.

Figure 4.23 : GF/PEEK 3 a) before TR (front), b) after TR (front), c) after TR (back), d) after TR and cleaning (front), e) after TR and cleaning (back)

Summary and discussion

In Figure 4.24, the evolution of the GF/PEEK sample and the enclosures from the outside through the TR process is observed. It can be seen that the thermocouples of the sample resisted the whole TR process except sample 3, where one of the thermocouples fell from the sample between the flame and the end of the experiment.

GF/PEEK 1 **GF/PEEK 2** **GF/PEEK 3**

Beginning of the experiment

5 seconds before flame

First flame
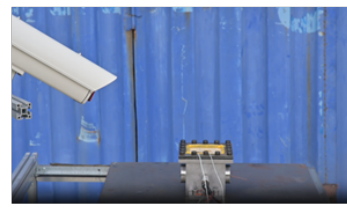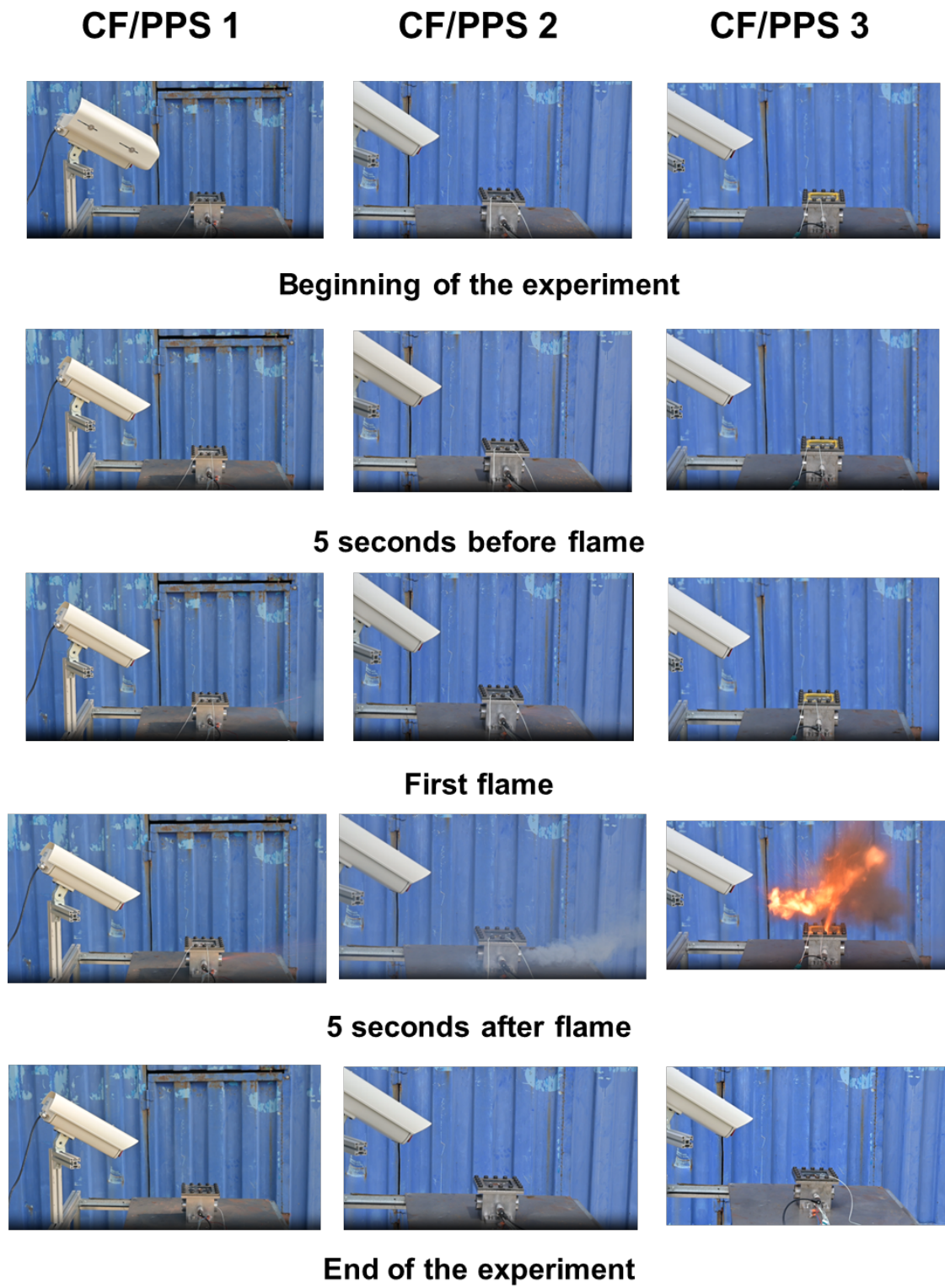
5 seconds after flame

End of the experiment

Figure 4.24   : GF/PEEK 1, 2 and 3 sample and flame evolution from outside the enclosure during TR

At Figure 4.25, the thermal images of the samples GF/PEEK 1, 2, and 3 are presented during the TR processes. It can be observed that GF/PEEK 2, which presents a more noticeable swelling, presents higher temperatures at the point of maximum temperature distribution in the region where the swelling is formed.
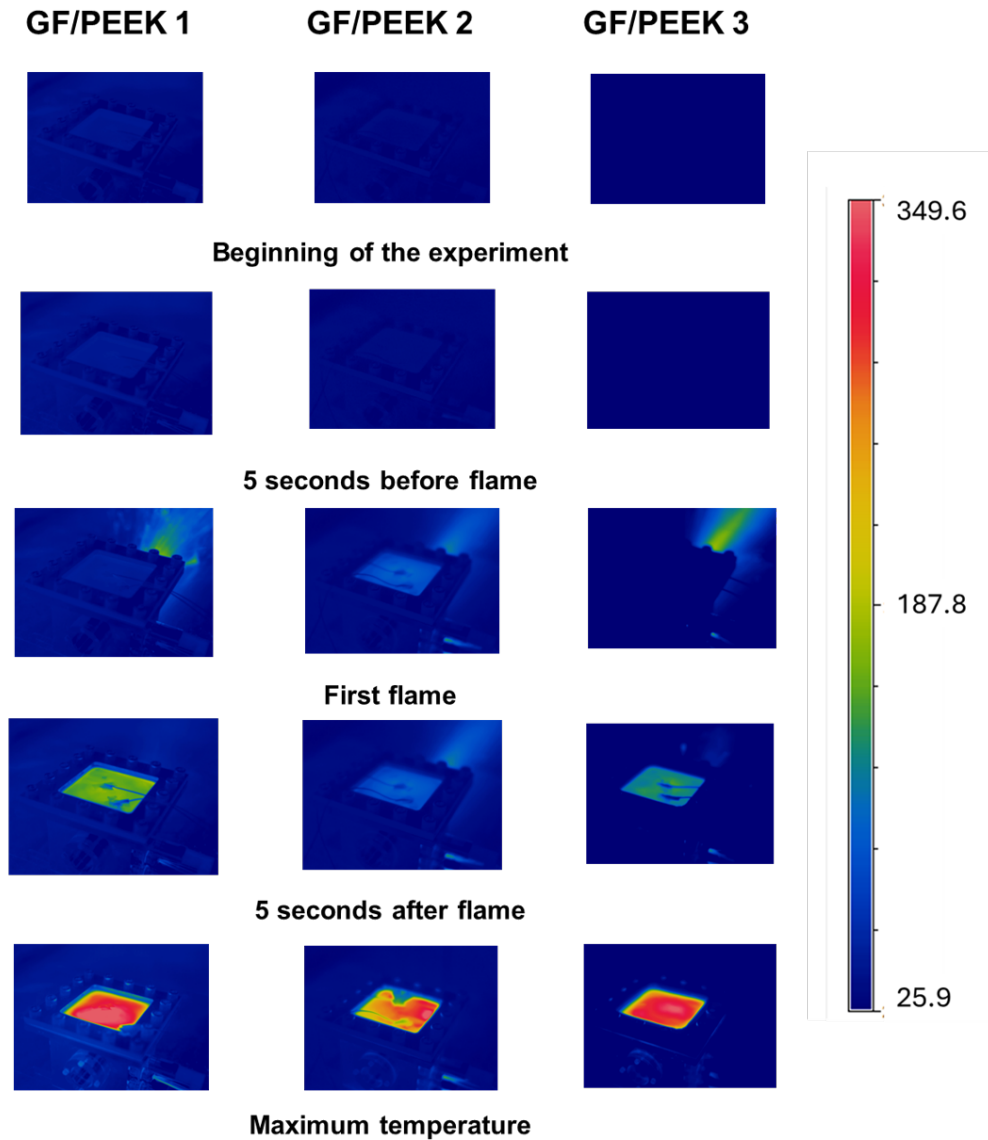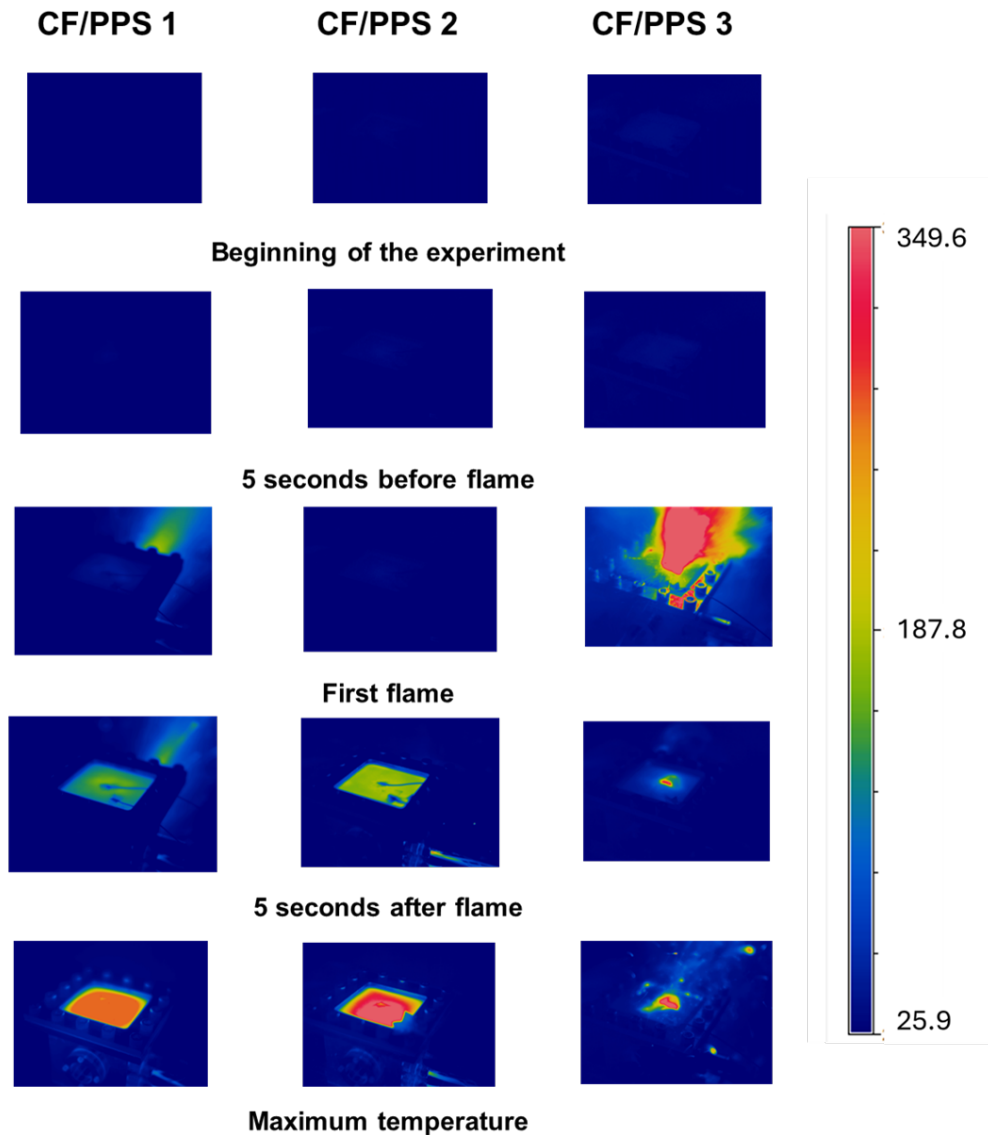

Figure 4.25   : GF/PEEK 1, 2 and 3 sample thermal evolution during TR

Figure 4.25 compares the maximum temperature at each point of the sample for the three repetitions, as well as the maximum differential pressure at which they were exposed. With this graph, it can be noticeable again the difference between the temperature distribution among the different samples as the point at which the samples achieve higher maximum temperatures between them. GF/PEEK 2 and 3 present a more similar value of maximum differential pressure than CF/PEEK 1, which presents a higher value.
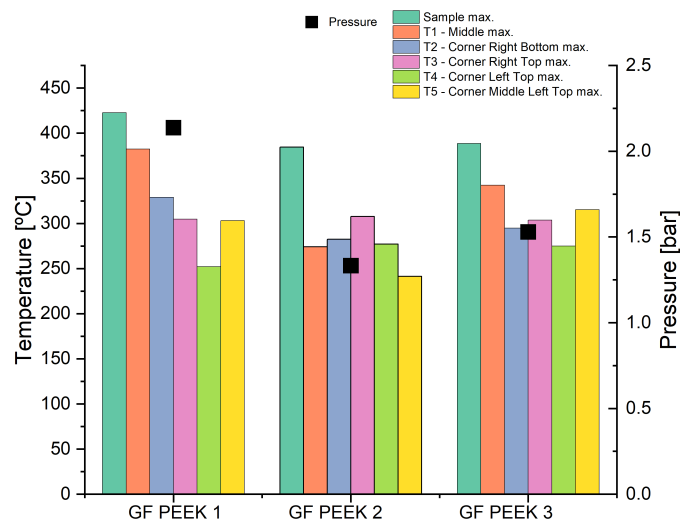
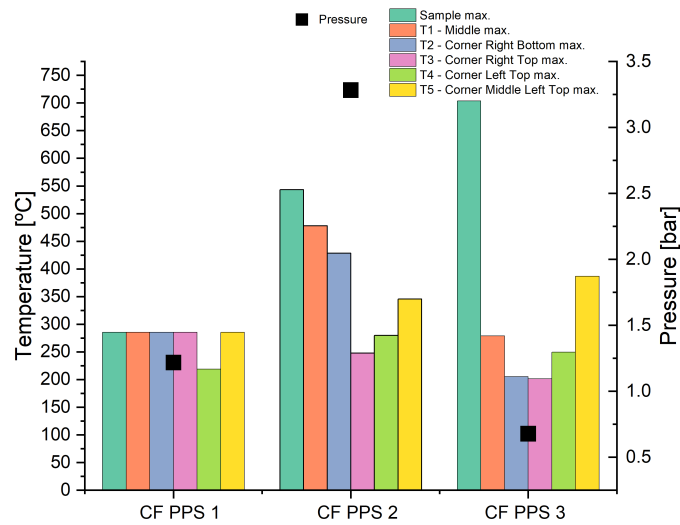Figure 4.26   : GF/PEEK 1, 2 and 3 sample temperatures and
pressure summary

In Figure 4.27 and Figure 4.28, the mass loss of the CF/PEEK samples is presented in grams and percentages, respectively. It is observed that samples 1 and 3 exhibit similar values, 4.93% and 4.91%, respectively. In contrast, sample 2 displays a lower mass loss loss, 4.03%, it is also the sample in which the swelling was more noticeable.
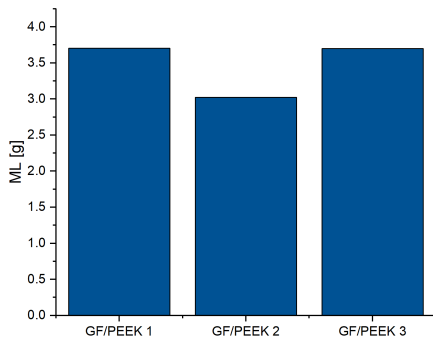
Figure 4.27   : GF/PEEK 1, 2 and 3 ML [g]
after TR
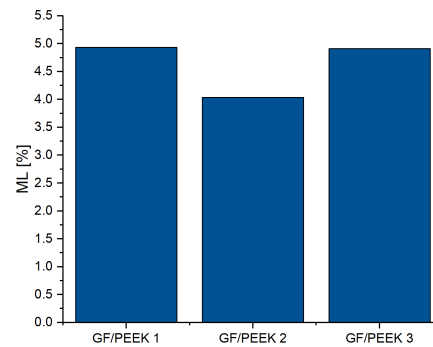
Figure 4.28   : GF/PEEK 1, 2 and 3 ML [%]
after TR

PEEK matrix discussion

This section presents the differences in temperature behavior depending on the type of fiber employed. At Figure 4.29, it can be observed that in the middle, the samples of the same fibers have similar slopes and temperatures. The samples of CF/PEEK present

steeper slopes but reach lower temperatures than the GF/PEEK samples. This behavior on the slope was expected, taking into account that the E glass employed for GF/PEEK presents a thermal conductivity of 1.3 W/(m K) [10], while the carbon HT 3k presented a higher thermal conductivity, 8.5 W/(m K) [50]; which explains a steeper slope in the thermal behavior CF/PEEK. This steeper slope is also observed in the literature [14]. Due to the higher thermal conductivity of CF, the temperatures reached under TR by the composites containing them were supposed to reach higher temperatures, as also indicated in the literature [14]. However, this behavior is not observed, being the GF/PEEK samples the ones that reached higher temperatures. It is suggested that these variations with respect to the expected behavior are due to the variations in the environmental conditions in which the experiments were performed as well as the internal conditions inside the battery enclosure since the conditions of each TR are different, such as the time needed for the TR to begin, the magnitude of the explosion, the type of explosion of the surrounding cells, among others.

Similar slope behavior is generally observed for the cases of the corner right bottom, Figure 4.30 and the corner right top Figure 4.31. The differences at the corners are that while CF/PEEK samples present a more similar behavior between repetitions, GF/PEEK experiments present lower repeatability.
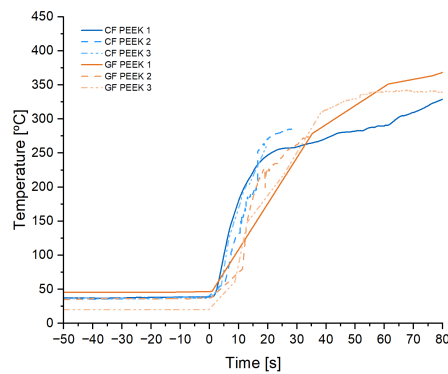
Figure 4.29 : CF/PEEK and GF/PEEK sample middle-temperature summary

74
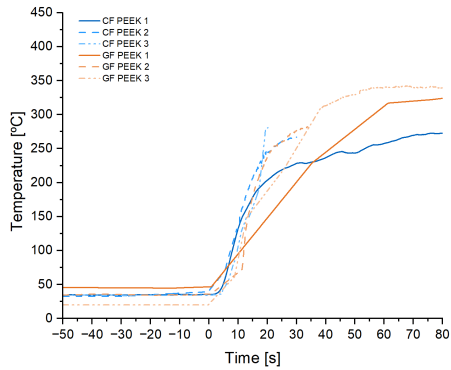
Figure 4.30 : CF/PEEK and GF/PEEK sample corner right bottom temperature summary
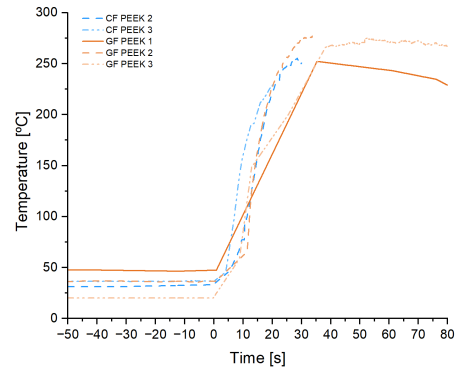
Figure 4.31 : CF/PEEK and GF/PEEK sample corner left top temperature summary

4.1.2 PPS

The second matrix, PPS, was tested under TR with carbon and glass fibers. Three experiment repetitions were performed for each type of fiber with three different samples.

CF/PPS

CF/PPS 1 results

The Figure 4.32 presents the temperature evolution at different sample parts. It can be observed that the temperature is uniform in the whole sample for the first 25 seconds after it starts heating, and from that point on, most of the sample follows the same uniform temperature except the corner left top, which presents a slope of temperature decline. This uniform temperature along the sample can be observed in the thermal camera images, see Figure 4.39
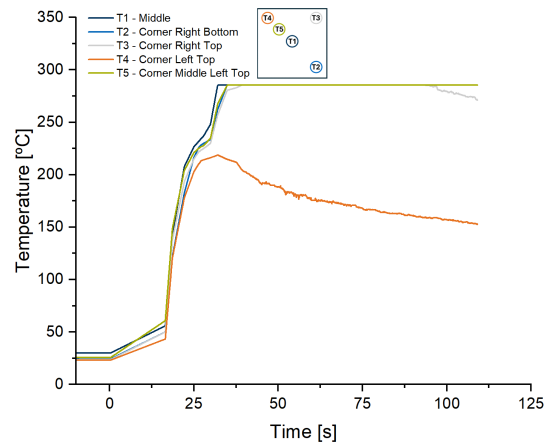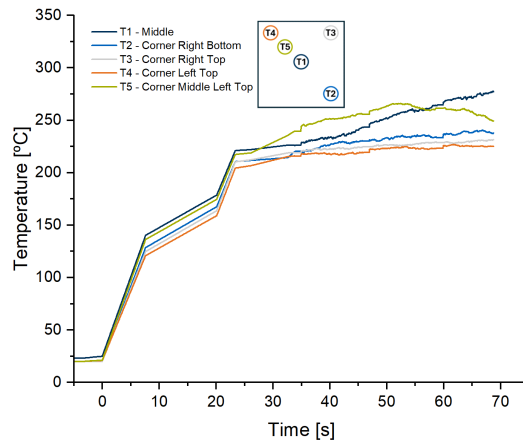
Figure 4.32 : CF/PPS 1 thermal camera measurements during TR test

Figure 4.33 shows the sample evolution through the whole process. A slight change of color between before TR Figure 4.33 a, and after TR Figure 4.33 b and c is visible. Figure 4.19 d presents traces of small open plies on the middle of the sample expanding to the sides.
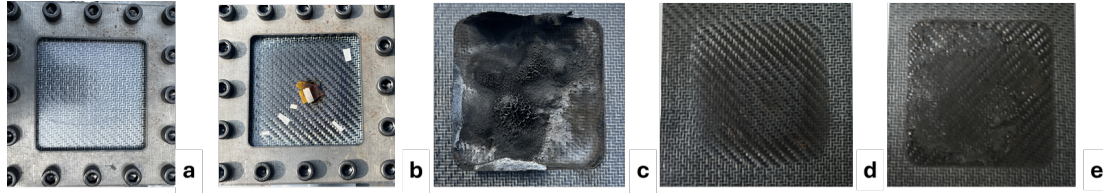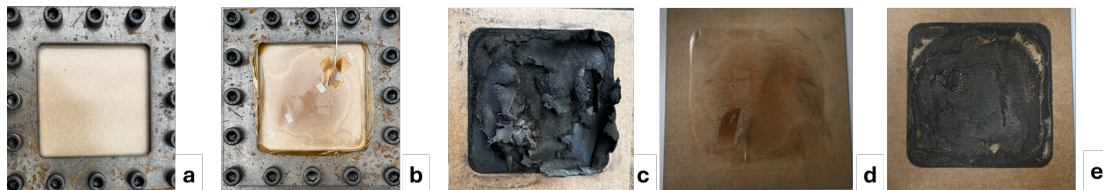

Figure 4.33 : CF/PPS 1 a) before TR (front), b) after TR (front), c) after TR (back), d) after TR and cleaning (front), e) after TR and cleaning (back)

CF/PPS 2 results

The Figure 4.34 presents the temperature evolution at different sample parts. It can be observed that the temperature is higher in the middle and in the corner right bottom than in the rest of the sample. On these two points, the slope and the temperatures reached are similar. The slope is similar for the rest of the points studied, but the temperatures reached diverse levels and were lower than in the middle and at the CRB.

Figure 4.34 : CF/PPS 2 thermal camera measurements during TR test

Figure 4.35 shows the sample evolution through the whole process. The front side after TR, Figure 4.35 d is similar to the one of CF/PPS 1. In contrast, the back side after TR presents much greater open plies than the first sample studied; this material degradation is concentrated in one of the sides, expanding to the middle and its perpendicular sides.

Figure 4.35 : CF/PPS 2 a) before TR (front), b) after TR (front), c) after TR (back), d) after TR and cleaning (front), e) after TR and cleaning (back)

CF/PPS 3 results

The Figure 4.36 presents the temperature evolution at different sample parts. It can be observed that abrupt temperature changes occur at the moment when the initial instant is. This abrupt change is due to a rupture of the matrix. The exact moment this happens can be observed from the outside of the enclosure at Figure 4.39 in the picture CF/PPS 3, 5 seconds after the first flame. The recording points were shifted to avoid recording the flame temperatures.

Figure 4.36   : CF/PPS 3 thermal camera measure-
ments during TR test

Figure 4.37 shows the sample evolution through the whole process. The rupture can be
observed at Figure 4.37 b,c, and e. Sample 3 presents a failure in its function, which
results in a great contrast with sample 1, which gave very good results. Despite present-
ing rupture, Figure 4.37 d does not present a color change, and Figure 4.37 e does not
present material degradation apart from the hole.

Figure 4.37   : CF/PPS 3 a) before TR (front), b) after TR (front), c) after TR (back), d) after
TR and cleaning (front), e) after TR and cleaning (back)

Summary and discussion

In Figure 4.38, the evolution of the CF/PPS sample and the enclosures from the outside
through the TR process is observed. It can be seen that the thermocouples did not remain
attached to the sample by the end of the experiments. The difference in behavior between
the pictures of 5 seconds after the first flame is also noticeable. CF/PPS 1 presents some
sparks, CF/PPS 2 presents smoke, and CF/PPS 3 suffers an abrupt rupture, and the flame
escapes by the sample.

Figure 4.38 : CF/PPS 1, 2, and 3 samples and flame evolution from outside the enclosure during TR

At Figure 4.39, the thermal images of the samples CF/PPS 1, 2, and 3 are presented during the TR processes. At the maximum temperature pictures, the difference already

commented on in the temperature distribution between samples 1 and 2 can be observed. The first one presents a uniform distribution, while the second does not.

Figure 4.39   : CF/PPS 1, 2, and 3 samples thermal evolution during TR

Figure 4.39 shows a comparison of the maximum temperature at each point of the sample for the three repetitions as well as the maximum differential pressure at which they were exposed. With this graph, the difference between the temperature distribution among the different samples can be noticeable again. While CF/PEEK 1 presents a more uniform behavior along the whole specimen, CF/PEEK 2 and 3 present greater differences. CF/PPS 2 presents the highest maximum differential pressure, while the lowest one is presented at CF/PPS 3.

Figure 4.40   : CF/PPS 1, 2, and 3 sample temperatures and
pressure summary

In figures Figure 4.41 and Figure 4.41, the mass loss of the CF/PPS samples is presented
in grams and percentages, respectively. In this case, the mass loss corresponds to the
level of degradation/rupture of the sample; the first sample is the one with lower material
degradation and ML, 0.68%, followed by the second one, 2.32%, and finally, the third
one, which suffered a rupture presents an ML of 4.70%.
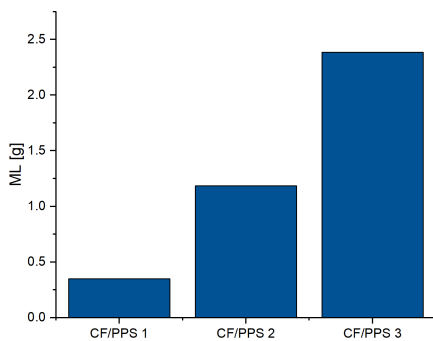
Figure 4.41   : CF/PPS 1, 2, and 3 ML [g]
after TR
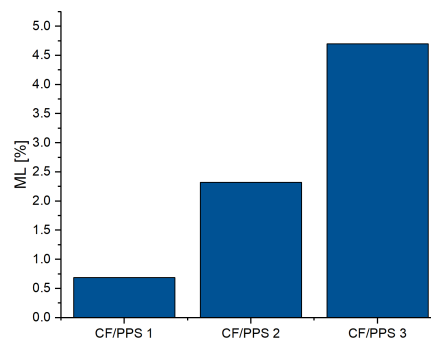
Figure 4.42   : CF/PPS 1, 2, and 3 ML [%]
after TR

GF/PPS

GF/PPS 1 results

The Figure 4.43 presents the temperature evolution at different sample parts. It can be observed that the temperature is uniform in the whole sample for the first 25 seconds after it starts heating, and from that point on, the corner middle left top and the right bottom corner present higher temperatures than the left side of the sample.
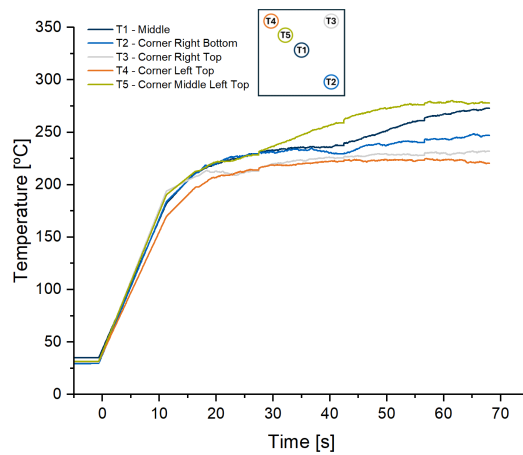
Figure 4.43   : GF/PPS 1 thermal camera measurements during TR test

Figure 4.44 shows the sample evolution through the whole process. A change of color and a slight swelling between before TR Figure 4.44 a, and after TR Figure 4.44 b and c are visible. Figure 4.44 e shows material degradation in the form of open plies at the back of the sample concentrated in the middle and expanding to the outside.
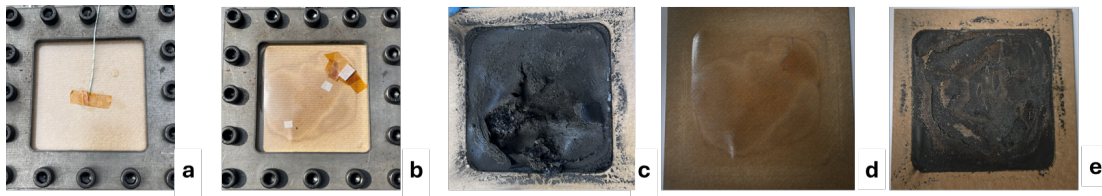
Figure 4.44   : GF/PPS 1 a) before TR (front), b) after TR (front), c) after TR (back), d) after TR and cleaning (front), e) after TR and cleaning (back)

GF/PPS 2 results

The Figure 4.43 presents the temperature evolution at different sample parts. It can be observed that the temperature is uniform in the whole sample for the first 20 seconds after it starts heating, and from that point on, the top and the left side of the sample present higher temperatures than the CRB and the middle of it.
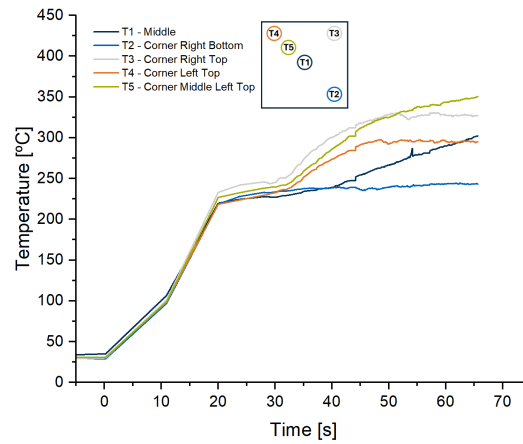
Figure 4.45   : GF/PPS 2 thermal camera measurements during TR test

Figure 4.46 shows the sample evolution through the whole process. A change of color and a slight swelling between before TR Figure 4.21 a, and after TR Figure 4.21 b and c is visible. The swelling is concentrated on the left side of the sample, in which the temperatures were higher than in other regions. Figure 4.21 e shows a greater material degradation, in the form of open plies, on one of the sides expanding to the side in front of it.

Figure 4.46   : GF/PPS 2 a) before TR (front), b) after TR (front), c) after TR (back), d) after TR and cleaning (front), e) after TR and cleaning (back)

GF/PPS 3 results

The Figure 4.43 presents the temperature evolution at different sample parts. It can be observed that the temperature is uniform in the whole sample for the first 25 seconds after it starts heating, and from that point on, the highest temperatures are concentrated in the middle of the sample (T1 and T5).

Figure 4.47   : GF/PPS 3 thermal camera measure-
ments during TR test

Figure 4.48 shows the sample evolution through the whole process. A change of color and a slight swelling between before TR Figure 4.48 a, and after TR Figure 4.48 b and c are visible. The swelling is concentrated in the middle region, where the temperatures were higher than in other sample regions. Figure 4.48 e shows a similar material degradation as samples 1 and 2; in this case, the worst part of the open plies is concentrated in the middle, expanding to the sides in a concentric way.

Figure 4.48   : GF/PPS 3 a) before TR (front), b) after TR (front), c) after TR (back), d) after TR and cleaning (front), e) after TR and cleaning (back)

Summary and discussion

In Figure 4.49, the evolution of the GF/PPS sample and the enclosures from the outside through the TR process is observed. It can be seen that only the thermocouples of the GF/PPS 1 and 3 resisted attached to the samples, while on the GF/PPS 2 no. The GF/PPS 1 presents mainly smoke, GF/PPS presents a more noticeable flame, and GF/PPS 3 presents sparks.

GF/PPS 1　　　**GF/PPS 2**　　　**GF/PPS 3**
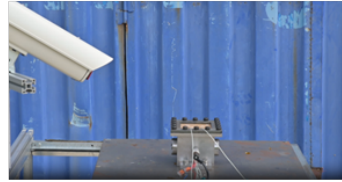
Beginning of the experiment
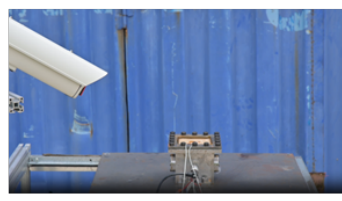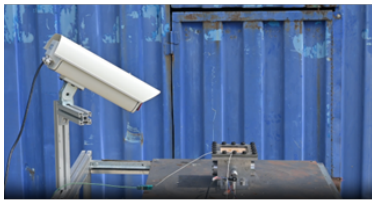
5 seconds before flame
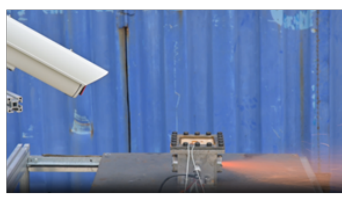
First flame

5 seconds after flame

End of the experiment

Figure 4.49　: GF/PPS 1, 2, and 3 samples and flame evolution from outside the enclosure during TR

At Figure 4.50, the thermal images of the samples CF/PEEK 2 and 3 are presented during the TR processes. A more uniform distribution of temperatures at GF/PPS 1 and 3 can be observed, while GF/PPS 2 presents a difference between one-half of the sample and the other one, which corresponds to the swelling.
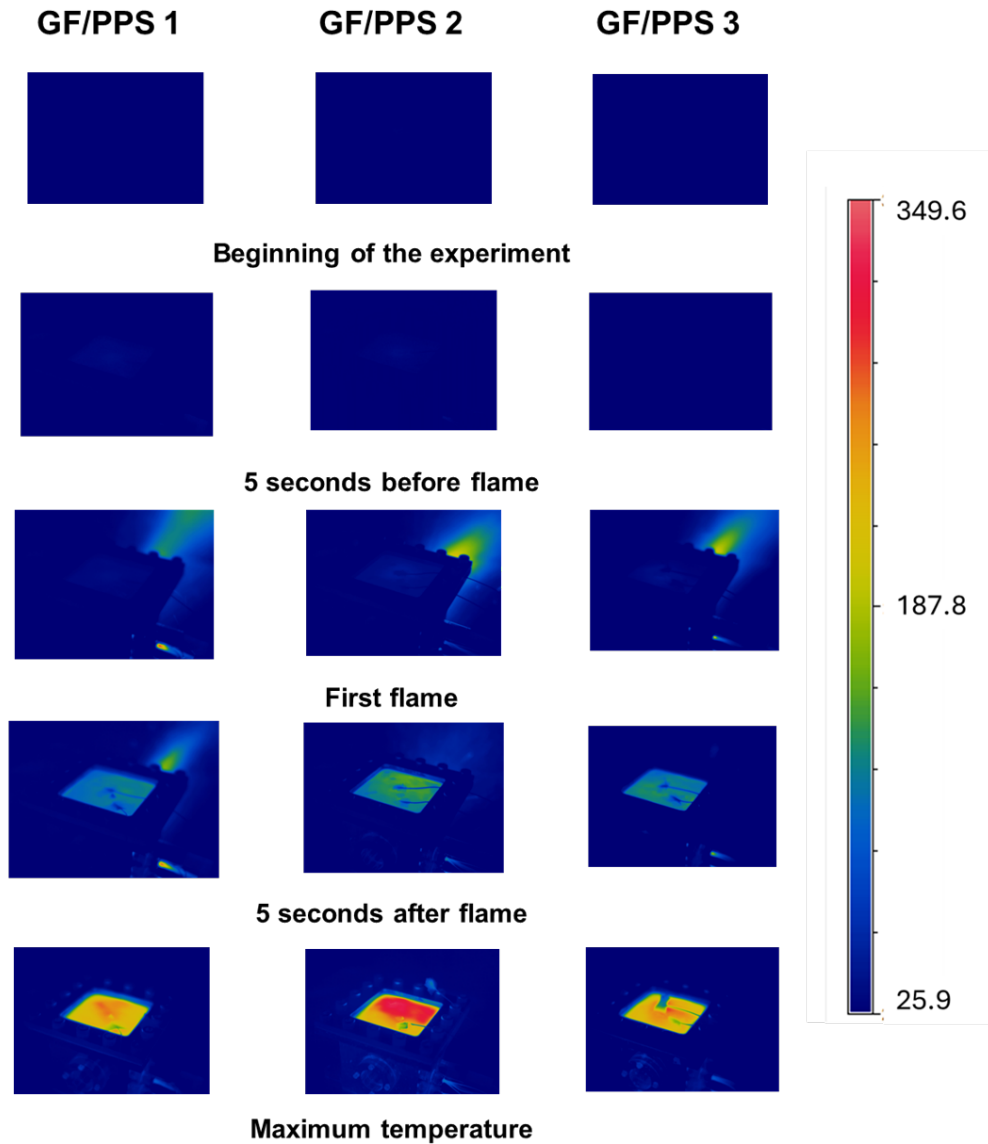
Figure 4.50   : GF/PPS 1, 2, and 3 samples thermal evolution during TR

Figure 4.54 shows a comparison of the maximum temperature at each point of the sample for the three repetitions as well as the maximum differential pressure at which they were exposed. While CF/PEEK 1 and 3 present similar values and distribution of maximum temperatures in all the points studied, sample 2 presents higher values of maximum temperatures. The maximum differential pressure is greater in the first sample, followed by the second one and the third one.
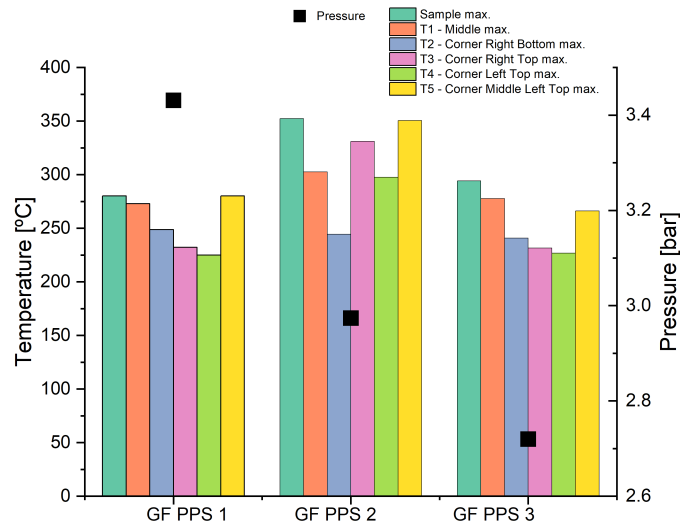
Figure 4.51   : GF/PPS 1, 2, and 3 sample temperatures and
pressure summary

In figures Figure 4.55 and Figure 4.56, the mass loss of the GF/PPS samples is presented
in grams and percentages, respectively. It is observed that sample 3 presents the maxi-
mum ML, 8.76%, while sample 1 is the lowest, 4.89%. The second sample presents an
ML of 7.41%.
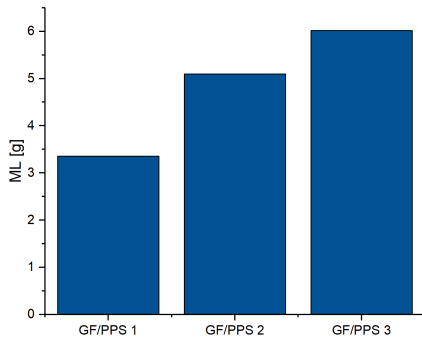
Figure 4.52   : GF/PPS 1, 2, and 3 ML [g]
after TR
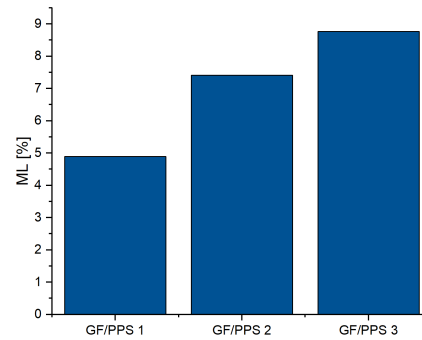
Figure 4.53   : GF/PPS 1, 2, and 3 ML [%]
after TR

PPS matrix discussion

In this section, the differences in temperature behavior depending on the type of fiber
employed are presented. At Figure 4.54, Figure 4.55 and Figure 4.56, it can be observed
that with the GF/PPS combination, the repeatability of the experiments is higher as
the temperatures follow similar tendencies in the three points compared. CF/PPS does

not present the repeatability that GF/PPS presents firstly because of the difference of temperatures between the first and the second sample, as seen in the graphs, and also because of the rupture already mentioned in sample 3.

The lower steep at GF/PPS was expected, taking into account that the E glass employed for GF/PPS presents a thermal conductivity of 1.3 W/(m K) [10], while the carbon HT 3k presented a higher thermal conductivity, 8.5 W/(m K) [50]; which explains a steeper slope in the thermal behavior CF/PPS. This behavior on the slopes was expected and also observed in the literature [14]. Moreover, the lower thermal conductivity behavior of GF/PPS can also be appreciated when analyzing the maximum enclosure temperature. On average, the maximum temperatures reached at the enclosure when using GF/PPS composites were higher than in the CF/PPS composites. When looking at the graphs, it can be observed that CF/PPS composites present higher temperature values in most of the points compared, while the enclosure temperature was lower than at the GF/PPS tests.
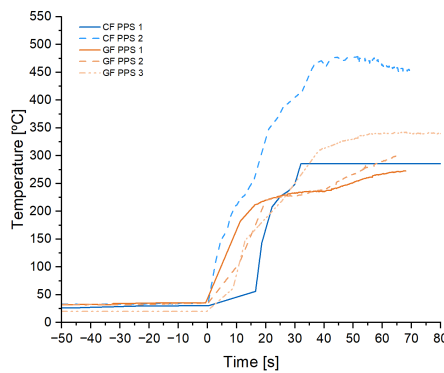
Figure 4.54   : CF/PPS and GF/PPS sample middle-temperature summary
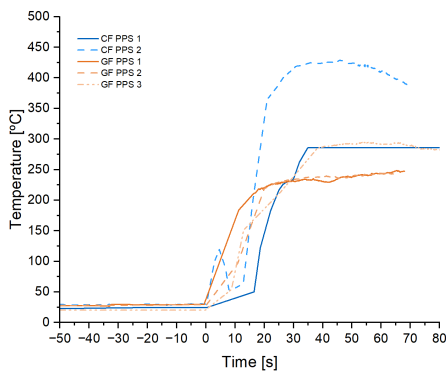
Figure 4.55   : CF/PPS and GF/PPS sample corner right bottom temperature summary
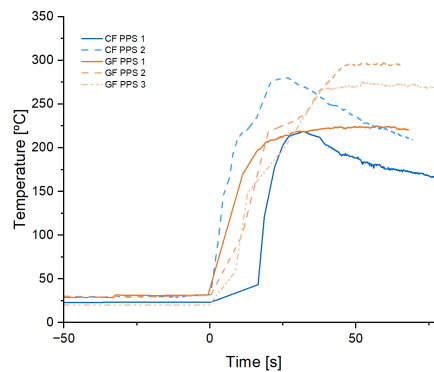
Figure 4.56   : CF/PPS and GF/PPS sample corner left top temperature summary

4.1.3 Discussion

In this section, a final summary of the multi-cell 21700 TR experiments is found. On the Figure 4.57, the average value of the maximum temperatures of each sample repetition is found with its standard deviation. It can be observed that, except for the CF/PPS samples, the repeatability of the experiments is similar, as can be observed in their respective standard deviations of maximum temperatures and differential pressure. It can be observed that the greatest differential pressures are found when using PPS matrices. Regarding higher temperatures, CF/PPS presents the highest temperatures, followed by the composites with GF.
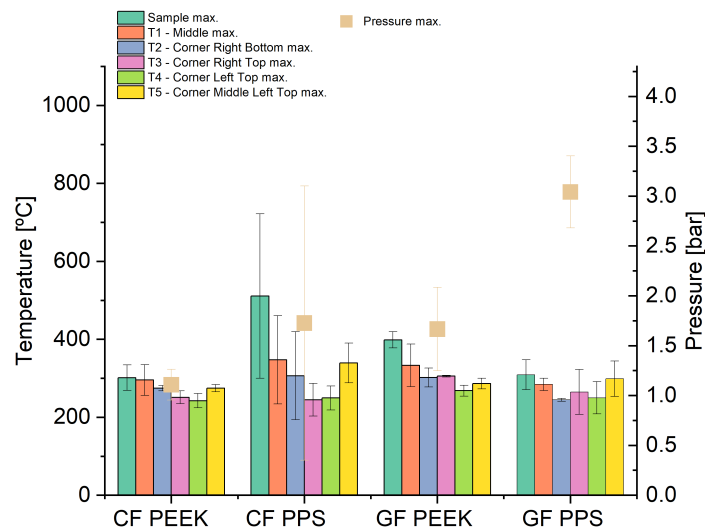
Figure 4.57 : CF/PEEK, GF/PEEK, CF/PPS, GF/PPS summary of the behavior under TR

In terms of ML Figure 4.58 presents the average ML in % and their standard deviations for each type of material tested. The lowest standard deviation and the lowest ML are in CF/PEEK. CF/PPS has the seconds lowest ML but the standard deviation is the highest, GF/PPS presents also a high standard deviation and the highest ML, this shows that using PPS decreases the repeatability of the experiments in terms of ML. When using PEEK, the repeatability in terms of ML is greater.
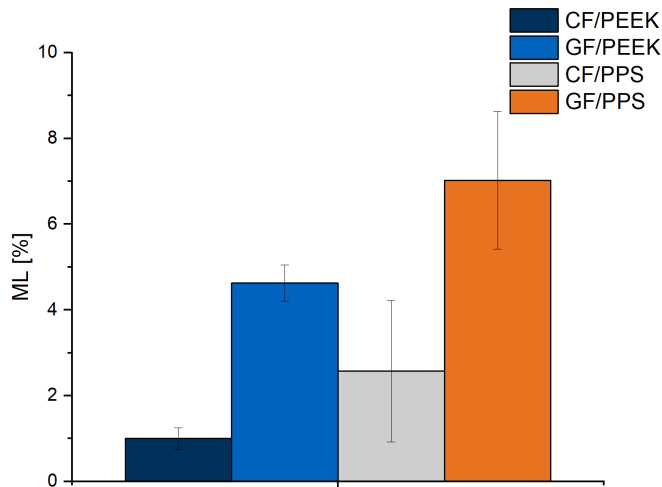
Figure 4.58   : CF/PEEK, GF/PEEK, CF/PPS, GF/PPS summary of the ML in % after TR

To conclude, in terms of maximum temperature and pressure, the repeatability is higher when using GF; in terms of ML, the repeatability is higher when using PEEK matrices.

4.2 Cell 4695 TR results

4.2.1 Calibration test with steel plate

For the calibration test for the 4695 cell, a steel plate was used.

At Figure 6.25, it can be observed that almost every thermocouple failed during the recording, and only one of the environment thermocouples connected to the Quantum X worked properly during the whole experiment.

The thermocouple of the Arduino only worked from the beginning of the experiment till the beginning of the TR; for the time measured, the heating rate was 11.2206 ºC/min. One of the purposes of this experiment was to check that the 4695 achieved TR when wrapped by 3 thermocouples and which heating rate the cell would have.

In Figure 6.26, it can be observed that the maximum differential pressure reached the enclosure was 2.722 bar, achieved at the TR; other peaks follow this first initial peak but with lower pressure.
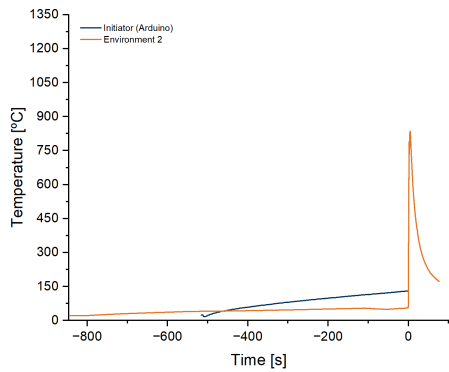
Figure 4.59 : STEEL thermocouple measurements during TR test
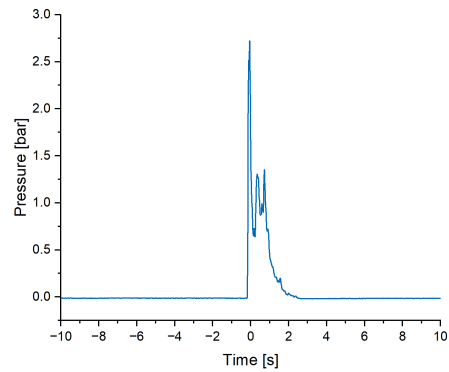
Figure 4.60 : STEEL pressure measurement during TR test

The Figure 4.43 presents the temperature evolution at different sample parts. It can be observed that the temperature follows a similar evolution in the whole sample, the greatest temperatures are found at the middle of the sample (T1 and T5).
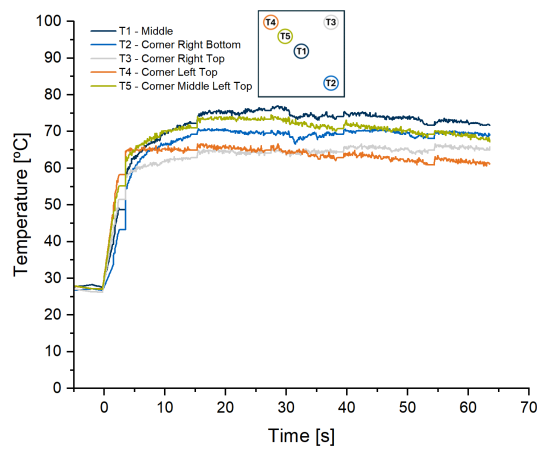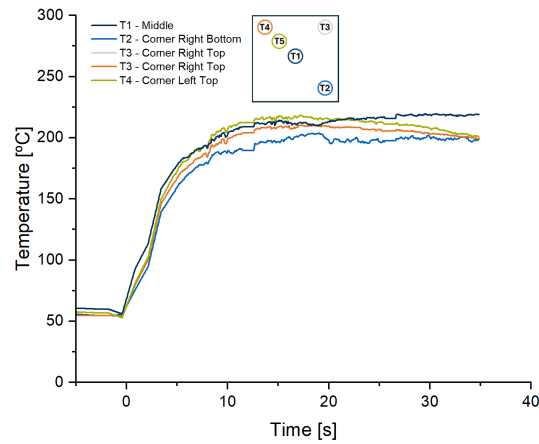

Figure 4.61 : STEEL thermal camera measurements during TR test

Figure 4.62 shows the sample evolution through the whole process. The whole sample, Figure 4.62 b and c, was covered with emissivity tape to obtain the exact temperatures with the thermal camera. Figure 4.62 d presents all the residues encrusted on the back after the TR.
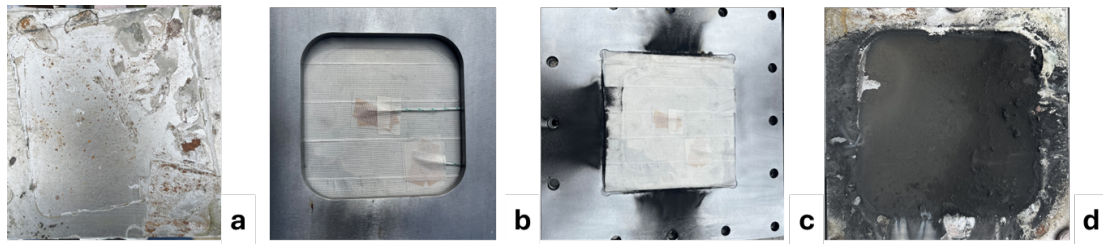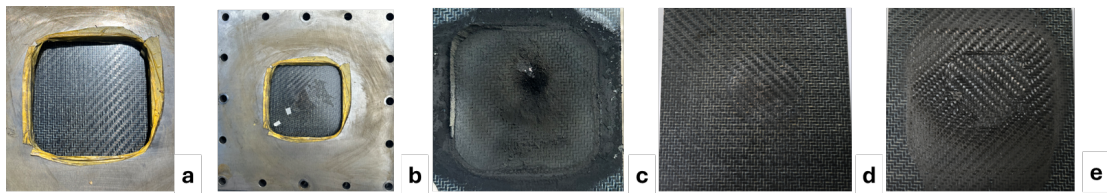
Figure 4.62 : STEEL a) before TR (front), b) after TR (front), c) after TR (back), d) after TR and cleaning (front), e) after TR and cleaning (back)

In Figure 4.63, the evolution of the STEEL sample and the enclosures from the outside through the TR process is observed. It can be seen that at the moment of the first flame, the smoke goes out from the enclosure by the orifice and by the middle of the two tapes.

Beginning of the experiment

5 seconds before flame

First flame

5 seconds after flame

End of the experiment

Figure 4.63 : Steel sample and flame evolution from outside the enclo-
sure during TR

At Figure 4.64, the thermal images of the steel sample are presented during the TR
processes. It can be observed that the sample temperature rises in an almost uniform
distribution, as already commented on the graphs.

Beginning of the experiment

5 seconds before flame

First flame

5 seconds after flame

Maximum temperature
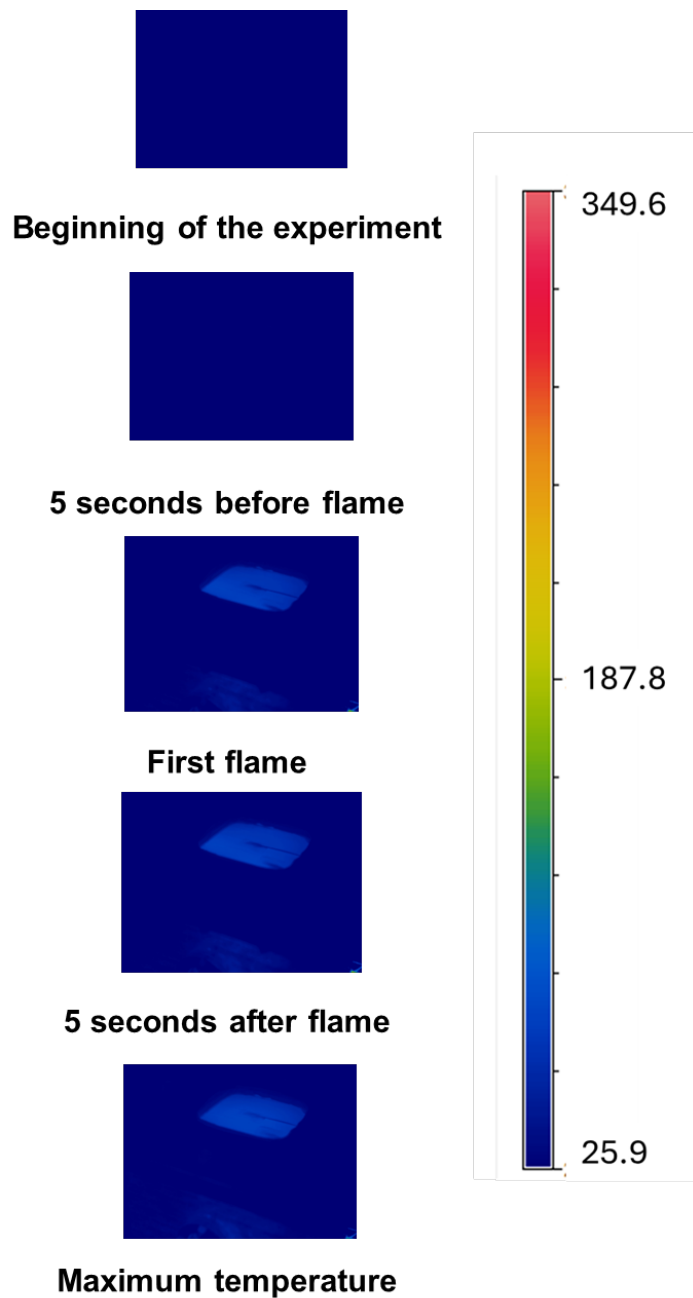
Figure 4.64   : Steel sample thermal evolution during TR

From Figure 4.63 and Figure 4.64, it can be observed that neither the flame nor the temperatures achieved were as expected on first hand. The reason for this behavior can be found in Figure 4.65; the cell fell over because it was placed wrongly; the vent cup was placed on the bottom, and the TR made it fall over. For the rest of the experiments with 4695, the vent cup was placed properly and fixed for stabilization.

Figure 4.65 : 4695 cell at calibration test after TR

4.2.2 CF/PC results

For the CF/PC temperature recording, only the information on the thermocouples was stored; the thermal camera was not used for security reasons, as the behavior of this combination could not be predicted.

The Figure 6.27 shows the measurements of the thermocouples during the TR experiment. It can be observed a slight peak at -40 seconds in the initiator temperature measurements; this is related to the ejection of the vent cup. The ejection of the vent cup is also observable at Figure 6.28 at -40 seconds when there is a small peak on the differential pressure at the enclosure; there is only another peak of pressure, the one that corresponds to the TR.

In the case of the temperature measurement of the laminate, the corner temperature presents a steeper slope than the one in the middle. Moreover the temperatures reached at the corner of it are higher than at the middle. From the second 50, there is an error in the measurement of the laminate middle.
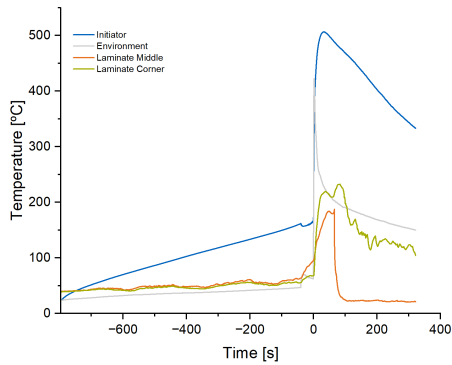
Figure 4.66 : CF/PC thermocouple measurements during TR test
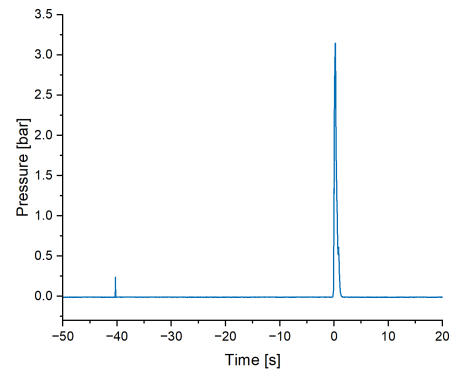
Figure 4.67 : CF/PC pressure measurement during TR test

Figure 4.68 shows the sample evolution through the whole process. A change of color is hardly noticeable between before TR Figure 4.68 a, and after TR Figure 4.48 b and d is visible. Some signals of material degradation, in the form of open plies in the middle and one of the corners, are shown at Figure 4.68 e.
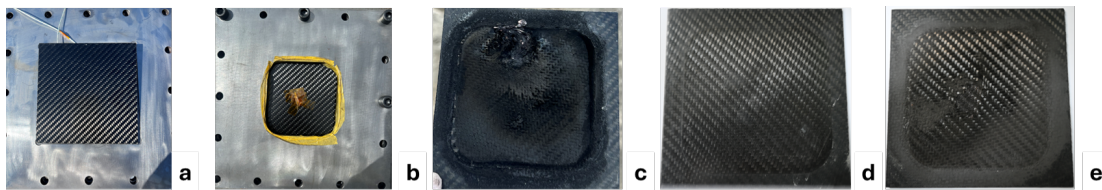
Figure 4.68 : CF/PC a) before TR (front), b) after TR (front), c) after TR (back), d) after TR and cleaning (front), e) after TR and cleaning (back)

4.2.3 CF/PEEK 4 results

The Figure 4.69 presents the temperature evolution at different sample parts. It can be observed that the slope is the same for all parts of the sample once the steeper heating process begins. Once it arrives at 200ºC, the heating curve of the middle of the sample (T1 and T5) is steeper than on the rest of the sample.
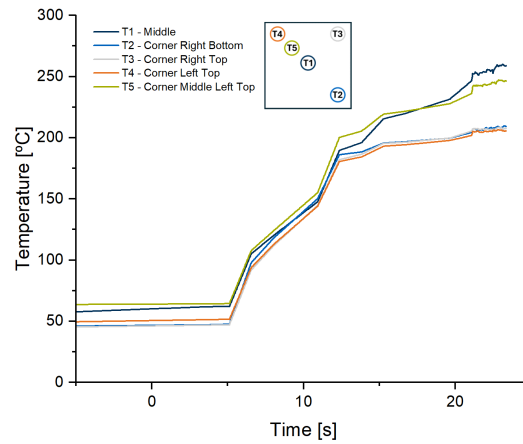
Figure 4.69   : CF/PEEK 4 thermal camera measurements during TR test

Figure 4.70 shows the sample evolution through the whole process. A change of color between before TR Figure 4.70 a, and after TR Figure 4.44 b and d is visible. Figure 4.70 e shows open plies at the back of the sample, mainly concentrated in the midpoint between the center and one of the corners.
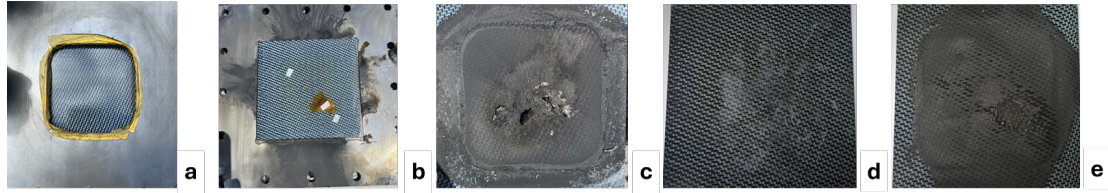
Figure 4.70   : CF/PEEK 4 a) before TR (front), b) after TR (front), c) after TR (back), d) after TR and cleaning (front), e) after TR and cleaning (back)

4.2.4 CF/PPS 4 results

The Figure 4.69 presents the temperature evolution at different sample parts. It can be observed that the slope is the same for all parts of the sample once the steeper heating process begins. The middle part has the highest temperature values, while CRB has the lowest.

97

Figure 4.71　: CF/PPS 4 thermal camera measurements during TR test

Figure 4.72 shows the sample evolution through the whole process. A slight change of color between before TR Figure 4.72 a, and after TR Figure 4.72 b and d is visible. Figure 4.72 e shows material degradation at the back of the sample, mainly concentrated between the middle of the sample and one of the sides and in the form of open plies.

Figure 4.72　: CF/PPS 4 a) before TR (front), b) after TR (front), c) after TR (back), d) after TR and cleaning (front), e) after TR and cleaning (back)

4.2.5　Discussion

In Figure 4.73, the evolution of the GF/PPS sample and the enclosures from the outside through the TR process is observed. It can be seen that all the thermocouples of the samples studied resisted attached to them. It can also be seen that on the moment of the first flame in the CF/PC sample, some smoke gets out of the enclosure through the two lids. In all cases, there was more smoke than fire or sparks.

Figure 4.73 : CF/PC, CF/PEEK, CF/PPS sample and flame evolution from outside the enclosure during TR

At Figure 4.74, the thermal images of the samples CF/PEEK 4 and CF/PPS 4 are presented during the TR processes. It can be seen that at CF/PPS 4, at the moment of the first flame, heat was released through the gap of the lids. In both cases, an almost uniform distribution of temperatures is observed after the first flame. In the instant of maximum temperature, the middle region of both presents higher temperatures than the rest of the sample.
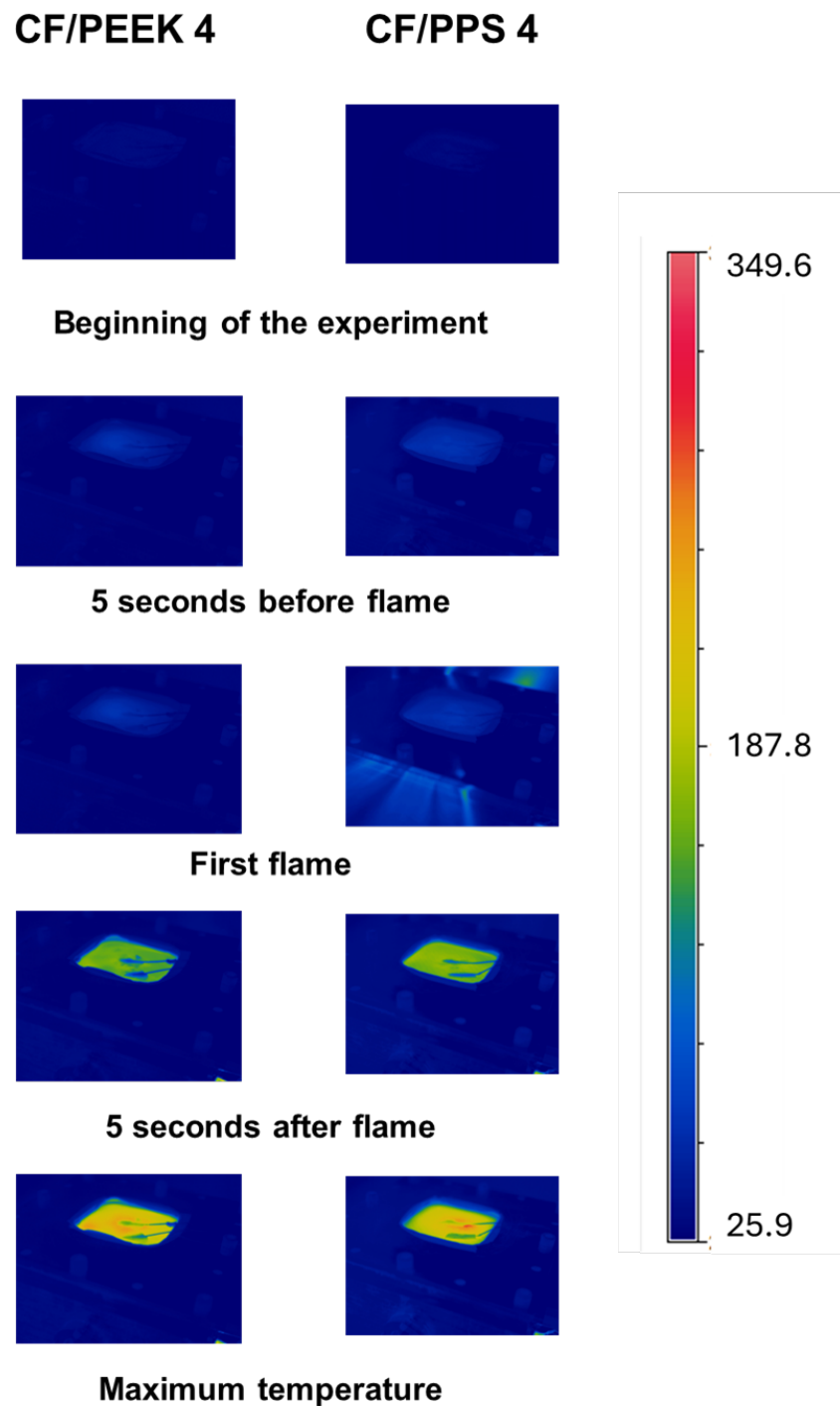
Figure 4.74   : CF/PEEK, CF/PPS sample thermal evolution during TR

Figure 4.54 compares the maximum temperature at each point of the sample for the CF/PC, CF/PEEK 4, and CF/PPS and the maximum differential pressure at which they were exposed. While CF/PEEK 4 and CF/PPS 4 present similar values and distribution of maximum temperatures in all the points studied and similar values of maximum differential pressure, the temperature values of CF/PC are lower, and its maximum differential pressure is higher.
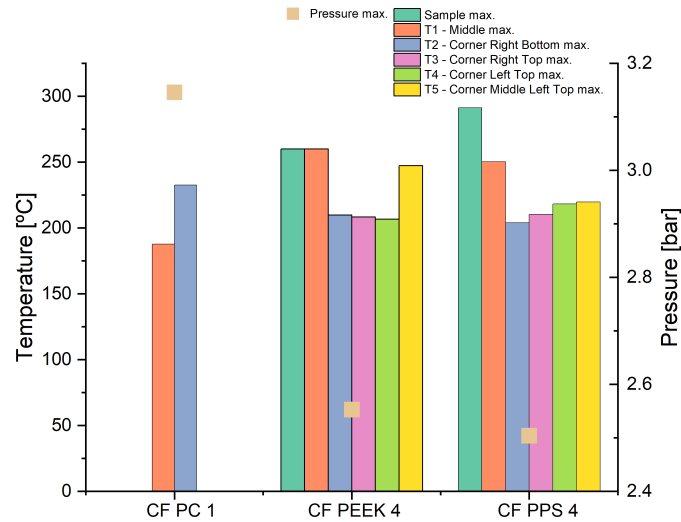
Figure 4.75 : CF/PC, CF/PEEK, CF/PPS summary of the behavior under TR

In figures Figure 4.55 and Figure 4.77, the mass loss of the samples tested with the 4695 cells is presented in grams and percentages, respectively. It is observed that the use of the PC matrix has the highest ML, with a value of 1.36%, while the PPS matrix has the lowest, 0.56%. CF/PEEK material presents a ML of 0.80% after TR and cleaning.
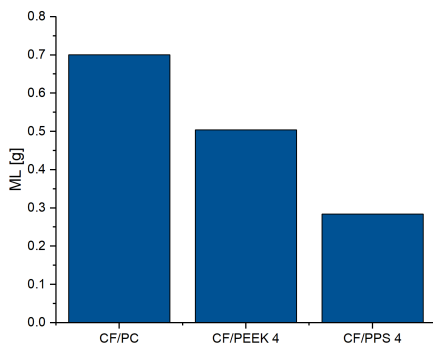
Figure 4.76 : CF/PC, CF/PEEK 4 and CF/PPS 4 ML [g] after TR

Figure 4.77 : GF/PPS 1, 2, and 3 ML [%] after TR

101
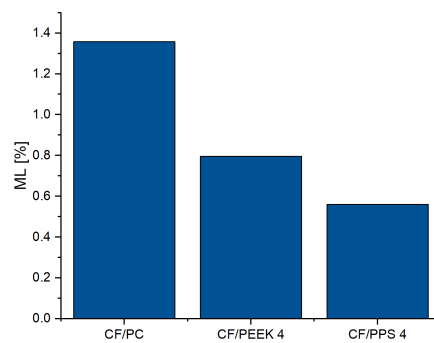
CF/PEEK combination is a trade-off between the thermal properties of CF/PC and the ML loss of CF/PPS because CF/PEEK was the second sample with the lowest temperatures and the second one with the lowest ML.

5 Evaluation

This section aims to screen the materials to determine which presents the best performance regarding the TR test developed in this project.

The first step for screening the materials is to collect all the relevant data from the different experiments; this can be found at Table 5.1. The information in the table is distributed as follows:

- Type of cell and number of cells employed for each sample.

- Material with failed structural integrity: Yes, the material got a trough-thickness fracture during the TR.

- Information at the beginning of the experiment: temperatures and pressure.

- Time to reach TR.

- Heating rate of the initiator cell.

- Information at the TR instant: Temperatures and pressure.

- Maximum temperatures and differential pressure during the experiment.

- Physical data: Thickness, weight before TR, after TR, and after TR and cleaning, and the respective mass loss.

Some remarks about the data from Table 5.1. For the environment temperatures when more than one sensor was shown in the graph, only one was selected these were: Sensor 1 in CF/PPS 2, CF/PPS 3 GF/PEEK 1 and GF/PPS 3; and sensor 2 in CF/PPS 1, GF/PPS 1, GF/PPS 2 and steel. When the thermocouples of the samples did not work, the data for the initial data and the TR were extracted from the thermal camera at CF/PPS 2, GF/PEEK 2, GF/PPS 1, and GF/PPS 3.

Table 5.1 : Summary of studied variables for 21700 and 4695 experiments and samples tested

Variable	STEEL	CF/PC	CF/PEEK 1	CF/PEEK 2	CF/PEEK 3	CF/PEEK 4	GF/PEEK 1	GF/PEEK 2	GF/PEEK 3	CF/PPS 1	CF/PPS 2	CF/PPS 3	CF/PPS 4	GF/PPS 1	GF/PPS 2	GF/PPS 3
Type of cell	4695	4695	21700	21700	21700	4695	21700	21700	21700	21700	21700	21700	4695	21700	21700	21700
Number of cells	1	1	7	7	7	1	7	7	7	7	7	7	1	7	7	7
Material with failed structural integrity	NO	NO	NO	NO	NO	NO	NO	NO	NO	NO	NO	YES	NO	NO	NO	NO
Initial differential pressure [bar]	-0.015	-0.014	-0.013	-0.011	-0.008	-0.008	-0.005	-0.017	-0.009	-0.016	-0.011	-0.008	-0.001	-0.010	-0.014	-0.015
Initial temperature cell [ºC]	24.250	23.480	31.750	28.660	25.820	31.760	42.760	30.070	19.630	20.630	28.210	29.280	34.630	25.740	28.500	23.320
Initial enclosure environment temperature [ºC]	20.610	23.600	28.820	30.050	36.040	33.530	-	31.430	31.720	21.510	29.910	31.110	43.930	27.910	30.310	23.220
Initial temperature sample middle [ºC]	20.000	38.280	33.390	30.000	33.200	34.800	41.900	37.000	20.000	23.500	29.700	35.700	20.000	25.700	25.300	20.000
Initial temperature sample CRB [ºC]	20.000	37.460	33.330	30.200	33.200	34.400	42.200	32.100	20.000	22.400	28.300	33.000	20.000	25.700	23.700	20.000
Time to reach TR [s]	516.421	796.000	185.000	195.000	198.000	684.000	384.000	186.000	224.000	166.000	185.000	207.000	656.000	198.000	149.000	187.000
HEATING RATE [ºC/min]	11.221	9.938	36.422	40.231	-	12.189	36.937	32.750	-	18.301	30.013	22.857	-	34.049	35.080	32.642
HEATING RATE [ºC/s]	0.187	0.166	0.607	0.671	-	0.203	0.616	0.546	0.267	0.305	0.500	0.381	0.263	0.567	0.585	0.544
Differential pressure at TR [bar]	1.476	1.261	0.868	-0.011	0.000	0.631	0.363	0.898	-	0.058	0.002	-0.006	-	0.240	-0.010	-0.014
Initiator cell temperature at TR [ºC]	130.250	167.910	140.000	178.200	-	198.640	158.210	138.180	-	140.360	131.000	114.340	123.690	141.740	116.000	135.950
Enclosure environment temperature at TR [ºC]	67.530	68.050	40.089	47.250	52.720	160.960	-	118.950	37.680	27.120	41.760	35.150	75.700	39.060	43.250	34.370
Sample middle temperature at TR [ºC]	28.100	95.940	38.720	42.330	35.000	69.270	55.970	37.5	32.270	30.610	39.570	40.090	62.300	41.830	38.790	23.200
Sample CRB temperature at TR [ºC]	27.000	68.230	35.200	29.300	32.640	52.480	53.470	35.5	27.120	26.520	34.260	42.640	-	38.300	34.650	23.100
Differential pressure max. [bar]	2.722	3.146	1.247	1.134	0.943	2.553	2.137	1.333	1.529	1.218	3.283	0.678	2.504	3.431	2.974	2.720
Initiator cell max. temperature [ºC]	-	506.390	1202.500	1365.500	-	581.350	1057.100	1025.600	539.330	1370.400	1057.700	242.220	700.100	970.780	1023.750	1375.000
Enclosure max. temperature [ºC]	835.700	422.670	1090.600	1373.800	1000.000	752.750	994.170	994.670	388.500	409.170	886.390	119.160	291.200	722.240	1216.900	900.360
Sample max. temperature [ºC]	87.200	214.870	338.890	285.000	280.800	260.000	422.600	384.500	342.300	285.500	543.200	703.500	250.200	280.100	352.300	294.100
Sample CRB max. Temperature [ºC]	77.000	187.000	273.330	267.300	280.800	209.700	382.400	282.300	294.700	285.500	478.100	278.900	203.900	272.900	302.500	277.700
Average thickness [mm]	71.000	2.041	2.438	2.470	2.445	2.439	2.278	2.246	2.293	1.969	1.932	1.926	1.926	2.059	2.071	2.062
Weight before TR [g]	-	51.601	63.037	63.921	63.305	63.304	75.105	74.922	75.168	50.950	50.985	50.786	50.684	68.657	68.798	68.615
Weight after TR [g]	-	53.300	95.700	71.000	84.700	65.900	98.700	95.800	104.200	88.000	77.600	48.700	53.000	72.100	95.600	76.900
Weight after TR and cleaning [g]	-	50.900	61.000	61.800	60.900	62.800	71.400	71.900	71.600	50.600	49.800	48.400	50.400	65.300	63.700	62.600
Mass loss before cleaning [g]	-	-1.699	-32.663	-7.079	-21.395	-2.596	-23.595	-20.878	-29.032	-37.050	-26.615	2.086	-2.316	-3.443	-26.802	-8.285
Mass loss before cleaning [%]	-	-3.293	-51.815	-11.075	-33.796	-4.101	-31.416	-27.866	-38.622	-72.719	-52.202	4.108	-4.570	-5.014	-38.957	-12.074
Mass loss after cleaning [g]	-	0.701	2.037	2.121	2.405	0.504	3.705	3.022	3.698	0.350	1.185	2.386	0.284	3.357	5.098	6.015
Mass loss after cleaning [%]	-	1.358	3.232	3.318	3.800	0.796	4.933	4.034	4.911	0.687	2.324	4.698	0.560	4.890	7.410	8.767

5.1 Parameters evaluation

On the first hand, it is decided to compare the 4695 and the 21700 experiments as the conditions of TR in both of them should be theoretically similar, taking into account the energy (six 21700 cells correspond to one 4695 cell) and volume (6.51 cells corresponds to one 4695 cell) relations previously calculated at subsection 3.1.2. Three parameters are selected and normalized to compare the different experiments.

- Temperature ratios between the maximum enclosure environment temperature and the maximum sample temperature.

- Temperature difference along the sample: Absolute percentage temperature increases between the maximum temperature at the middle of the sample and at the corner right bottom.

- Percentage of mass loss between the weight of the sample before TR and after TR and the cleaning process.

Once the parameters are normalized, each sample obtains a score depending on its performance regarding that parameter, with 5 as the maximum score assigned to the material with the greater performance and 0 as the minimum assigned to the material with the worst performance. For the final evaluation, the score obtained from the percentage of mass loss will get a weight of 60%, while the other two parameters will be multiplied by a weight of 20%. The reason for these percentages is based on the safety performance of the samples, as with a high mass loss, the sample has a lower capability of maintaining security due to a complete rupture or a high material degradation.

For a better understanding of the behavior of the material's thermal conductivity, the following Table 5.2 indicates the thermal conductivity for each fiber and matrix employed and the thermal conductivity calculated according to the volume in fiber for every combination tested (rule of mixture). The table also indicates the fiber architecture used for every composite.

Material	Thermal conductivity [W/(m K)]
CF	8.5 [50]
GF	1.3 [10]
PEEK	0.23 [15]
PPS	0.3 [56]
PC	0.23 [85]
CF/PC (Twill 2/2)	3.95
CF/PEEK (Atlas 5HS)	4.36
GF/PEEK (US 7781)	0.77
CF/PPS (Twill 2/2)	4.4
GF/PPS (Style 7628)	0.8

Table 5.2 : Thermal conductivity of fibers, matrices and composite materials tested

5.1.1 Temperature ratios

For the LIB enclosure safety, it is important that the material that encloses the LIB transmits the lowest amount of heat released by the cells in the case of TR to the rest of the aircraft. That means that the factors to screen the materials are their conductivity and heat capacity.

To shorten the materials, the temperature ratios between the temperature at the enclosure environment and the temperature at the sample are performed. After performing this ratio, the materials are shorted by a scoring system in which the best ratio gets 5 points, and the rest of the ratios are compared to the best one to calculate their score.

At Table 5.3, each sample's maximum temperature ratios and scores are collected. For the GF/PEEK 1, due to the lack of the maximum enclosure environment temperature, the sample gets the average score between the other two samples with the same fiber and resin and the same type of cell.

Analyzing the samples tested by the multi-cell experiment, GF/PPS was supposed to obtain and obtain high scores in this parameter as it has a low thermal conductivity (0.8 W/ (m K)). However, GF/PEEK, which was supposed to obtain a great score in this parameter study as it has the lowest thermal conductivity from the materials studied (0.77 W/ (m K)), obtains one of the lowest scores. There are several hypotheses that can explain this unexpected behavior. It is suggested that these variations from the expected behavior are due to the differences in the environmental conditions in which the experiments were performed as well as the internal conditions inside the battery enclosure since the conditions of each TR are different, such as the time needed for the TR to begin, the magnitude of the explosion, the type of explosion of the surrounding cells, among others. Another factor that can influence the differences in behavior between composites with the same fiber material is that the manufacturer may have employed different types of CF or GF for each type of material, which could influence the thermal behavior. Finally, it is suggested that this difference in behavior, while having similar thermal conductivity values, can also be due to the fiber architecture as GF/PEEK has a US 7781 architecture style and GF/PPS has a Style 7628 architecture. The same happens with CF/PEEK, in which CF presents Atlas 5HD architecture, and CF/PPS, in which CF presents Twill 2/2.

Unexpected behavior is also observed in the single-cell experiment, where the CF/PEEK and CF/PPS present higher values of thermal conductivity but obtain better scores than CF/PC with a lower thermal conductivity value. Again, a possible explanation of this behavior can be due to variations in the environmental conditions and the TR of the cells, as well as different types of carbon fibers between composites that the manufacturer may have employed in their elaboration.

Finally, comparing the scores between the same material in the single-cell experiments and the multi-cell experiments, it can be observed that both CF/PEEK and CF/PPS obtain higher values in comparison with the sample materials when tested under the single-cell experiment. This behavior results from the explosions in the single-cell test being less intense and involving less fire than those in the multi-cell test.

Sample	Max. enclosure environment temperature [ºC]	Max.sample middle temperature [ºC]	Max. temperature ratio	Score
CF/PC	422.67	214.87	1.97	3.3
CF/PEEK 1	1090.60	338.89*	3.21	2.0
CF/PEEK 2	1373.80	285.00	4.82	5.0
CF/PEEK 3	1000.00	280.80	3.56	3.7
CF/PEEK 4	752.75	260.00	2.90	3.0
GF/PEEK 1	-	422.60	-	2.1
GF/PEEK 2	994.67	384.50	2.59	2.7
GF/PEEK 3	539.33	388.50	1.39	1.4
CF/PPS 1	409.17	285.50	1.43	1.5
CF/PPS 2	886.39	543.20	1.63	1.7
CF/PPS 3	119.16	703.50	0.17	0.2
CF/PPS 4	700.10	291.20	2.40	2.5
GF/PPS 1	722.24	280.10	2.58	2.7
GF/PPS 2	1216.90	352.30	3.45	3.6
GF/PPS 3	900.36	294.10	3.06	3.2

Table 5.3   : Maximum temperature ratios and screening scores, *maximum temperature at the middle of the sample

5.1.2 Temperature difference along the sample

The difference along the sample evaluates the difference between the temperature in the middle of the sample, just above the initiator cell, and in one of the corners, the right corner bottom. This calculus is related to the thermal stress that the material can be under during the TR process. The difference in thermal expansion coefficients between the matrices and the fibers can induce internal stresses that can cause cracks in the material [46].

Equation 5.1 is employed to calculate the temperature difference between the two control points of the sample. The sample with the lowest temperature difference gets a score of 5; the rest of the sample's temperature differences are compared to it to get their scores.

$$\frac{\text{Sample middle temperature} - \text{Sample CRB temperature}}{\text{Sample middle temperature}} \cdot 100 \qquad (5.1)$$

At Table 5.4, each sample's temperature difference and their respective scores can be observed. When comparing the single-cell experiment, it can be observed that the best score is obtained by CF/PPS 1, followed by GF/PEEK 2 and CF/PEEK 2. The lowest scores are obtained by CF/PEEK 1 and CF/PPS 3. A clear correlation between the thermal conductivity of the fiber or resin material and the score obtained is not observed. CF/PC obtains the best score compared to the other single-cell tests.

For this parameter, a correlation between the difference in behavior of the same material under the two different tests that they were under is not observed; for example, CF/PEEK 4 obtained the same score as CF/PEEK 2, and CF/PPS 4 obtain a higher score than CF/PPS 2 but lower than CF/PPS1.

Sample	Sample middle max. temperature [ºC]	Sample CRB max. temperature [ºC]	Max. temperature difference [%]	Score
CF/PC	187	214.87	14.90	2.2
CF/PEEK 1	338.9	273.33	19.35	1.3
CF/PEEK 2	285	267.3	6.21	3.8
CF/PEEK 3	262.3	280.8	7.05	3.7
CF/PEEK 4	260	209.7	19.35	1.3
GF/PEEK 1	382.4	329	13.96	2.4
GF/PEEK 2	274.2	282.3	2.95	4.4
GF/PEEK 3	342.3	294.7	13.91	2.4
CF/PPS 1	285.5	285.5	0.00	5.0
CF/PPS 2	478.1	428.4	10.40	3.0
CF/PPS 3	278.9	205.4	26.35	0.0
CF/PPS 4	250.2	203.9	18.51	1.5
GF/PPS 1	272.9	248.6	8.90	3.3
GF/PPS 2	302.5	244.5	19.17	1.4
GF/PPS 3	277.7	240.7	13.32	2.5

Table 5.4   : Maximum sample temperature difference and screening scores

5.1.3 Mass loss

Mass loss is a quantitative way of reflecting the material degradation, structural integrity, and thermal resistance of the materials.

Table 5.5 shows each sample's mass loss in percentage after cleaning and their respective score. The sample with the lowest mass loss gets a score of 5, and the rest of the sample's mass loss is compared to it to get the score, except for CF/PPS 3, which had a fracture during TR and failed in structural integrity, this sample got a score of 0.

For the multi-cell experiment the samples with higher scores are CF/PPS 1 and CF/PPS 2, followed by the CF/PEEK samples. From this comparison, it is observed that fiber material is a crucial factor in the mass loss parameter; the best scores are obtained in materials with CF and the worst in materials with GF.

For the single-cell experiments, the three samples obtained excellent scores. CF/PEEK under the single-cell experiment obtain a higher score than the samples of the same material under the multi-cell test. The same happens to CF/PPS material. This behavior results from the explosions in the single-cell test being less intense and involving less fire than those in the multi-cell test; because of that, samples under single-cell TR presented lower material degradation and lower ML than the ones under multi-cell TR.

Sample	Mass loss [%]	Score
CF/PC	1.36	4.5
CF/PEEK 1	3.23	3.5
CF/PEEK 2	3.32	3.4
CF/PEEK 3	3.80	3.2
CF/PEEK 4	0.80	4.9
GF/PEEK 1	4.93	2.5
GF/PEEK 2	4.03	3.0
GF/PEEK 3	4.91	2.5
CF/PPS 1	0.69	4.9
CF/PPS 2	2.32	4.0
CF/PPS 3	4.70	0.0
CF/PPS 4	0.56	5.0
GF/PPS 1	4.89	2.5
GF/PPS 2	7.41	1.1
GF/PPS 3	8.77	0.3

Table 5.5 : Mass loss score

5.1.4 Final score

This section presents the final score of each sample and the average score for each composite material.

At Table 5.6, the scores of each parameter and the final score, the average score for each sample, are found. A separate analysis of the samples tested under single-cell TR and the ones tested under multi-cell TR is performed in the next section.

Sample	T ratio score	T difference along the sample score	ML score	Final score
CF/PC	2.0	2.2	4.5	3.6
CF/PEEK 1	3.3	1.3	3.5	3.0
CF/PEEK 2	5.0	3.8	3.4	3.8
CF/PEEK 3	3.7	3.7	3.2	3.4
CF/PEEK 4	3.0	1.3	4.9	3.8
GF/PEEK 1	2.1	2.4	2.5	2.4
GF/PEEK 2	2.7	4.4	3.0	3.2
GF/PEEK 3	1.4	2.4	2.5	2.3
CF/PPS 1	1.5	5.0	4.9	4.3
CF/PPS 2	1.7	3.0	4.0	3.3
CF/PPS 3	0.2	0.0	0.0	0.0
CF/PPS 4	2.5	1.5	5.0	3.8
GF/PPS 1	2.7	3.3	2.5	2.7
GF/PPS 2	3.6	1.4	1.1	1.6
GF/PPS 3	3.2	2.5	0.3	1.3

Table 5.6   : Final screening scores for each sample

5.2 Multi-cell test and single-cell test comparison

In this section, a comparison between the single-cell test and the multi-cell test results is found. As was stated previously in this chapter, the conditions from the 21700 and the 4695 experiments are theoretically really similar to each other. In reality, as seen in Table 5.1, it can be seen that some parameters differ from one type of experiment to the other such as the heating rate of the initiator cell is higher in the multi-cell tests than in the single-cell tests and the time to reach TR is higher when using the 4695 cell.

At Figure 5.1 and Figure 4.40, the differences at the maximum temperatures of the samples and the maximum differential pressure are presented visually. Except CF/PPS 2 the values of the maximum differential pressure are higher for the single cell test than for the multi-cell test. In terms of maximum temperature difference along the sample, the distribution differs between the two types of cells, and the values of maximum temperatures in the 4695 experiment are, in most cases, lower than in the 21700 experiments. From the pictures taken from the normal camera recording Figure 4.73, Figure 4.38, Figure 4.13, it can be seen that the level of sparks, smoke, and fire is higher in for the 21700 test than for the 4695 test. Moreover, when performing the experiments, it was noticed that the sound of the explosion for the 4695 tests was lower than for the explosion at the 21700 tests.
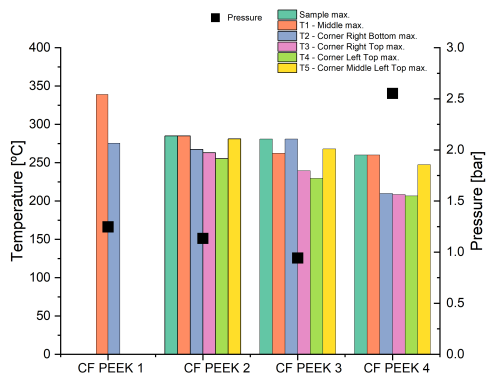
Figure 5.1 : CF/PEEK summary of behavior under TR
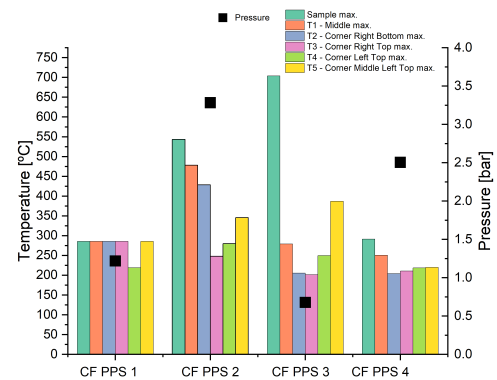
Figure 5.2 : CF/PPS summary of behavior under T

For all the reasons listed above, the comparison should be performed to determine the samples with best performance under the same type of tests.

5.2.1 21700 test parameters evaluation

At Table 5.7, it can be observed that the CF/PPS 1 has the highest final scores. However, as already commented, CF/PPS 3 suffered from rupture during TR and occupies the lowest position; further investigation on the behavior of this combination under these conditions is suggested for future experiments. All the CF/PEEK samples are found in the first six best scores. It is observed that except for CF/PPS 3, which has the lowest score, as a general rule, the materials with CF presented better behavior according to the parameter evaluation over the ones with GF. PEEK matrix with GF presents better behavior than use a PPS matrix with GF.

Sample	T ratio score	T difference along the sample score	ML score	Final score
CF/PEEK 1	3.3	1.3	3.5	3.0
CF/PEEK 2	5.0	3.8	3.4	3.8
CF/PEEK 3	3.7	3.7	3.2	3.4
GF/PEEK 1	2.1	2.4	2.5	2.4
GF/PEEK 2	2.7	4.4	3.0	3.2
GF/PEEK 3	1.4	2.4	2.5	2.3
CF/PPS 1	1.5	5.0	4.9	4.3
CF/PPS 2	1.7	3.0	4.0	3.3
CF/PPS 3	0.2	0.0	0.0	0.0
GF/PPS 1	2.7	3.3	2.5	2.7
GF/PPS 2	3.6	1.4	1.1	1.6
GF/PPS 3	3.2	2.5	0.3	1.3

Table 5.7   : 21700 test final screening scores for each sample

At Table 5.9, the average score for each material composite is presented. PEEK matrices obtain the best scores, with the CF/PEEK combination being the best. GF/PEEK presents the second higher score, and CF/PPS, with the third position, is just 0.1 points under GF/PEEK. However, if the CF/PEEK 3 sample that failed was not taken into consideration for the average calculation, the final score would be 3.8, 0.4 points over CF/PEEK composite.

Another key factor to analyse is the initial weight at Table 5.1 it can be observed that the CF/PEEK samples are lighter before TR than the GF/PEEK samples. The average weight of CF/PEEK samples is 63.42 g, while for GF/PEEK is 75.07g. This factor indicates that not only the score of CF/PEEK is the highest but also that the second best option is heavier than it; lightness is a key factor for material selection for aeronautics purposes. If CF/PPS 3 had not failed, CF/PPS would have presented better qualities for acting as the LIB enclosure material under the TR conditions studied.

Sample type	Final score
CF/PEEK	3.4
GF/PEEK	2.6
CF/PPS	2.5
GF/PPS	1.9

Table 5.8   : 21700 test final screening scores for each composite material

5.2.2 4695 test parameters evaluation

For the 4695 test, it is observed at Table 5.9 that when comparing the samples for this test, CF/PEEK and CF/PPS are tied in the first position. CF/PC has the lowest score, however, the score is only 0.2 under the CF/PEEK and CF/PPS scores. In terms of weight CF/PPS 4 (50.68 g) is lighter than CF/PC (51.60 g) and CF/PEEK (63.30 g), which is a reason to choose CF/PPS over CF/PEEK. A remark on this selection is that it only takes into account the 4695 test, as even though the material resisted the 4695 test, the material's structural integrity failed during one of the 21700 tests.

Sample	T ratio score	T difference along the sample score	ML score	Final score
CF/PC	2.0	2.2	4.5	3.6
CF/PEEK 4	3.0	1.3	4.9	3.8
CF/PPS 4	2.5	1.5	5.0	3.8

Table 5.9   : 21700 test final screening scores for each composite material

6 Summary and Outlook

This project aims to contribute to the transition to electrification in the aeronautical sector by testing different fiber-reinforced composite materials for the energy storage system of lithium-ion batteries under TR conditions. For this purpose, PMC thermoplastic matrices, PEEK, PC, and PPS, will be tested combined with GF for the PEEK, PPS matrices, and CF for all the matrices.

A literature review, consisting of four branches, is conducted. The first one is a revision of the working principle of LIBs as well as their types, properties, types of failure, and applications in the aerospace sector. A more exhaustive literature review of TR, one of the main types of failure, is performed, summarizing its cases and stages. Once the LIBs and the phenomenon to be studied, the TR, are analyzed, a literature review on composite materials regarding their definition, the types of matrices and reinforcements and their thermal and mechanical properties, their aerospace applications, and their fire resistance and fire reaction properties are carried out. To focus on the final purpose of the project, a literature review of the current standard test method and studies on the thermal performance of battery enclosure materials is completed.

Afterward, a series of tests are performed to screen the materials selected. The materials employed for the tests are listed, including the main technical characteristics of the cells and composite tested, the measurement equipment, and the support equipment to carry out the tests. The assembly of the materials, the codes developed to perform the test, and the workflow during the experimental campaign are also detailed. For carrying on the experiments, the calculations of the boundary conditions from previous experiments and preliminary tests of the code, thermocouples, heating foils, and thermal cameras were carried out.

For TR, two different cells are employed, the INR21700-50S and INR4695. 21700 cells were tested in groups of seven cells; the one in the middle, the initiator cell, was heated by two heating foils at an average heating rate of 31.93 ºC/min. For the multi-cell experiment, twelve experiments were performed; CF/PEEK, GF/PEEK, CF/PPS, and GF/PPS samples were tested; for each material, three samples were tested. For the 4695 cell tests, only one cell was placed on the battery enclosure; the cell was heated with three heating foils with an average heating rate of 11.11 ºC/min. A calibration test with a steel plate was performed, and CF/PC, CF/PEEK, and GF/PPS materials were tested once for the single-cell test.

After reviewing the experiment videos, the first conclusion obtained is that even though thermocouples can measure sample temperatures, it is better to use a thermal camera for more precise results, as thermocouples often become detached from the samples during

testing. Another recommendation is to use multiple thermocouples at each point of interest to reduce the risk of detachment. It is important to note that multiple thermocouples were used to measure the ambient temperature measurements of the battery enclosure, the surrounding cells, and the initiator to obtain data for all variables, even if one failed. This method worked in most cases since the thermocouples were tested before starting the test. However, there were also some tests in which data could not be collected for some variables. As a solution, it is suggested that future experiments should be more redundant, and if possible, more than two thermocouples should be used per variable. It is highly recommended to use thermal camera protection as samples can fracture, as in the case of the CF/PPS 3, and damage the camera. Also, when using the thermal camera, it is recommended to add painter's tape to the edges of the enclosure to avoid reflections on the sample.

In the visualization and discussion of the results, a similar behavior was observed in the temperature graphs of the thermocouples inside the enclosure concerning the shape, both for the 21700 cells and the 4695 cell experiments. It is suggested that the peaks presented in the recorded differential pressure of the multi-cell experiment that followed the initial peak represent the TR of the surrounding cells.

For the 21700 cells experiments, it was observed that, in general, the samples containing GF presented higher material damage and swelling after TR than CF samples, except for CF/PPS 3, which fractured during the TR process. Greater repeatability is observed in the results when using PEEK matrices than PPS. This is evident in both temperatures and mass loss, as PEEK matrices presented a lower standard deviation. Additionally, the use of CF decreases the mass loss after the TR.

For the case of the experiments with the 4695 battery, the calibration was carried out with a steel sample; however, most of the thermocouples failed, and their data could not be collected; it was observed that three heating foils had to be used to induce the TR of the cell. Regarding the results of the sample tests, similar maximum temperatures were observed for the three cases, and a lower mass loss was observed using the PPS matrix.

Finally, a parameter evaluation was carried out by assessing the temperature ratios, the temperature difference along the sample, and the percentage of mass loss. The percentage of mass loss was the parameter with the highest weight on the final score. When studying the temperature ratios between the maximum temperature of the battery enclosure and the maximum temperature of the sample, it was observed that not only the thermal conductivity of the material played an important role. As some of the materials showed a different behavior than expected due to their thermal conductivity and the current literature, it is suggested that some factors such as the environmental conditions, the TR conditions, and the difference in architecture of the fibers of the same type can influence the results. The manufacturer could have also used a different CF for the PEEK matrix than for the PPS matrix, and the same for GF composites. On the other hand, the

temperature difference along the sample did not present a clear correlation between the score obtained per each sample and its fiber and matrix materials. In the study of mass loss after TR, it was observed that the use of materials composed with CF implies lower ML than the use of the ones composed with GF.

Due to the difference in experimental conditions between the single-cell experiment and the multi-cell experiments, the materials are analyzed according to the type of experiment.

Regarding the evaluation of multi-cell experiments, the best combination was CF/PEEK followed by GF/PEEK. When evaluating the single-cell experiments, the best score was tied between the CF/PEEK and CF/PPS.

It is concluded from the material screening that the use of CF for composite materials under TR conditions presents better properties under the evaluated parameters than the use of GF. In the multi-cell experiment, PEEK matrices obtained higher scores than PPS matrices; however, in the single-cell experiment, CF/PPS material presented the same score as CF/PEEK material. This study highlights the need for further investigation into the behavior of the CF/PPS combination, as all the samples of this combination presented distinguished properties except for the CF/PPS 3, which did not present structural integrity as it ruptured during the TR test.

CF/PC presented a great score in the multi-cell parameters evaluation; however, its behavior under multi-cell TR was not tested. For future studies, it is suggested that the repeatability of the single-cell experiment for the three samples studied be checked, and the behavior of the CF/PC combination should be checked under the multi-cell test.

CF/PEEK obtains the highest score in the multi-cell test and in the single-cell test and the general analysis, it is a great candidate for coping with the conditions caused by the TR of the LIBs.

It would be beneficial to conduct additional research on screening the CF composite combinations materials, especially CF/PEEK studied with other FRCMs not studied in this project and in a controlled environment. Future lines of research are open to determine the most suitable composite material for the battery housing module under TR conditions.

Bibliography

[1] *ASTM Standard terminology of fire standards.*

[2] *Fire Properties of Polymer Composite Materials.*

[3] *PRODUCT SPECIFICATION Rechargeable Lithium-ion Cell Model: : INR4695-300A.*

[4] *TECATEC PEEK GF50 S296CP IP OS V01 natural DS 1.*

[5] *TECATEC PEEK MT CF50 S280 CP IP OS V01 natural DS 1.*

[6] *TECATEC PPS CF50 T200 CP IP OS V01 natural DS 1.*

[7] *TECATEC PPS GF50 P203 CP IP OS V01.*

[8] *UL 2596 Test Method for Thermal and Mechanical Performance of Battery Enclosure Materials.*

[9] *Thermal degradation and fire behaviour of unsaturated polyester with chain ends modified by dicyclopentadiene*, 1998.

[10] *Through-thickness thermal conduction in glass fiber polymer–matrix composites and its enhancement by composite modification.* Journal of Materials Science, 51:3463–3480, 4 2016.

[11] *Lithium-ion rechargeable cell for power tools Model name : INR21700-50S Energy Business Division*, 2020.

[12] *Fundamentals of composite materials - A100.* CKN, 2021.

[13] *Metal-Matrix Composites.* Machine Design, 2022.

[14] *Bench-scale fuel fire test for materials of rechargeable energy storage system housings.* Journal of Thermal Analysis and Calorimetry, 148:305–313, 1 2023.

[15] *Covalently modified graphene and 3D thermally conductive network for PEEK composites with electromagnetic shielding performance.* Composites Part A: Applied Science and Manufacturing, 173, 10 2023.

[16] *Description of Poly(aryl-ether-ketone) Materials (PAEKs), Polyetheretherketone (PEEK) and Polyetherketoneketone (PEKK) for Application as a Dental Material: A Materials Science Review*, 5 2023.

[17] *The influence of expandable graphite on the thermal, flame retardant and mechanical characteristics of short carbon fiber reinforced polyamide composites.* Journal

of Thermoplastic Composite Materials, 36:2777–2788, 7 2023.

[18] *Performance evaluation of various phosphorus compounds on the flammability properties of short carbon fiber-reinforced polyamide 6 composites.* Fire and Materials, 47:837–847, 10 2023.

[19] *Synthesis and Properties of Polystyrene Composite Material with Hazelnut Shells.* Polymers, 15, 8 2023.

[20] *Temperature and Thermal Aging Effects on the Mechanical Response of Polycarbonate Materials.* Volume 56, pages 71–77. Elsevier B.V., 2024.

[21] AIFANTIS, KATERINA E., R. VASANT KUMAR and PU HU: *Rechargeable Ion Batteries: Materials, Design, and Applications of Li-Ion Cells and Beyond.* Wiley, 1 2023.

[22] AL-HALLAJ, SAID and J R SELMAN: *Thermal modeling of secondary lithium batteries for electric vehicle/hybrid electric vehicle applications* .

[23] ALI, HAYDER, HECTOR BELTRAN, NANCY J. LINDSEY and MICHAEL PECHT: *Assessment of the calendar aging of lithium-ion batteries for a long-term—Space missions.* Frontiers in Energy Research, 11, 2 2023.

[24] AMIRABADI, SHAHAB, NICOLAS TANGUY, PETER SERLES, TOBIN FILLETER, MOHINI SAIN and CHUL B. PARK: *Heat and fire-resistant nanofiber networks: Towards tailoring the new generation of lightweight intermeshing polymer composite systems.* Chemical Engineering Journal, 467, 7 2023.

[25] AN, ZHOUJIAN, WENDA LI, XIAOZE DU, LI JIA, QINGLIANG LI and DONG ZHANG: *Experimental study on behaviors of lithium-ion cells experiencing internal short circuit and thermal runaway under nail penetration abuse condition.* Applied Thermal Engineering, 247, 6 2024.

[26] AUGEARD, AMAURY, TCHAPO SINGO, PHILIPPE DESPREZ and M'HAMMED ABBAOUI: *Contribution to the study of electric arcs in lithium-ion batteries.* IEEE Transactions on Components, Packaging and Manufacturing Technology, 6:1066–1076, 7 2016.

[27] AUGEARD, AMAURY, TCHAPO SINGO, PHILIPPE DESPREZ, FREDERIC PERISSE, SÉBASTIEN MENECIER and M ' HAMMED ABBAOUI: *Arc Analysis to the CID of Li-ion Battery Cells in High-Current Applications.*

[28] BAAZOUZI, SABRI, NIKLAS FEISTEL, JOHANNES WANNER, INGA LANDWEHR, ALEXANDER FILL and KAI PETER BIRKE: *Design, Properties, and Manufacturing of Cylindrical Li-Ion Battery Cells—A Generic Overview.* Batteries, 9, 6 2023.

[29] BAHRAMIAN, AHMAD REZA, MEHRDAD KOKABI, MOHAMMAD HOS-

SEIN NAVID FAMILI and MOHAMMAD HOSSEIN BEHESHTY: *Ablation and thermal degradation behaviour of a composite based on resol type phenolic resin: Process modeling and experimental*. Polymer, 47:3661–3673, 5 2006.

[30] BERESNEVICIUS, RYTIS: *Harbour Air says electric DHC-2 Beaver is delayed to at least mid-2025*. AEROTIME HUB, 4 2023.

[31] BOPPANA, SATISH BABU, C.G. RAMACHANDRA, PALANI K. KUMAR and S. RAMESH: *Structural Composite Materials*. Springer Nature Singapore, 2024.

[32] CAMPBELL, F.C.: *Structural Composite Materials*. 2010.

[33] CAMPO, E. ALFREDO: *1 - Polymeric Materials and Properties*. In CAMPO, E. ALFREDO (editor): *Selection of Polymeric Materials*, Plastics Design Library, pages 1–39. William Andrew Publishing, Norwich, NY, 2008.

[34] CARPIER, YANN, AURÉLIE BOURDET, NICOLAS DELPOUVE, ÉRIC DARGENT and BENOIT VIEILLE: *Thermal decomposition study of carbon fiber-reinforced polyphenylene sulfide at high heating rates met under fire exposure*. Journal of Thermal Analysis and Calorimetry, 149:6039–6050, 6 2024.

[35] CENTER, NASA JOHNSON SPACE, UNIVERSITY COLLEGE LONDON and OXFORD UNIVERSITY: *Transportation and Mobility Research Battery Failure Databank*, 2 2024.

[36] DAS, ABHIJIT and PRAKASH MAHANWAR: *A brief discussion on advances in polyurethane applications*, 7 2020.

[37] DOUGHTY, DAN and E. PETER ROTH: *A general discussion of Li Ion Battery Safety*. The Electrochemical Society Interface, 2012.

[38] FENG, XUNING, MOU FANG, XIANGMING HE, MINGGAO OUYANG, LANGUANG LU, HAO WANG and MINGXUAN ZHANG: *Thermal runaway features of large format prismatic lithium ion battery using extended volume accelerating rate calorimetry*. Journal of Power Sources, 255:294–301, 6 2014.

[39] FU, YANGYANG, SONG LU, KAIYUAN LI, CHANGCHEN LIU, XUDONG CHENG and HEPING ZHANG: *An experimental study on burning behaviors of 18650 lithium ion batteries using a cone calorimeter*. Journal of Power Sources, 273:216–222, 1 2015.

[40] GARCÍA, ANTONIO, JAVIER MONSALVE-SERRANO, RAFAEL LAGO SARI and SANTIAGO MARTINEZ-BOGGIO: *Influence of environmental conditions in the battery thermal runaway process of different chemistries: Thermodynamic and optical assessment*. International Journal of Heat and Mass Transfer, 184, 3 2022.

[41] GARCÍA, ANTONIO, JAVIER MONSALVE-SERRANO, FELIPE DE VARGAS LEWISKI and CARLOS GUARACO-FIGUEIRA: *Enhancing thermal runaway*

characterization in NMC811 lithium-ion batteries through laser-induced triggering. Journal of Power Sources, 610, 8 2024.

[42] GHOBADI, AMIN: *Common Type of Damages in Composites and Their Inspections*. World Journal of Mechanics, 07:24–33, 2017.

[43] GMBH, VAERIDION: *Vaeridion leading the green revolution in aviation*.

[44] GMBH, VOLOCOPTER: *Volocopter we pioneer sustainable urban air mobility*.

[45] GOLUBKOV, ANDREY W., DAVID FUCHS, JULIAN WAGNER, HELMAR WILTSCHE, CHRISTOPH STANGL, GISELA FAULER, GERNOT VOITIC, ALEXANDER THALER and VIKTOR HACKER: *Thermal-runaway experiments on consumer Li-ion batteries with metal-oxide and olivin-type cathodes*. RSC Advances, 4:3633–3642, 2014.

[46] GREISEL, M., J. JÄGER, J. MOOSBURGER-WILL, M. G.R. SAUSE, W. M. MUELLER and S. HORN: *Influence of residual thermal stress in carbon fiber-reinforced thermoplastic composites on interfacial fracture toughness evaluated by cyclic single-fiber push-out tests*. Composites Part A: Applied Science and Manufacturing, 66:117–127, 2014.

[47] HART, ROBERT, BENJAMIN DWYER, ANDREW SMAIL, AMMAR CHISHTI, DAVID ERB and ROBERTO LOPEZ-ANIDO: *LIGHTWEIGHT COMPOSITE CREW FLOOR FOR GROUND COMBAT VEHICLES*, 2021.

[48] HOFMANN, ANDREAS, NILS UHLMANN, CARLOS ZIEBERT, OLIVIA WIEGAND, ALEXANDER SCHMIDT and THOMAS HANEMANN: *Preventing Li-ion cell explosion during thermal runaway with reduced pressure*. Applied Thermal Engineering, 124:539–544, 2017.

[49] INC., POLLEN AM: *High performance materials for highly demanding applications*, 2024.

[50] INC., POLYMER COMPOSITES: *Carbon Fiber 3K 2×2 Twill Weave*.

[51] KANDOLA, B.K and E. KANDARE: *5.1 Introduction Composites having improved fire resistance*, 2008.

[52] KANGISHWAR, S., N. RADHIKA, ASAD AMAAN SHEIK, ABHINAV CHAVALI and S. HARIHARAN: *A comprehensive review on polymer matrix composites: material selection, fabrication, and application*, 1 2023.

[53] KARPENKO, MYKOLA, MICHAŁ STOSIAK, ADAM DEPTUŁA, KAMIL URBANOWICZ, JUSTAS NUGARAS, GRZEGORZ KRÓLCZYK and KRZYSZTOF ŻAK: *Performance evaluation of extruded polystyrene foam for aerospace engineering applications using frequency analyses*. International Journal of Advanced Manufacturing Technology, 126:5515–5526, 6 2023.

[54] KIM, MINSU and JOOHEON KIM: *Enhancement of the flame retardant properties of PPS-based composites via the addition of melamine-coated CaAl-LDH fire-retardant filler*. European Polymer Journal, 201, 12 2023.

[55] KOBAYASHI, YOSHINARI, KEISUKE MATSUMOTO, NAOKI MATSUKAWA and SHUHEI TAKAHASHI: *Opposed-flow flame spread over carbon fiber reinforced plastic with different carbon fiber orientations*. Proceedings of the Combustion Institute, 39:3899–3907, 1 2023.

[56] KURITA, AKIFUMI, YOHEI YOSHIMURA, MAKOTO SUZUKI, HIDETOSHI YOKOI and YUSUKE KAJIHARA: *Precise temperature calibration for visualized high-thermal-conductivity PPS in injection molding during filling process*. Precision Engineering, 82:91–105, 7 2023.

[57] LAMB, JOSHUA, CHRISTOPHER J. ORENDORFF, LEIGH ANNA M. STEELE and SCOTT W. SPANGLER: *Failure propagation in multi-cell lithium ion batteries*. Journal of Power Sources, 283:517–523, 6 2015.

[58] LI, GANG, FANG QU, ZHI WANG, XUHAI XIONG and YANYING XU: *Experimental Study of Thermal and Fire Reaction Properties of Glass Fiber/Bismaleimide Composites for Aeronautic Application*. Polymers, 15, 5 2023.

[59] LILIUM: *Why Lilium*.

[60] LIN, CHUNJING, HAORAN WEN, LEI LIU, SHIQIANG LIU, TIANYI MA, BIN FAN and FANG WANG: *Heat generation quantification of high-specific-energy 21700 battery cell using average and variable specific heat capacities*. Applied Thermal Engineering, 184, 2 2021.

[61] LIU, HUAQIANG, ZHONGBAO WEI, WEIDONG HE and JIYUN ZHAO: *Thermal issues about Li-ion batteries and recent progress in battery thermal management systems: A review*, 2017.

[62] LIU, YANHUI, LEI ZHANG, YIFEI DING, XIANJIA HUANG and XINYAN HUANG: *Effect of thermal impact on the onset and propagation of thermal runaway over cylindrical Li-ion batteries*. Renewable Energy, 222, 2 2024.

[63] LIU, ZHEN, XINRONG GUO, NA MENG, ZHANGLONG YU and HE YANG: *Study of thermal runaway and the combustion behavior of lithium-ion batteries overcharged with high current rates*. Thermochimica Acta, 715, 9 2022.

[64] MAHAMUD, RAJIB and CHANWOO PARK: *Theory and Practices of Li-Ion Battery Thermal Management for Electric and Hybrid Electric Vehicles*. Energies, 15, 6 2022.

[65] MAHMUD, MAYESHA BINTE, SAADMAN SAKIB RAHMAN, MARYAM FASHANDI, SHAHAB AMIRABADI, WENGE ZHENG and CHUL B. PARK: *Developing highly flame-retardant PA6-based composites via in-situ PPS nanofiber*

network. Polymer, 307, 7 2024.

[66] META, ENVALIOR: *Property Data (Provisional) 210fr-C200(x) 45*

[67] MOURITZ, A P*: Fire Safety of Advanced Composites for Aircraft, 2006.*

[68] NIEDUZAK, TYMON B., ELEONORA M. TRONCI, TIANYI ZHOU, LUKE B. DEMO *and* MARIA Q. FENG*: Heat transfer analysis through hybrid FRP composite for self-sensing lithium-ion battery enclosure. In* SHULL, PETER J., TZUYANG YU, ANDREW L. GYEKENYESI *and* H. FELIX WU *(editors):* Nondestructive Characterization and Monitoring of Advanced Materials, Aerospace, Civil Infrastructure, and Transportation XVIII, *page 39. SPIE, 5 2024.*

[69] NISHI, YOSHIO*: The development of lithium ion secondary batteries. Chemical Records, 1:406–413, 2001.*

[70] NUMMY, AMANDA*: Introduction of a battery enclosure thermal runaway material screening program for electric vehicles Background and Requirements.*

[71] NUMMY, AMANDA*: Material-Level Thermal Runaway Test Method for EV Battery Enclosure Design Introduction.*

[72] OGABI, RAPHAEL, BRADY MANESCAU, KHALED CHETEHOUNA *and* NICOLAS GASCOIN*: A study of thermal degradation and fire behaviour of polymer composites and their gaseous emission assessment, 11 2021.*

[73] OPTRIS*: PI 640i.*

[74] OPTRIS*: PI 640i CM.*

[75] PIPISTREL*: Pipistrel, 2024.*

[76] RAMGOBIN, ADITYA, GAËLLE FONTAINE *and* SERGE BOURBIGOT*: A case study of polyether ether ketone (I): Investigating the thermal and fire behavior of a high-performance material. Polymers, 12, 8 2020.*

[77] RANA, S. *and* R. FANGUEIRO*: Advanced composites in aerospace engineering, pages 1–15. Elsevier, 2016.*

[78] REMONDIS-GROUP, RETRON GMBH // A COMPANY OF THE*: Battery safety box RETRON 460, 2024.*

[79] REN, DONGSHENG, XUNING FENG, LANGUANG LU, XIANGMING HE *and* MINGGAO OUYANG*: Overcharge behaviors and failure mechanism of lithium-ion batteries under different test conditions. Applied Energy, 250:323–332, 9 2019.*

[80] SHAH, KRISHNA, DIVYA CHALISE *and* ANKUR JAIN*: Experimental and theoretical analysis of a method to predict thermal runaway in Li-ion cells. Journal of Power Sources, 330:167–174, 10 2016.*

[81] SHI, BOBO, WANGZHAONAN SHEN, BO YIN, ZHI WANG, HUI RUAN, ZHI-

HUA LI *and* DONG HUANG*:* Experimental study on suppressing thermal runaway propagation of lithium-ion battery modules by using liquid nitrogen: Influence of injection pipe diameter and position*. Thermal Science and Engineering Progress, 50, 5 2024.*

[82] SPOERK, MARTIN, CLEMENS HOLZER *and* JOAMIN GONZALEZ-GUTIERREZ*:* Material extrusion-based additive manufacturing of polypropylene: A review on how to improve dimensional inaccuracy and warpage*, 3 2020.*

[83] STERLING, J., L. TATTERSALL, N. BAMBER, F. DE COLA, A. MURPHY *and* S. L.J. MILLEN*:* Composite structure failure analysis post Lithium-Ion battery fire*. Engineering Failure Analysis, 160, 6 2024.*

[84] SUKUR, EMINE FEYZA*:* Thermally conditioned aerospace-grade carbon fiber reinforced polyether ketone ketone composites: Structure, impact response, and thermomechanical performance*. Polymer Composites, 44:2530–2544, 4 2023.*

[85] THERMTEST*:* Thermal Conductivity of Polycarbonate Materials*.*

[86] VIEILLE, BENOIT *and* ALEXIS COPPALLE*:* In situ compressive behavior of carbon fibers reinforced PolyEtherEther Ketone laminates exposed to one-sided heat flux*. Journal of Composite Materials, 58:1737–1750, 6 2024.*

[87] WALKER, W. Q.*:* Rechargeable lithium batteries for aerospace applications, *pages 369–383. Elsevier Inc., 4 2015.*

[88] WANG, QINGSONG, PING PING, XUEJUAN ZHAO, GUANQUAN CHU, JINHUA SUN *and* CHUNHUA CHEN*:* Thermal runaway caused fire and explosion of lithium ion battery*, 6 2012.*

[89] WILLSTRAND, OLA, MOHIT PUSHP, PETRA ANDERSSON *and* DANIEL BRANDELL*:* Impact of different Li-ion cell test conditions on thermal runaway characteristics and gas release measurements*. Journal of Energy Storage, 68, 9 2023.*

[90] YE, JIANA, HAODONG CHEN, QINGSONG WANG, PEIFENG HUANG, JINHUA SUN *and* SIUMING LO*:* Thermal behavior and failure mechanism of lithium ion cells during overcharge under adiabatic conditions*. Applied Energy, 182:464–474, 11 2016.*

[91] YU, YAN, GUOSHENG JIA, LIANG ZHAO, HENGXUE XIANG, ZEXU HU, GUIYIN XU *and* MEIFANG ZHU*:* Flexible and heat-resistant polyphenylene sulfide ultrafine fiber hybrid separators for high-safety lithium-ion batteries*. Chemical Engineering Journal, 452, 1 2023.*

[92] YUAN, QING FENG, FENGGANG ZHAO, WEIDONG WANG, YANMING ZHAO, ZHIYONG LIANG *and* DANLIN YAN*:* Overcharge failure investigation of lithium-ion batteries*. Electrochimica Acta, 178:682–688, 7 2015.*

[93] ZHANG, JINGFAN, YIFANG HUA, JIAN LIU, TAO ZHU, JUN SUN, XIAOYU GU, HONGFEI LI, JINGMAO ZHAO *and* SHENG ZHANG*:* Constructing flame retardant silica nanoparticles through styrene maleic anhydride copolymer grafting for PC/ABS composites. *Composites Part A: Applied Science and Manufacturing, 175, 12 2023.*

[94] ZHANG, LEEN, XIAOPING WANG, JINGYU PEI *and* YU ZHOU*:* Review of automated fibre placement and its prospects for advanced composites, *6 2020.*

[95] ZHANG, YUE, WENXIN MEI, PENG QIN, QIANGLING DUAN *and* QINGSONG WANG*:* Numerical modeling on thermal runaway triggered by local overheating for lithium iron phosphate battery. *Applied Thermal Engineering, 192, 6 2021. Nume.*

[96] ZHU, MINGHAO, SIYU ZHANG, YIN CHEN, LUYAO ZHAO *and* MINGYI CHEN*:* Experimental and analytical investigation on the thermal runaway propagation characteristics of lithium-ion battery module with NCM pouch cells under various state of charge and spacing. *Journal of Energy Storage, 72, 11 2023.*

[97] ZIMMERMANN, WOLFGANG*:* Degradation of Plastics by Fungi. *In* ZARAGOZA ÓSCAR *and* ARTURO CASADEVALL *(editors):* Encyclopedia of Mycology, *pages 650–661. Elsevier, Oxford, 2021.*

[98] ZONG, JIANAN, BINGJIE ZHU, ZHONGXI HOU, XIXIANG YANG *and* JIAQI ZHAI*:* Evaluation and comparison of hybrid wing vtol uav with four different electric propulsion systems. *Aerospace, 8, 9 2021.*

[99] ÖZSOY ÖZGE *and* ADVISOR MARGARITA ETCHEGARAY BELLO*:* Fiber-Reinforced Polymer Material Screening under Thermal Runaway Conditions for Li-ion Battery Enclosure in Garching near Munich, *2024.*

List of Figures

List of Tables

Appendix

A Offset graphs

Experiment	Thermal camera [s]	QUANTUM X T and p [s]
STEEL	-842.63747	-842.63747
CF/PC	-	-829.65971
CF/PEEK 1	-	-235.82591
CF/PEEK 2	-227.41211	-225.70392
CF/PEEK 3	-195.30098	-200.03690
CF/PEEK 4	-757.60870	-761.40452
GF/PEEK 1	-363.97122	-384.43810
GF/PEEK 2	-199.40683	-211.34074
GF/PEEK 3	-241.17282	-226.06657
CF/PPS 1	-269.75828	-282.58690
CF/PPS 2	-223.82910	-230.35455
CF/PPS 3	-233.67754	-228.09173
CF/PPS 4	-659.61957	-685.25659
GF/PPS 1	-236.86896	-216.28140
GF/PPS 2	-222.19203	-258.81346
GF/PPS 3	-220.73370	-218.51829

Table 6.1 : Offsets for the thermal camera graphs and Quantum X graphs (thermocouples temperature and pressure sensor graphs)

B Thermocouple and pressure sensor graphs

CF/PEEK 1 results
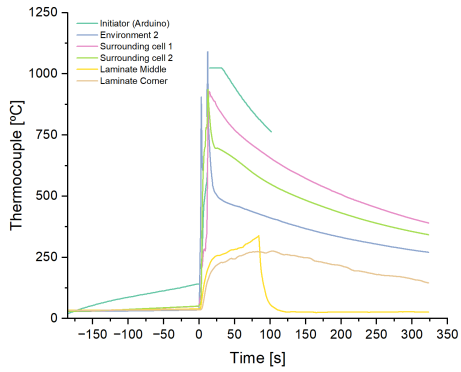
Figure 6.1 : CF/PEEK 1 thermocouple measurements during TR test
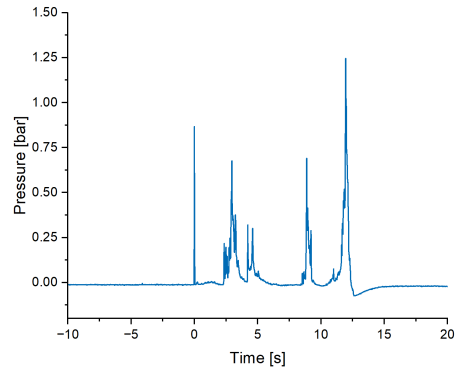
Figure 6.2 : CF/PEEK 1 pressure measurement during TR test

CF/PEEK 2 results
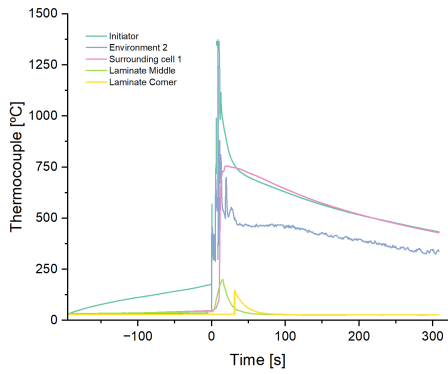
Figure 6.3 : CF/PEEK 2 thermocouple measurements during TR test
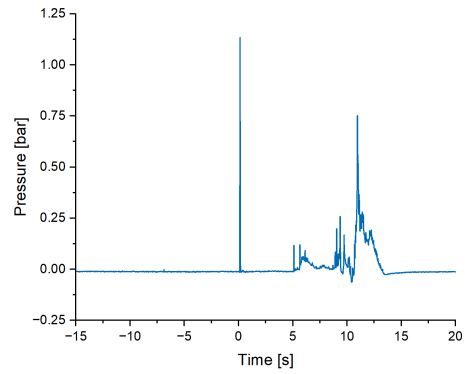
Figure 6.4 : CF/PEEK 2 pressure measurement during TR test

CF/PEEK 3 results
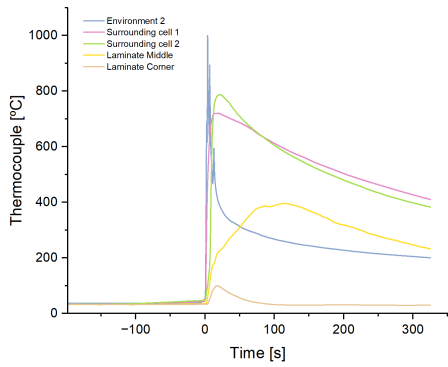
Figure 6.5 : CF/PEEK 3 thermocouple measurements during TR test
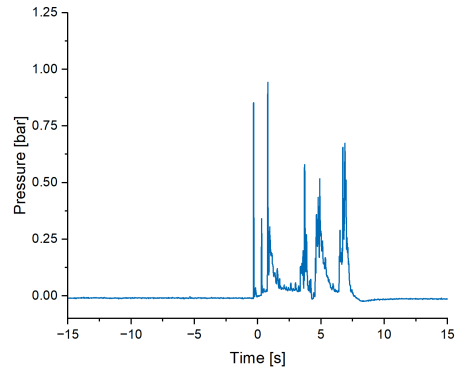
Figure 6.6 : CF/PEEK 3 pressure measurement during TR test
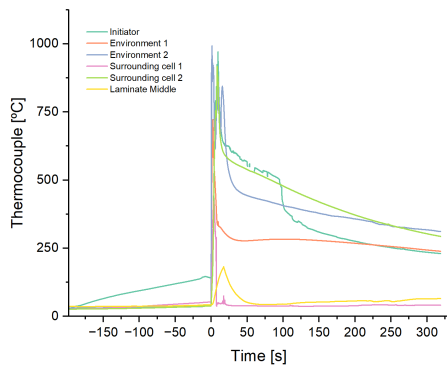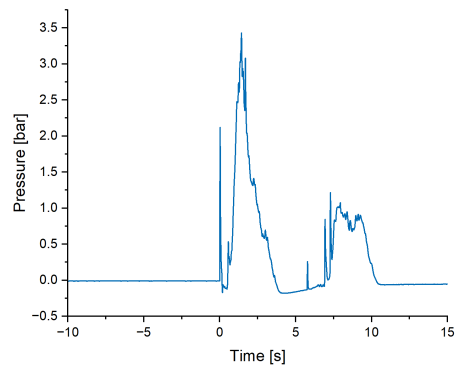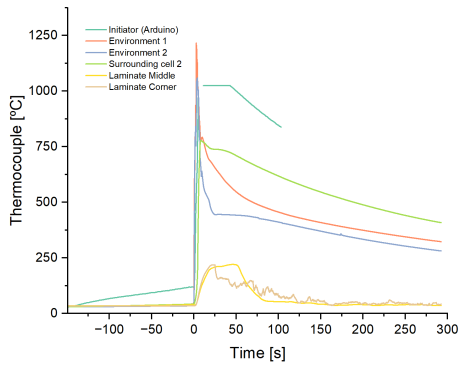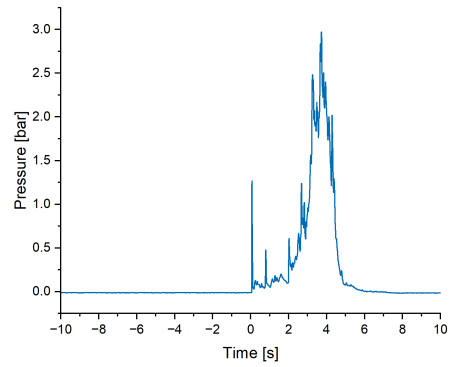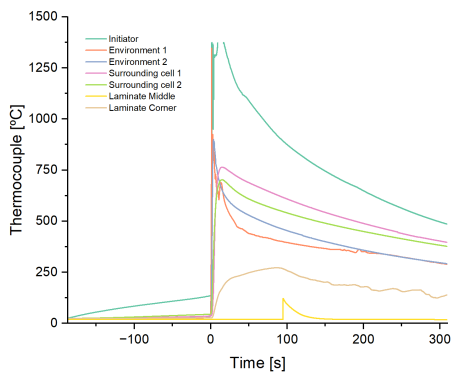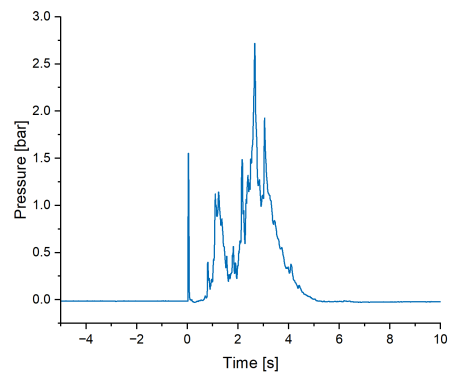
GF/PEEK 1 results
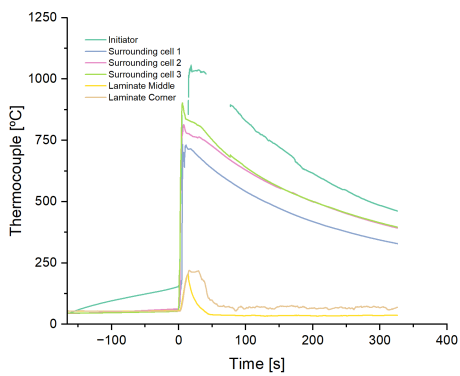
Figure 6.7 : GF/PEEK 1 thermocouple measurements during TR test
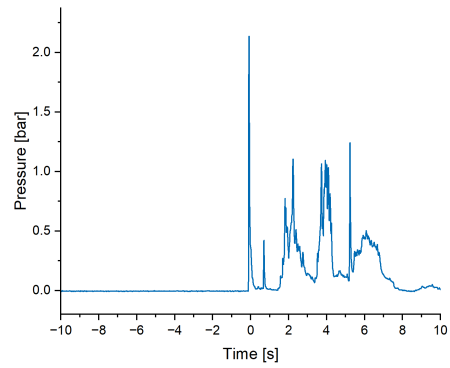
Figure 6.8 : GF/PEEK 1 pressure measurement during TR test

GF/PEEK 2 results
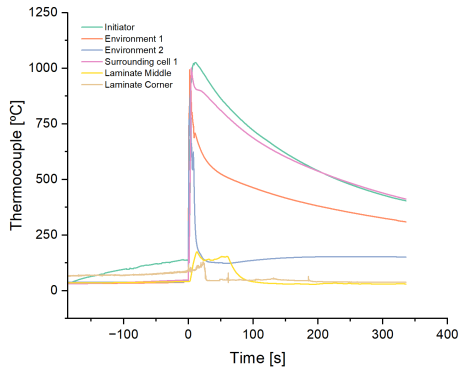
Figure 6.9 : GF/PEEK 2 thermocouple measurements during TR test
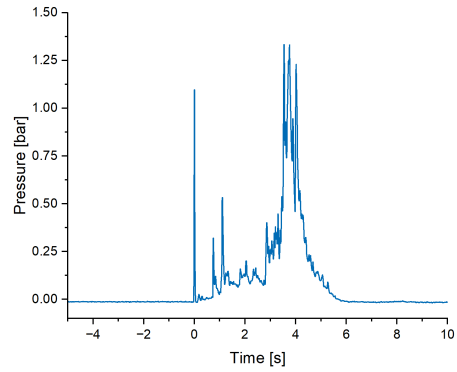
Figure 6.10 : GF/PEEK 2 pressure measurement during TR test

GF/PEEK 3 results
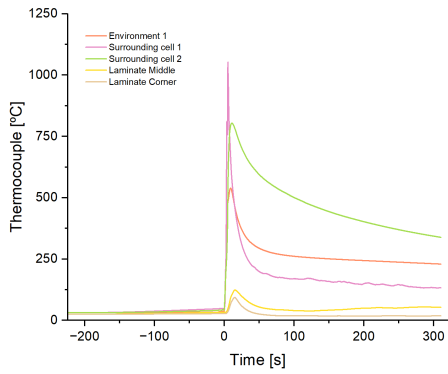
Figure 6.11 : GF/PEEK 3 thermocouple measurements during TR test
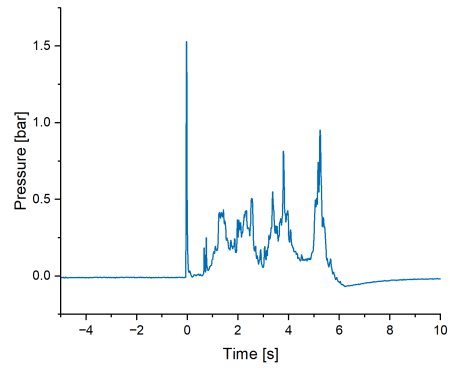
Figure 6.12 : GF/PEEK 3 pressure measurement during TR test

CF/PPS 1 results
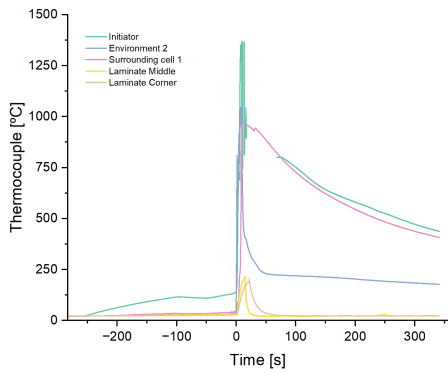
Figure 6.13 : CF/PPS 1 thermocouple measurements during TR test
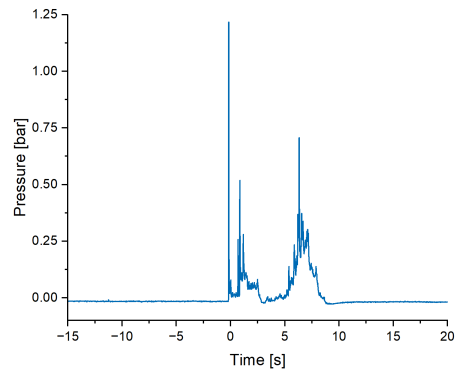
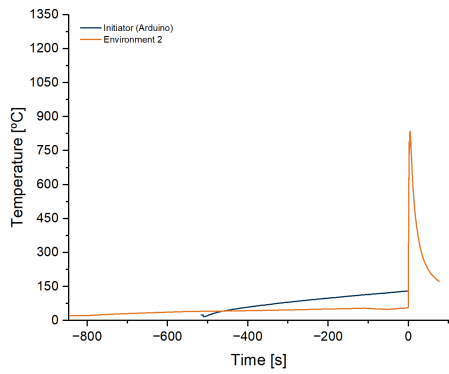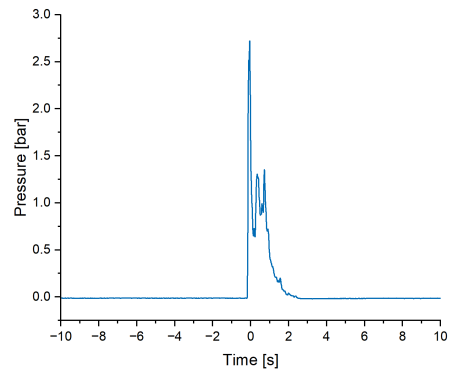Figure 6.14 : CF/PPS 1 pressure measurement during TR test

CF/PPS 2 results
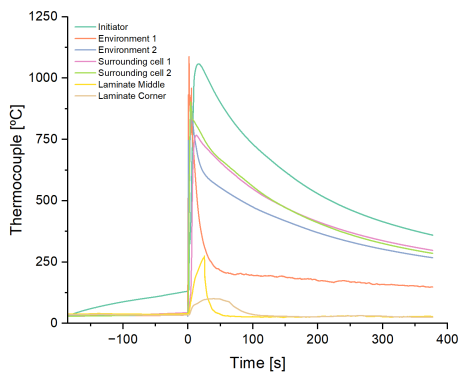
Figure 6.15 : CF/PPS 2 thermocouple measurements during TR test
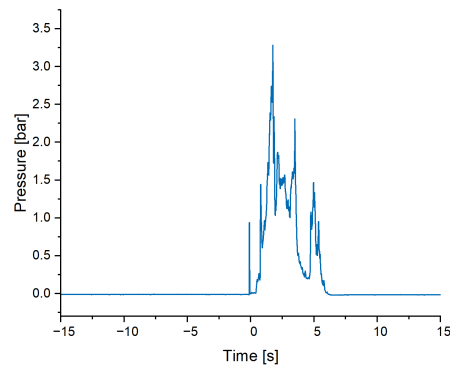
Figure 6.16 : CF/PPS 2 pressure measurement during TR test
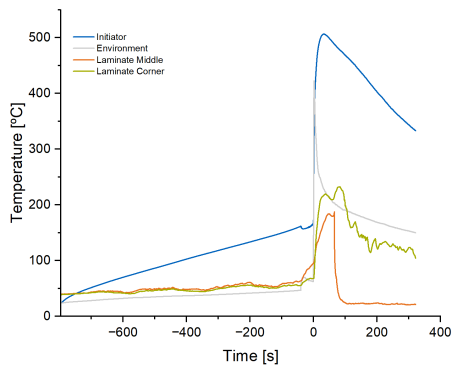
CF/PPS 3 results
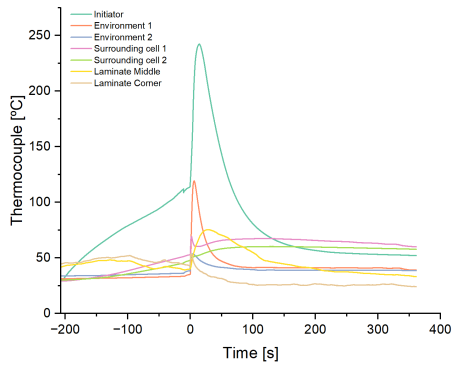
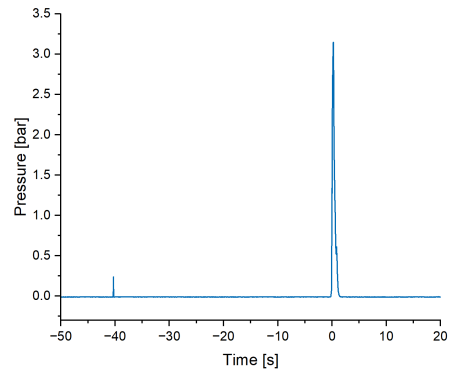Figure 6.17 : CF/PPS 3 thermocouple measurements during TR test
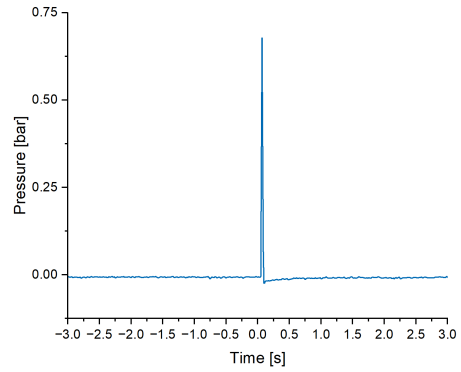
Figure 6.18 : CF/PPS 3 pressure measurement during TR test

GF/PPS 1 results

Figure 6.19 : GF/PPS 1 thermocouple measurements during TR test

Figure 6.20 : GF/PPS 1 pressure measurement during TR test

GF/PPS 2 results

Figure 6.21 : GF/PPS 2 thermocouple measurements during TR test

Figure 6.22 : GF/PPS 2 pressure measurement during TR test

GF/PPS 3 results

Figure 6.23 : GF/PPS 3 thermocouple measurements during TR test

Figure 6.24 : GF/PPS 3 pressure measurement during TR test

Steel plate

Figure 6.25 : STEEL thermocouple measurements during TR test

Figure 6.26 : STEEL pressure measurement during TR test

CF/PC results

Figure 6.27 : CF/PC thermocouple measurements during TR test

Figure 6.28 : CF/PC pressure measurement during TR test
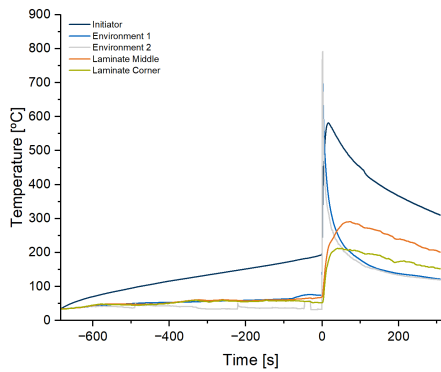
CF/PEEK 4 results

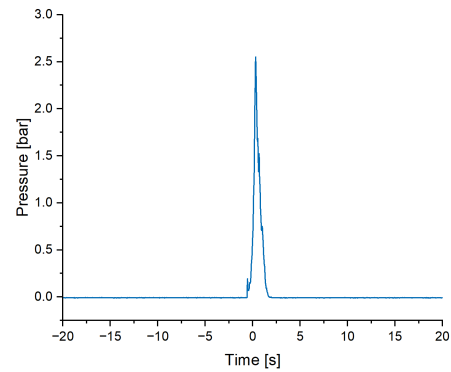Figure 6.29   : CF/PEEK 4 thermocouple measurements during TR test

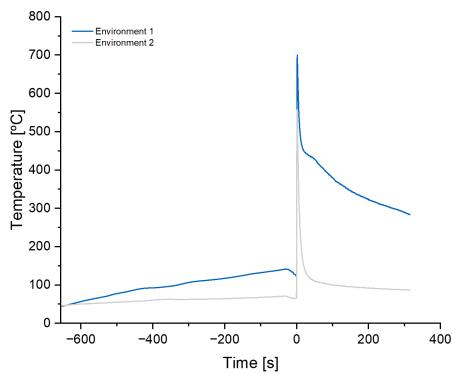Figure 6.30   : CF/PEEK 4 pressure measurement during TR test

CF/PPS 4 results

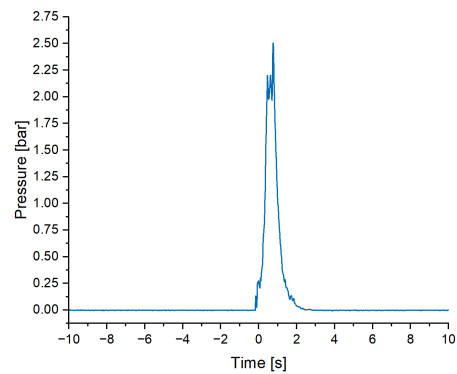Figure 6.31   : CF/PPS 4 thermocouple measurements during TR test

Figure 6.32   : CF/PPS 4 pressure measurement during TR test

C Folder

The folder: "TULR/lcc/Freigaben/Studentenprojekte/fernandez de_palencia_navarro_maria_(etchegaray_bello_mt_20241031)" contains the following data:

- Thesis in PDF and LaTeX format.

- Literature.

- Diagrams and figures.

- Design, preparation, execution and evaluation of the experiments.

- Code.